Light scattering in antiferromagnets with competing interactions - from spin chains to kagome lattices

Von der Fakultät für Elektrotechnik, Informationstechnik, Physik
der Technischen Universität Carolo-Wilhelmina
zu Braunschweig
zur Erlangung des Grades eines
Doktors der Naturwissenschaften
(Dr.rer.nat.)
genehmigte
D i s s e r t a t i o n

von: Dietrich Wulferding

aus (Geburtsort): Bassum

1. Referent: Prof. Dr. Peter Lemmens

2. Referent: Prof. Dr. Bernd Güttler

3. Referent: Prof. Dr. Meinhard Schilling

eingereicht am: 27. März 2013

mündliche Prüfung (Disputation) am: 05. Juli 2013

Druckjahr: 2013

Vorveröffentlichungen der Dissertation
Teilergebnisse aus dieser Arbeit wurden mit Genehmigung der Fakultät für Elektrotechnik, Informationstechnik, Physik, vertreten durch den Betreuer der Arbeit, in folgenden Beiträgen vorab veröffentlicht:

- **D. Wulferding**, P. Lemmens, P. Scheib, J. Röder, Ph. Mendels, S. Chu, T. Han, and Y. S. Lee, *Interplay of thermal and quantum spin fluctuations in the kagome lattice compound herbertsmithite*, Phys. Rev. B **82**, 144412 (2010).

- **D. Wulferding**, P. Lemmens, K.-Y. Choi, V. Gnezdilov, Yu. G. Pashkevich, J. Deisenhofer, D. Quintero-Castro, A. T. M. N. Islam, and B. Lake, *Coupled spin-lattice fluctuations in a compound with orbital degrees of freedom: The Cr-based dimer system* $Sr_3Cr_2O_8$, Phys. Rev. B **84**, 064419 (2011).

- M. A. de Vries, **D. Wulferding**, P. Lemmens, J. S. Lord, A. Harrison, P. Bonville, F. Bert, and P. Mendels, *Extension of the zinc paratacamite phase diagram: Probing the effect of spin vacancies in an* $S = 1/2$ *kagome antiferromagnet*, Phys. Rev. B **85**, 014422 (2012).

- **D. Wulferding**, P. Lemmens, H. Yoshida, Y. Okamoto, and Z. Hiroi, *The spin dynamics in distorted kagome lattices: a comparative Raman study*, J. Phys.: Condens. Matter **24**, 185602 (2012).

- **D. Wulferding**, K.-Y. Choi, P. Lemmens, A. N. Ponomaryov, J. van Tol, A. T. M. N. Islam, S. Toth, and B. Lake, *Softened magnetic excitations in the* $s = 3/2$ *distorted triangular antiferromagnet* α-$CaCr_2O_4$, J. Phys.: Condens. Matter **24**, 435604 (2012).

- **D. Wulferding**, P. Lemmens, K.-Y. Choi, Yu. G. Pashkevich, R. Yu. Babkin, K. V. Lamonova, A. Möller, J. M. Law, R. K. Kremer, and R. Glaum, *Phonon and orbital anomalies during the dimerization process in* $TiPO_4$, arXiv:cond-mat (2013).

Contents

List of Figures

List of Tables

Abstract

Within this thesis we discuss excitations in spin systems with competing interactions and orbital degrees of freedom. In particular, materials with frustration effects are investigated where interactions of similar strength compete. This can lead to a macroscopic degeneracy of ground states as well as strongly enhance quantum fluctuations. Promising candidates for a high degree of spin frustration are transition metal oxides with low dimensionality, a low spin quantum number and a low coordination number. Restricting the spin degrees of freedom geometrically can lead to an intricate interplay between spin, lattice and electronic degrees of freedom as well as a suppression of magnetic order due to strong quantum fluctuations down to lowest temperatures.

The kagome lattice, with a triangular motif, is of particular importance as it combines geometric frustration with a coordination number lower than in conventional triangular lattices. It may thus allow for spin liquid ground states with a vast ground state degeneracy. These states host exotic, fractional spinon excitations that can directly be probed using inelastic light scattering. On the other hand, one dimensional Heisenberg chains can display a rich number of phases, depending on details such as interchain interactions, orbital degeneracies, spin-Peierls instabilities, which drive the system from a 1D to a higher dimensional state and thereby modify the excitation spectrum. This can often be tuned by changing the temperature.

The first discussed compound is the quasi-1D isotropic $s = 1/2$ chain $TiPO_4$, which shows a spin-Peierls instability around $T_{SP} = 74$ K with the formation of a spin excitation gap. This is preceded by strong lattice dynamics in the temperature regime 111 K – 74 K. A high energy mode of mixed crystal field- and magnetic excitation is discovered for the first time using Raman spectroscopy. Additionally, the magnetic excitation spectrum allows to determine the energy of the spin-Peierls gap and the exchange interaction.

The frustrated spin dimer compound $Sr_3Cr_2O_8$ has a Jahn-Teller distortion around room temperature and shows a strong interplay of lattice and orbital degrees of freedom over a huge temperature range down to $T^* = 150$ K. In this temperature range an enhanced quasi-elastic scattering ($E \approx 0$) is observed, owing to orbital fluctuations. The temperature behaviour can be directly mapped onto measurements of the heat capacity. At lower temperatures, orbital ordering lifts the frustration, leading to a dimerized ground state. Two- and three magnon

scattering contributions observed in the Raman spectra at low temperatures allow the determination of the spin gap.

Temperature dependent Raman spectra of the three kagome lattice systems herbertsmithite, vesignieite and volborthite are investigated. In the perfect (i.e. undistorted) kagome lattice compound herbertsmithite we find a continuum of gapless spinon excitations at low temperatures. On the other hand, vesignieite, with a minute lattice distortion and Dzyaloshinsky-Moriya anisotropy, shows a clear onset of short-range magnetic ordering at temperatures below $T_{SRO} = 22$ K. Volborthite has a sizable distortion of the kagome lattice which increases at low temperatures and thus reduces the degree of magnetic frustration. Additionally, the excitation spectrum of the slightly distorted $s = 3/2$ triangular lattice compound α-$CaCr_2O_4$ is investigated. Despite its seemingly robust 120° ground state the excitation spectrum shows a structured, strongly renormalized structure, due to the system's proximity to a new magnetic phase.

Überblick

Der Schwerpunkt dieser Arbeit befasst sich mit Anregungen frustrierter Spinsysteme. Typischerweise wird Frustration durch konkurrierende Wechselwirkungen vergleichbarer Stärke ausgelöst. Dies führt zu einer hohen Entartung des Grundzustandes sowie zu starken Fluktuationen. Ein hoher Grad an Spinfrustration kann in Übergangsmetalloxiden mit niedriger Dimensionalität, niedriger Spinquantenzahl und niedriger Koordinationszahl erreicht werden. Die geometrische Einschränkung der Spinfreiheitsgrade führt oftmals zu einem komplexen Wechselspiel zwischen Spin-, Gitter- und elektronischen Freiheitsgraden, sowie zu einer völligen Unterdrückung der magnetischen Ordnung durch starke Quantenfluktuationen bis hin zu niedrigsten Temperaturen.

Das Kagome Gitter mit seiner Dreieckstruktur ist von besonderer Bedeutung, da es einen hohen Grad an geometrischer Frustration mit einer Koordinationszahl verbindet, die niedriger ist als in herkömmlichen Dreieckgittern. Somit ist es ein guter Kandidat für Spinflüssigkeitsgrundzustände. Diese Zustände zeichnen sich durch exotische, fraktionelle Spinon Anregungen aus. Andererseits erlaubt die eindimensionale Heisenbergkette das Studium zahlreicher Phasen, welche von scheinbar geringfügigen Unterschieden abhängen, wie schwache magnetische Zwischenkettenkopplung, orbitale Entartungen oder Spin-Peierls-Instabilitäten. Der Einfluss dieser Größen lässt sich oftmals einfach über die Temperatur regeln, und somit ist es möglich, die Physik des Systems von einer Dimension zu höheren Dimensionen zu überführen. Dies hat wiederum einen fundamentalen Einfluss auf das Anregungsspektrum.

Bei der ersten diskutierten Verbindung handelt es sich um die quasi isotrope, 1D $s = 1/2$ Kette $TiPO_4$, die sich durch eine Spin-Peierls-Instabilität bei $T_{SP} = 74$ K auszeichnet. Darüber hinaus existiert im Temperaturbereich von 111 K bis 74 K eine starke Gitterdynamik, in der eine inkommensurable Phase den Übergang von isotroper zu dimerisierter Struktur markiert. Weiterhin existiert eine temperaturabhängige Anregung im Bereich hoher Energien, basierend auf einer Kombination von Kristallfeld- und magnetischer Anregung. Eine solche Anregung wurde hier zum ersten Mal beobachtet. Zusätzlich ermöglicht das Spektrum magnetischer Anregungen die Größe der Spin-Peierls Lücke und der Austauschkonstante zu bestimmen.

Die frustrierte Spin-Dimer-Verbindung $Sr_3Cr_2O_8$ zeigt eine Jahn-Teller-Verzerrung unterhalb Raumtemperatur zusammen mit einer starken Wechsel-

wirkung von Gitter- und orbitalen Freiheitsgraden über einen ungewöhnlich großen Temperaturbereich von 275 K bis $T^* = 150$ K. In diesem Temperaturbereich ist eine starke quasielastische Streuung ($E \approx 0$) aufgrund orbitaler Fluktuationen zu beobachten. Das Temperaturverhalten dieser Streuung zeigt einen direkten Zusammenhang mit der spezifischen Wärmekapazität. Bei niedrigeren Temperaturen setzt eine orbitale Ordnung ein, was zur Aufhebung der Frustration führt. Gleichzeitig geht das System in einen dimerisierten Grundzustand über. Zwei-und drei-Magnon-Streubeiträge treten bei tiefen Temperaturen auf und erlauben die Bestimmung der Spin-Anregungs-Lücke.

Weiterhin wurden im Rahmen dieser Arbeit temperaturabhängige Ramanspektren der drei Kagome-Gittersysteme Herbertsmithite, Vesignieite und Volborthite untersucht. In dem strukturell perfekten Kagome-Gittersystem Herbertsmithite tritt ein Kontinuum von Spinon Anregungen ohne Spin-Lücke bei niedrigen Temperaturen auf. Andererseits zeigt Vesignieite, mit einer geringen Gitterverzerrung und Dzyaloshinsky-Moriya Anisotropie klare Anzeichen für kurzreichweitige magnetische Ordnung bei Temperaturen unterhalb $T_{SRO} = 22$ K. Volborthite hat eine beträchtliche Verzerrung des Kagome Gitters, welche bei niedrigen Temperaturen weiterhin zunimmt, und damit den Grad der Frustration verringert.

Schließlich wurde das Anregungsspektrum des leicht verzerrten $s = 3/2$ Dreieckgitters α-$CaCr_2O_4$ untersucht. Trotz seines scheinbar robusten 120° Spin-Grundzustands ist das magnetische Anregungsspektrum unerwartet stark energetisch abgesenkt und zudem strukturiert, was darauf schließen lässt, dass sich das System in der Nähe zu einem magnetischen Phasenübergang befindet.

Chapter 1

Introduction

Our present understanding of the solid state is based mainly on two paradigms that are used to categorize, connect and relate its fascinating and technologically important properties. These are given by the observation that, first, interaction effects within the solid state lead to ordering phenomena and, second, these ordering phenomena lead to a well-defined hierarchy of energy scales. This hierarchy is the basis for many useful approximations and allows using symmetry aspects of the given problems more efficiently.

A prominent example is the Born-Oppenheimer or adiabatic approximation, which allows us to separate the wave function of the electrons with small mass from the wave function of the lattice degrees of freedom with heavier mass. There are, however, interesting electron-lattice problems with intermixed electronic and lattice modes that do not allow such an approximation. Such effects usually happen for so-called Jahn-Teller ions in which lattice distortions lift the energetic degeneracy of 3d electron states within crystalline electric fields of high symmetry.

This thesis explores special cases of solids in which strong electronic correlations and magnetic exchange interactions exist. However, they may not lead to a ground state with broken symmetry and magnetic order. This concept of a *resonating valence bond* state (RVB) was first discussed in 1973 by Nobel laureate P. W. Anderson. It is based upon Pauling's famous valence bond theory that has been established to describe the delocalized electronic state of benzene by a wave function that connects 6 carbon atoms. In 1987, just after the discovery of high temperature superconductivity in layered Cu oxides, the RVB was a promising contender to describe the dynamics of charge carriers on the background of antiferromagnetic spin fluctuations. Although the applicability of the RVB model is strongly disputed for the latter compounds it has been highlighted as a theoretical concept to describe the magnetic correlations of spin frustrated, low dimensional compounds. The unusual physics of these low dimensional systems is governed by an incompatibility of magnetism and structure, and – as a consequence – the suppression of magnetic order. Oftentimes, the spin frustration is lifted at low temperatures via instabilities, such as a spin-Peierls transition in one dimensional

spin chains. Therefore, lattices with triangular motifs and hence, a large degree of frustration, were strongly considered for a RVB ground state. In particular, the kagome structure was recognized as a candidate for a new state of matter – the so-called spin liquid. The recent discovery of herbertsmithite as a perfect $s = 1/2$ kagome lattice has led to an avid interest of experimentalists in this compound. Within this thesis, Raman scattering experiments on herbertsmithite were carried out and allowed the observation of fractional spinon excitations. The subsequent classification of herbertsmithite as a gapless algebraic spin liquid is one cornerstone of this thesis. Further examples of strongly correlated electron systems with competing interactions discussed within this thesis include the spin chain $TiPO_4$, the dimer compound $Sr_3Cr_2O_8$ and the distorted triangular lattice α-$CaCr_2O_4$. All of these systems exhibit unusual hierarchies of energy scales that lead to exotic behaviour. The use of Raman scattering within this thesis allows not only observing and studying lattice, magnetic, and electronic excitations, but it additionally yields valuable information about their symmetry properties.

Further presently discussed challenges in strongly correlated electron systems are related to the question of topology of a quantum system: (i) in the small gap semiconductor Bi_2Se_3 topologically protected surface states exist that show unusual properties; (ii) in applying magnetic fields some compounds form topological defects of the spin polarization – so-called skyrmions – which could pave the way for novel magnetic data storage devices; (iii) the combination of magnetic anisotropy and atomic coordination leads to magnetic monopoles as quasiparticles in the so-called spin ice compounds $Dy_2Ti_2O_7$ and $Ho_2Ti_2O_7$. Raman light scattering can be and has been used in these and related topics to enhance our knowledge of, e.g., the energy scale and the interplay of the related excitations. As some of these questions are of fundamental as well as of applied relevance, this experimental technique is of essential importance.

Chapter 2

Basics of Raman scattering

Inelastic light scattering, or Raman scattering, is a well-established method to probe excited states in molecules, gases, liquids, as well as solids. The scattering process was first predicted by Smekal in 1923 [1] and subsequently observed in 1928 by the indian scientist Chandrasekhara Venkata Raman [2], who was awarded the Nobel prize in 1930 (it was independently also observed by Landsberg and Mandelstam around the same time). Since the advent of the laser in the 1960s, Raman scattering has become a prominent tool in chemistry and pharmacy, as it allows to easily analyze substances in a non-destructive and non-invasive way, and to determine their composition. On the other hand, the solid state physics community has benefitted from Raman scattering, e.g., to investigate semiconductors for defects, mechanical stress, or to conduct spatially resolved studies on microstructures. Another well-established application is magnetic Raman scattering, which allows to directly probe the magnetic exchange interaction (as well as the exchange geometry), e.g., in high temperature superconductors [3]. In this thesis more exotic materials are investigated, in which magnetic Raman scattering is not yet established. These are quantum critical or magnetically frustrated materials that may realize novel ground states such as spin liquids with unusual excitations. The great strength of Raman scattering is that it allows the direct observation of lattice, magnetic, and electronic excitations, and thereby the interplay of these quantities in strongly correlated electron systems can easily be studied.

2.1 Theory of Raman scattering

Thorough reviews on the theory of Raman scattering, upon which this brief outline is based, can be found, e.g. in [3], [4], and [5].

In a Raman scattering process incoming photons with a well-defined frequency ω_I and momentum $\vec{k}_I$ interact with a scattering medium, see Fig. 2.1. This leads to scattered photons with ω_S and $\vec{k}_S$, while the scattering medium progresses from an initial state $|i\rangle$ to a final state $|f\rangle$.

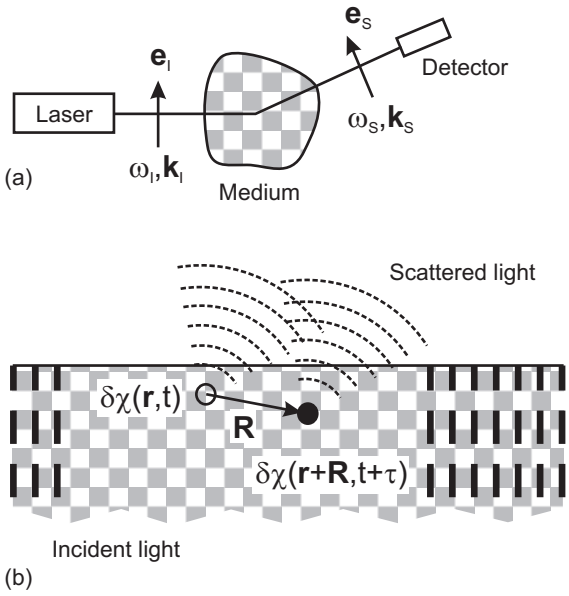

Figure 2.1: a) Basic sketch of the light scattering process, b) light scatters on spatial and temporal modulations of $\chi(\omega|\vec{r},t)$, [4].

Let's consider the propagation of a light beam with the electric field $\vec{E}$ in a medium, which leads to the polarization

$$\vec{P}_\omega = \epsilon_0 \chi(\omega)\vec{E} \tag{2.1}$$

Here, $\chi(\omega)$ denotes the polarizability. For a polarizability static in both space and time light will not be scattered. However, a modulation of $\chi(\omega|\vec{r},t)$ in space and time by quantum and/or thermal fluctuations allows the incoming light to scatter on these modulations. This yields a spectral density of final states

$$\rho(\vec{k},\Omega) \sim \int \langle \delta\chi^*(\vec{k},t)\delta\chi(\vec{k},0)\rangle e^{i\Omega t}\mathrm{d}t \tag{2.2}$$

with $\chi(\vec{r},t)$ transformed to momentum space and $\Omega = \omega_I - \omega_S$.

Considering a harmonic perturbation that acts upon the scattering medium and using first order perturbation theory one can write the polarizability as

$$\chi_{\alpha\beta}(\omega) = \frac{2}{\hbar}\sum_{i,f}\int \langle i\vec{k}|\hat{M}_\alpha|f\vec{k}\rangle\langle f\vec{k}|\hat{M}_\beta|i\vec{k}\rangle \times \left(\frac{1}{\Omega(\vec{k})-\omega}+\frac{1}{\Omega(\vec{k})+\omega}\right)\frac{\mathrm{d}^3k}{(2\pi)^3} \tag{2.3}$$

with the dipole matrix element $\langle f\vec{k}|\hat{M}_\beta|i\vec{k}\rangle$ between initial state $|i\rangle$ and final state $|f\rangle$. Here, α and β denote cartesian coordinates. Thus, the scattering probability depends on the polarization of the incident light. So far, the considered excitations that couple to $\chi(\vec{q},t)$ are very general. Possible sources for the modulation are phonons, magnetic excitations or energy fluctuations.

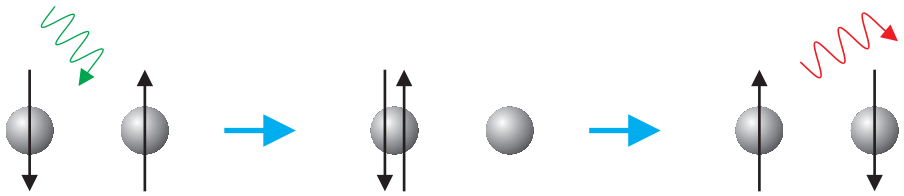

Figure 2.2: Mechanism of a 2-magnon scattering process.

To account for phonon excitations, let's consider a unit cell with N atoms. In the presence of an ionic displacement Q_ν the polarizability $\chi(\omega)$ will be changed accordingly:

$$\delta\chi^{\nu}_{\alpha\beta}(\omega) = \sum_{a=1}^{N} Q_{a,\nu} \frac{\partial \chi_{\alpha\beta}(\omega)}{\partial Q_a} \tag{2.4}$$

which yields a lorentzian spectral distribution with a maximum at the phonon frequency Ω_ν, an integrated intensity I and a linewidth related to the phonon damping γ_ν:

$$\rho(\Omega) = \frac{1}{\pi} I \frac{\gamma_\nu}{(\Omega - \Omega_\nu)^2 + \gamma_\nu^2} \tag{2.5}$$

A second mechanism, magnetic Raman scattering, arises through light scattering on modulations of $\chi(\omega)$ brought on by magnetic excitations (magnons) in the scattering medium. Using Taylor series expansion, the polarizability can be written as

$$\begin{aligned} \chi_{\alpha\beta}(r) \quad = \quad & \chi^{(0)}_{\alpha\beta}(r) + \\ & \underbrace{\sum_{\mu} K_{\mu,\alpha\beta}(r) S_{\mu,r} + \sum_{\mu,\nu} G_{\mu\nu,\alpha\beta}(r) S_{\mu,r} S_{\nu,r} +}_{1-magnon-scattering} \\ & \underbrace{\sum_{\delta} \sum_{\mu,\nu} H_{\mu\nu,\alpha\beta}(r,\delta) S_{\mu,r} S_{\nu,r+\delta} + \ldots}_{2-magnon-scattering} \end{aligned} \tag{2.6}$$

K, G and H are coupling constants between photons and spins. The two relevant terms are 1-magnon scattering and 2-magnon scattering. The former corresponds to a transition from a lower (e.g. ground) state to an excited state via coupling to spin orbit interaction. The latter term is ascribed to the simultaneous flip of two neighboring spins. Even though this is a higher order scattering term, no spin orbit coupling is needed. Therefore, 2-magnon scattering in general leads to a larger spectral weight. It is noteworthy that for one dimensional systems the 2-magnon term is identical with the Heisenberg Hamiltonian (see chapter 3). In fact, the two expressions commute. Therefore, 2-magnon scattering can only be observed in the presence of further interactions, such as next-nearest-neighbor correlations.

In addition, the polarization of the probing light must have a component in the direction of the exchange interaction to yield a finite 2-magnon intensity.

A third prominent contribution to a Raman spectrum is quasi-elastic scattering (QES). It is characterized by a broad mode centered at 0 cm^{-1} with a lorentzian line shape (when induced by energy density fluctuations) [6] or a gaussian line shape (when induced by spin diffusion) [7]. In magnetic systems it can be observed above the ordering temperature, when the light is polarized along the magnetic exchange paths. Its integrated intensity is directly related to the magnetic part of the specific heat, C_m, via

$$I(\omega) \sim C_m T^2 \frac{D_T k^2}{\omega^2 + (D_T q^2)^2} \tag{2.7}$$

with D_T being the thermal diffusion constant.

For systems with a structural transition at T_S, quasi-elastic scattering can be observed at temperatures slightly above T_S. Here a so called central mode appears due to phonon density fluctuations, which below T_S form new (soft) phonons.

2.2 Experimental

A Raman scattering experiment consists of a laser as a monochromatic light source, optical elements, a sample and a high resolution spectrometer with single photon sensitivity. The setup used in the following experiments is optimized with respect to stray light rejection. Therefore, we can access the spectral range down to $\sim 10\ \mathrm{cm}^{-1}$.

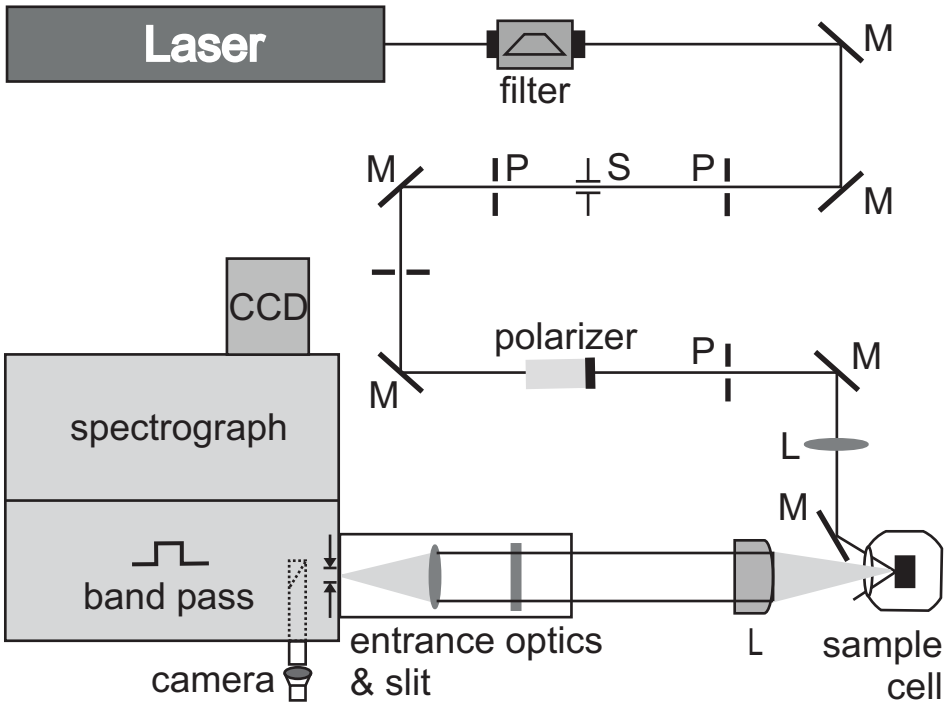

Figure 2.3: Sketch of a Raman scattering experiment, from [4].

The basic setup for Raman spectroscopy is sketched in Fig. 2.3. Four different lasers are available in the setup that supply the following laser lines:

- an Ar-Kr ion laser (Innova 70 Spectrum) with selected laser lines at $\lambda = 488$ nm, 514 nm, 568 nm and 647 nm; $P_{max} = 10$ mW,
- a He-Ne laser (Melles Griot) with $\lambda = 632.8$ nm; $P_{max} = 8$ mW,
- a frequency-doubled Nd:YAG laser (Coherent) with $\lambda = 532.1$ nm; $P_{max} = 20$ mW,
- a diode pumped solid state laser (Oxxius) with $\lambda = 561$ nm; $P_{max} = 60$ mW.

The laser light first passes through a filter that discriminates side lines (plasma lines) of the Ar-Kr ion laser and the He-Ne laser, which otherwise could dominate

the Raman spectrum. After the beam is being reflected on several mirrors (M) and passed through pinholes (P), a polarizer ($\lambda/2$ plate for linear polarization, $\lambda/4$ plate for circular polarization) is used to create a well-defined light polarization. Furthermore, a variable slit (S) is used to continuously tune the power of the laser light, which is measured by a power meter. The typical desired laser power ranges from 1 – 10 mW to avoid heating effects on the sample. The beam is finally guided and focused onto the sample with a spot diameter of about 100 μm in quasi backscattering geometry (i.e. perpendicular to the scattering plane of the sample). The inelastically scattered light is collected by a lens that focuses the signal onto the entrance slit of a triple grating spectrometer (Dilor XY 500). This device discriminates all elastically scattered light via a double monochromator and disperses the Stokes- or Anti-Stokes scattered light onto a liquid nitrogen cooled back-illuminated charge-coupled device (Horiba / Jobin Yvon Spectrum One CCD-3000V). With this setup it is possible to obtain a spectral resolution of ≈ 0.3 cm^{-1} (depending on the width of the entrance slit, the spectral range and the laser wavelength) down to 10 cm^{-1}. For solids, phonons and other excitations typically occur in the range of 30 – 1000 cm^{-1}.

A second polarizer ($\lambda/2$ or $\lambda/4$ plate) in front of the entrance slit is used as an analyzer to distinguish between the different symmetry components of the scattered light. For measurements at low temperatures the samples are installed into an evacuated closed cycle cryostat (Oxford Cryomech PT405) which provides a constant helium flow and can thus cool down to a temperature of 3 K. With a variable heater the temperature can be controlled in a range from 3 K – 295 K. The cryostat is placed on top of an xyz-table. The light scattered from the sample can be redirected via a mirror in the spectrometer onto a camera. This allows an accurate positioning and focusing of the sample via the xyz-table.

Clean sample surfaces are essential for high quality Raman spectra. If the sample provides large, as-grown surfaces with edges along the crystallographic axes, wiping the surface carefully with an aceton-soaked q-tip proves to be sufficient. If the sample exhibits a layered, 2 dimensional structure, cleaving off the surface layer with a razor blade is useful to obtain a large, fresh surface. This method is especially important for samples with quickly degrading surfaces. Finally, if the sample has a 3 dimensional structure and comes without as-grown surfaces along crystallographic planes it is first necessary to orient the crystal. This can be done via x-ray diffration by the Buerger precession method [8]. Once the crystallographic axes are determined the sample is carefully polished down to the desired plane using diamond paste with four different grain sizes in successive steps until an optically flat surface is aquired. To finally remove the polishing residue, the sample is cleaned first in isopropanol and subsequently in aceton for about 20 minutes in an ultrasonic bath.

To minimize signals originating from behind the samples in case they are thin, small or semi-opaque, a sample holder with a hole is available. Furthermore, a holder was constructed that allows rotations around one axis of the sample inside the cryostat via magnetic coupling to an external handle, see Fig. 2.4. In this

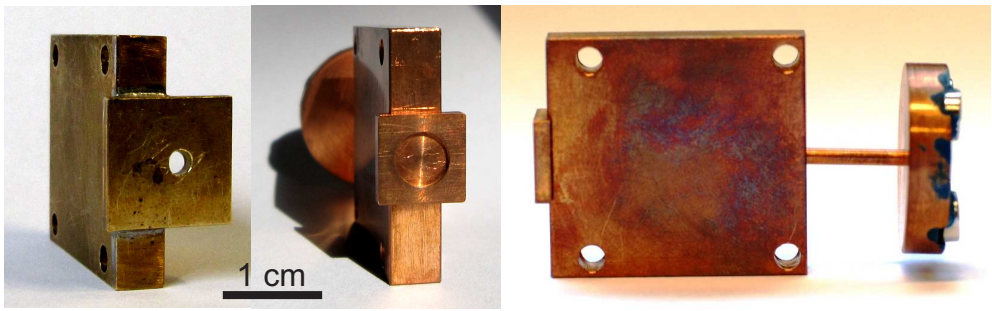

Figure 2.4: left: sample holder with hole (brass); center and right: rotational sample holder (copper).

way, the angular dependencies of the symmetry components can be conveniently studied even at low temperatures. The samples are generally fixed onto the sample holder by a stripe of double-sided adhesive tape together with a small drop of silver paste between the sample edge and the holder to guarantee thermal conduction to the base plate of the cryostat.

Chapter 3

Properties of spin liquid systems

In most solids with magnetic correlations, magnetic order sets in below characteristic order temperatures, i.e. when thermal fluctuations are weaker than the correlation strength. Through establishing order, the system undergoes a symmetry breaking. Its new (ground) state can be characterized by new bosonic excitations, such as magnons or singlet-triplet excitations. The kind of ground state that forms at low temperatures, e.g. longrange (anti-)ferromagnetic order or the formation of dimers, depends on the system's properties and can be tuned by parameters such as pressure, external magnetic field or doping. In between two phases, however, it can be possible to establish a spin liquid state down to lowest temperatures (see Fig. 3.1). A spin liquid is the magnetic equivalent to conventional liquids, in that spin-spin correlations are non-static and decay on short length scales. Upon lowering the temperature thermal fluctuations are replaced by quantum fluctuations. If they remain strong enough down to lowest temperature, no long range order will occur. This state can be realized by tuning a parameter, e.g. to lower the dimensionality of the system:

In 1966, Mermin and Wagner formulated what is known today as the Mermin-Wagner theorem [9]. It states that *no magnetic long-range order can develop in magnetically isotropic systems with a dimension of 2 or lower at finite temperatures*.

Instead, these systems can exhibit a number of interesting ground states, such as the resonating valence bond (RVB), the valence bond solid (VBS) or the valence bond crystal (VBC) state, in which new exotic, fractional excitations and unusual spin dynamics [10] can occur, some of which are yet to be fully understood. In a RVB ground state, fluctuating $S = 0$ dimer bonds cover the lattice. The ground state can be described as a superposition of all possible dimer configurations, in analogy to Pauling's valence bond model [11]. A valence bond crystal, on the other hand, exhibits some short ranged correlations between the valence bond-like dimer formations, thus introducing an anisotropy in the plane.

Very early on, P. W. Anderson speculated about the relation between the resonating valence bond and high temperature superconductivity in cuprates [12]. This motivated theorists to intensively investigate low-dimensional model sys-

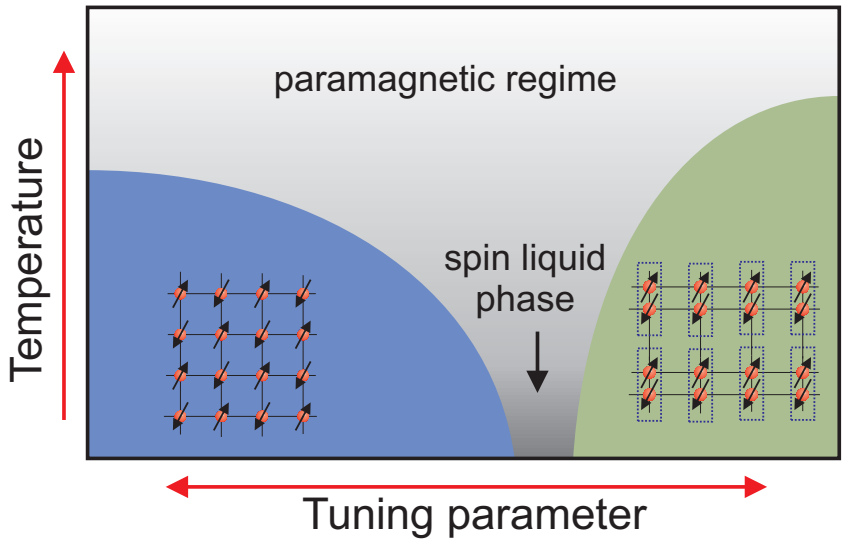

Figure 3.1: Schematic phase diagram for solids with magnetic correlations.

tems. Only recently, experimental realizations of compounds close enough to these models have made it possible to study the properties of quantum spin liquids experimentally.

The Heisenberg Hamiltonian proves to be a good description of the magnetic interaction between neighboring ions i and j in correlated transition metal oxides. It has the following form:

$$\mathcal{H} = -J \sum_{i,j} \hat{S}_i \cdot \hat{S}_j \tag{3.1}$$

where J is a measure for the exchange interaction. This Hamiltonian is obtained directly from the Hubbard model for the case of strong on-site repulsion U compared to the kinetic energy of the electrons t ($U \gg t$) and half-filling, i.e. one spin per site.

In the following, different spin arrangements will be discussed, that allow for a quantum spin liquid.

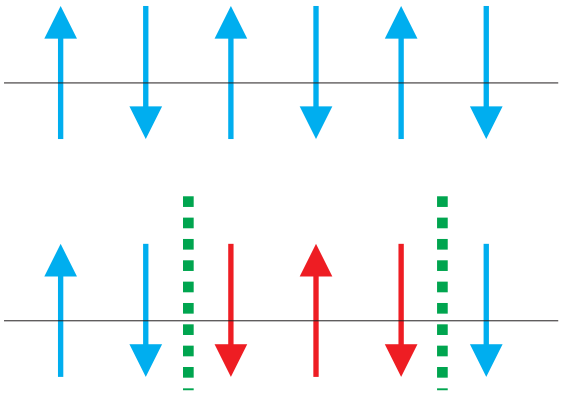

Figure 3.2: Spinon excitation (or domain walls) in the one dimensional $s = 1/2$ chain.

3.1 Spin chains and spin dimers

Consider an infinite one dimensional chain of antiferromagnetically coupled $s = 1/2$ ions. This is realized experimentally in systems with strong, isotropic magnetic interactions along one direction and negligible magnetic interactions along all other directions. At high temperatures ($T \gg J$), thermal fluctuations dominate over any magnetic order. However, as the system gets cooled down, magnetic order on a short length scale with algebraically decaying correlations along the chains starts to appear. Upon exciting this state via the flip of a spin, one creates new quasi particles, so-called spinons, that can be considered as domain walls. These spinons are created in pairs, to either side of the flipped spin (see Fig. 3.2). They are massless and carry the spin $s = 1/2$. In 1931, this 1-dimensional spin chain system was successfully described by the Bethe ansatz [13]. It was shown that spinons are deconfined – they can move apart without energy loss along perfect one dimensional, isotropic spin chains. Furthermore, excitations exist with vanishingly small energies. Hence, the excitation spectrum is gapless (see Fig. 3.3). It consists of a two-spinon continuum contained within two dispersion curves. These were calculated by des Cloizeaux & Pearson [14], and Faddeev & Takhtajan [15], and are given by

$$\omega(k) = \frac{\pi}{2} J \left|\sin(k)\right| \tag{3.2}$$

$$\omega(k) = \pi J \left|\sin(k/2)\right| \tag{3.3}$$

In the case of dimers the spatial anisotropy is broken in the ground state as every two neighboring spins pair up and form one dimer with a singlet ($S = 0$) configuration. This is realized, e.g., in spin chains with spin-Peierls instabilities, which lead to alternating exchange interactions. In this case, the Hamiltonian can be written as

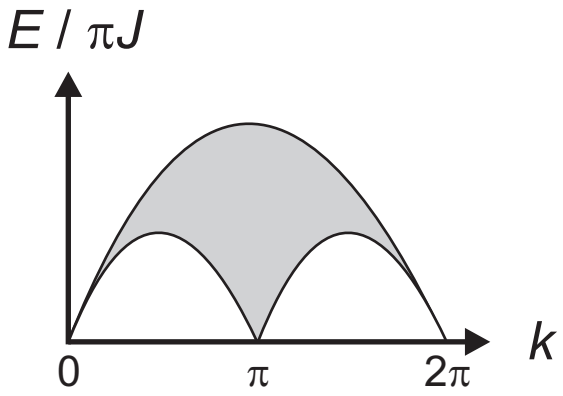

Figure 3.3: Spinon dispersion and continuum for the isotropic one dimensional $s = 1/2$ chain.

$$\mathcal{H} = -J \sum_i (1 + \delta(-1)^i) \hat{S}_i \cdot \hat{S}_{i+1} \tag{3.4}$$

where δ is a measure for the anisotropy, as the exchange interaction alternates between $J - \delta$ and $J + \delta$. Another possibility for introducing dimerization is a second, next-nearest neighbor exchange $J' = \alpha J$, which leads us to

$$\mathcal{H} = -J \sum_i \hat{S}_i \cdot \hat{S}_{i+1} + \alpha \hat{S}_i \cdot \hat{S}_{i+2} \tag{3.5}$$

In both cases, the elementary excitation is a magnon, consisting of a transition from the singlet ground state into a triplet ($S = 1$) state by creating two parallel oriented spins on a dimer. In this case, the excitation is no longer gapless, but proportional to the magnetic exchange interaction J. In the limit of strong anisotropy ($\delta \to 1$), the gap becomes largest ($2J$) and the dispersion curve nearly flat.

3.2 Triangular and kagome lattices

A concept for suppressing long-range magnetic order and decreasing spin-spin correlation lengths is by introducing geometric frustration. Frustration occurs when the magnetic ions are arranged in a way that it is impossible to simultaneously satisfy all exchange interactions. This situation is illustrated most dramatically for the case of an equilateral triangle (see Fig. 3.4). Extending this triangular motif onto a crystal lattice yields in 2 dimensions either a triangular (edge sharing) or kagome (corner sharing) lattice, and in 3 dimensions a pyrochlore structure of corner sharing tetrahedra. In general, a smaller coordination number yields a stronger degree of geometric frustration. Therefore, the kagome lattice is one of the most promising systems for realizing a 2-dimensional spin liquid.

In the classical limit ($s \to \infty$) the ground state of both the triangular and the kagome lattice is reached when every triangle contains a spin singlet ($S = 0$) with

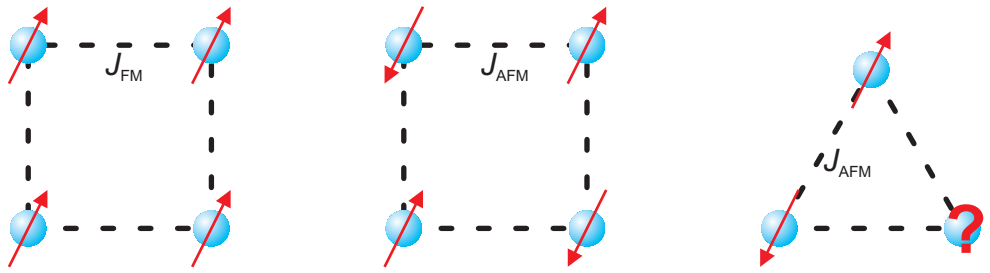

Figure 3.4: Spin arrangements for 2 dimensional $s = 1/2$ geometries. Left: ferromagnetic square lattice, center: antiferromagnetic square lattice, right: antiferromagnetic triangle.

all three spins pointing 120° away from each other. This ground state ("compromize state") has a macroscopically large degeneracy, as the global spin orientation is fully undetermined. Furthermore, spin rearrangements leading from one $S = 0$ to another $S = 0$ configuration are possible at an arbitrarily small energy cost. Therefore, the excitation spectrum is gapless for classical spins [16]. In addition to the global spin orientation, the chirality of the spin triangles is not fixed, either. It is thus possible, to decorate a kagome lattice with the same chirality for each triangle, or with an alternating, staggered chirality, which leads to an enlarged $\sqrt{3} \times \sqrt{3}$ unit cell. It was shown that for the $s = 3/2$ kagome lattice compound $Y_{0.5}Ca_{0.5}BaCo_4O_7$ the latter configuration is favoured due to its enhanced degeneracy and entropy. Through the principle of *order by disorder* [17], zero energy weathervane modes – collective rotations of spins on a hexagon – are observed in this compound [18].

For kagome lattices in the quantum spin limit ($s = 1/2$), which shall be one central point of this thesis, a 120° alignment of spins as a quantum state is not realized. Here, both VBC [19] and gapped or gapless RVB cases [20, 21] have been discussed as ground states. A VBC displays a certain bond order. Exciting this state by breaking up a bond therefore costs a finite energy as the bonds are correlated over a finite length scale. The excitation is integer $S = 1$, thus bosonic, and it corresponds to a transition from a singlet to a triplet spin state. Due to the bond-bond correlations the excitation costs a finite amount of energy, similar to dimerized 1-dimensional spin chains. The excited spins are still correlated and cannot move apart without energy loss. On the other hand, the RVB state is a superposition of every possible dimer bond covering, see Fig. 3.5. Creating an excitation from this ground state corresponds to breaking up one bond and thus releasing two $s = 1/2$ spinons. Two possible scenarios are currently discussed: independent (deconfined) and weakly correlated spinons. For the latter case algebraically decaying correlations are proposed [22].

An important issue is the robustness of spin liquid states against perturbations. Experimental realizations are always plagued by defects, which could easily stabilize magnetic order. A second drawback is the presence of small

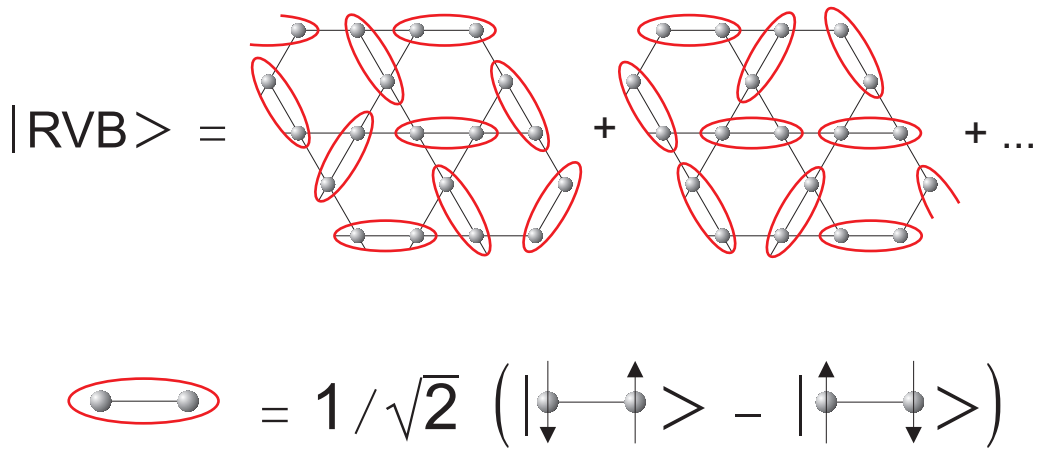

Figure 3.5: Singlet bond coverings in the Resonating Valence Bond state for the $s = 1/2$ Heisenberg antiferromagnet on a kagome lattice.

distortions and interlayer coupling in many kagome lattice compounds. These distortions introduce spatial anisotropies in the magnetic exchange interactions, that could stabilize magnetic order or a dimerized ground state as well. Finally, even in a structurally perfect kagome lattice spin anisotropies, induced by Dzyaloshinsky-Moriya (DM) interactions, can be anticipated. It was estimated that only for DM contributions larger than $0.1 \cdot J$ a long range ordered ground state is induced [23].

The model system for spin liquid states first proposed by P. W. Anderson was the $s = 1/2$ triangular lattice antiferromagnet. However, it is now established that a perfect triangular lattice forms a non-collinear 120° ordered ground state [24]. However, small deviations from the perfect triangular lattice, such as slightly different exchange interactions J_1 and J_2 can drive the system into a state of long range order, spin liquid, gapped dimer, or VBC, depending on the ratio of J_1 and J_2 [25].

Chapter 4

The 1D quantum spin chain $TiPO_4$

$TiPO_4$ realizes a nearly ideal 1D spin chain with a single dominating magnetic exchange direction and a low spin quantum number of $s = 1/2$. It shows a spin-Peierls instability below $T_{SP} = 74$ K and strong lattice dynamics over a large temperature regime between 111 K and T_{SP}. In particular, this system allows us to tune the magnetic excitation spectrum from fermionic to bosonic via changing the temperature. We study the interplay of lattice and magnetic degrees of freedom, discuss a high energy excitation of mixed electronic and magnetic origin, and compare it to TiOX (X = Cl, Br) [26].

4.1 Crystal structure

Single crystals of $TiPO_4$ were grown by the group of R. Glaum at the University of Bonn. The investigated sample has a size of about $0.5 \times 0.5 \times 1$ mm^3. Its optically flat, as-grown surface shares one edge with the crystallographic c axis, while the other, perpendicular edge lies within the ab plane, in accordance with the upper part of Fig. 4.1.

$TiPO_4$ crystallizes in the orthorhombic space group $Cmcm$, realizing 1D chains of edge sharing TiO_6 octahedra along the c direction. The Wyckoff positions of the atoms within the unit cell together with their allowed Raman active phonon modes [27] are given in Table 4.1.

In total, the phonon spectrum consists of $\Gamma_{Raman} = 5{\cdot}A_g{+}4{\cdot}B_{1g}{+}2{\cdot}B_{2g}{+}4{\cdot}B_{3g}$ Raman active modes. Their respective Raman tensors are given by:

$$A_g = \begin{pmatrix} a & 0 & 0 \\ 0 & b & 0 \\ 0 & 0 & c \end{pmatrix}, B_{1g} = \begin{pmatrix} 0 & d & 0 \\ d & 0 & 0 \\ 0 & 0 & 0 \end{pmatrix}, B_{2g} = \begin{pmatrix} 0 & 0 & e \\ 0 & 0 & 0 \\ e & 0 & 0 \end{pmatrix}, B_{3g} = \begin{pmatrix} 0 & 0 & 0 \\ 0 & 0 & f \\ 0 & f & 0 \end{pmatrix}.$$

Since the spin chains are formed along the c direction, we aligned the crystal in such a way that the laboratory x axis coincides with the crystallographic c

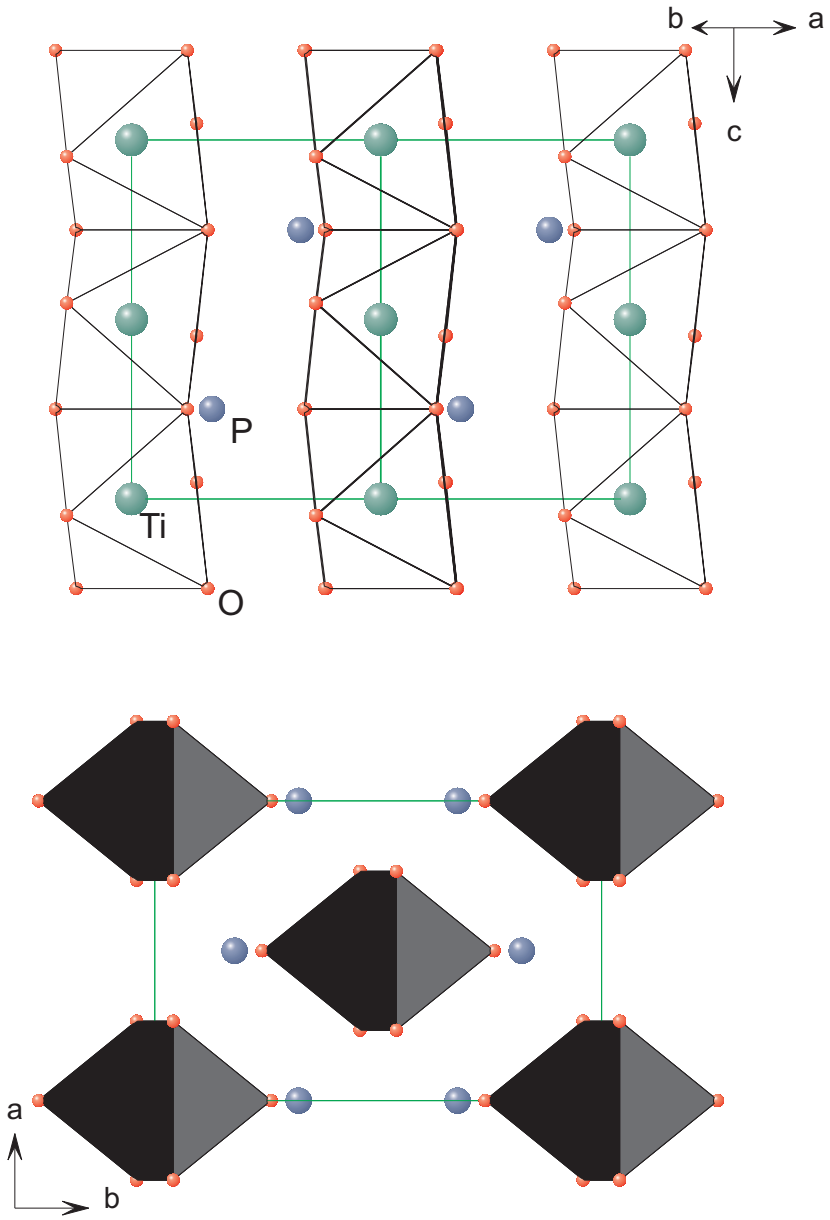

Figure 4.1: Crystal structure of $TiPO_4$. Upper panel: ribbons of edge-sharing TiO_6 octahedra form 1D chains along the crystallographic c axis. The plane displayed in the upper panel corresponds to the orientation of the measured sample. The lower panel displays the crystallographic ab plane.

Table 4.1: Symmetry analysis for $TiPO_4$

Atom	Wyckoff position	allowed phonon modes
Ti(1)	4a	–
P(1)	4c	1 A_g + 1 B_{1g} + 1 B_{3g}
O(1)	8g	2 A_g + 2 B_{1g} + 1 B_{2g} + 1 B_{3g}
O(2)	8f	2 A_g + 1 B_{1g} + 1 B_{2g} + 2 B_{3g}

axis. In this way we can probe possible magnetic excitations most sensitively. The perpendicular y axis lies within the crystallographic ab plane, i.e. canted by 45° from the a and from the b axis. Following the symmetry analysis, we expect 5 A_g modes in xx polarization, 5 A_g + 4 B_{1g} modes in yy polarization and 2 B_{2g} + 4 B_{3g} modes in crossed yx polarization. Fig. 4.2 and Fig. 4.3 show the spectra obtained in different polarizations at room temperature ($T = 295$ K) and at $T = 10$ K, respectively, together with the symmetry assignment for each phonon mode. An overview of the phonon frequencies together with their symmetry assignments can be found in Table 4.2. Due to the small size of the single crystal and its semi-transparent property, the incoming light can get scrambled. This partially lifts the selection rules. The symmetry assignment of a few modes (marked by an asterisk) is therefore ambiguous. Nevertheless, the observed 13 phonon modes at room temperature are in good agreement with the 15 phonon modes according to the symmetry considerations. Upon cooling to lowest temperature, the number of phonon modes increases to 24, with several very intense new modes of A_g symmetry appearing. This observation evidences a lowering of the crystal symmetry towards low temperatures. First principle density functional theory calculations were carried out in order to predict the low temperature crystal structure of $TiPO_4$ [28]. It was found that an energy minimum is reached for the $Pmmn$ space group, which results in a total of 36 Raman active phonon modes ($\Gamma_{Raman} = 12A_g + 5B_{1g} + 9B_{2g} + 10B_{3g}$). Indeed, we do observe 12 phonon modes of A_g symmetry at low temperature, together with 4 B_{1g} phonons. The 12 missing phonon modes (in total 24 out of 36 modes are observed) – mostly of B_{2g} and B_{3g} symmetry – are likely shoulders of / or overlapping with modes of strong intensity, or too weak in intensity to observe.

4.2 Electronic and magnetic properties

The Ti^{3+} ions in $TiPO_4$ contain a single $3d$ electron in the degenerate t_{2g} orbital states. The spins are coupled via super-exchange with the main antiferromagnetic exchange interaction $J_1 = -965$ K running along the chain (c) direction, as measurements of the magnetic susceptibility revealed. Subsequent DFT calculations found an exchange interaction of $J_{DFT} = -988$ K. This value, however, should

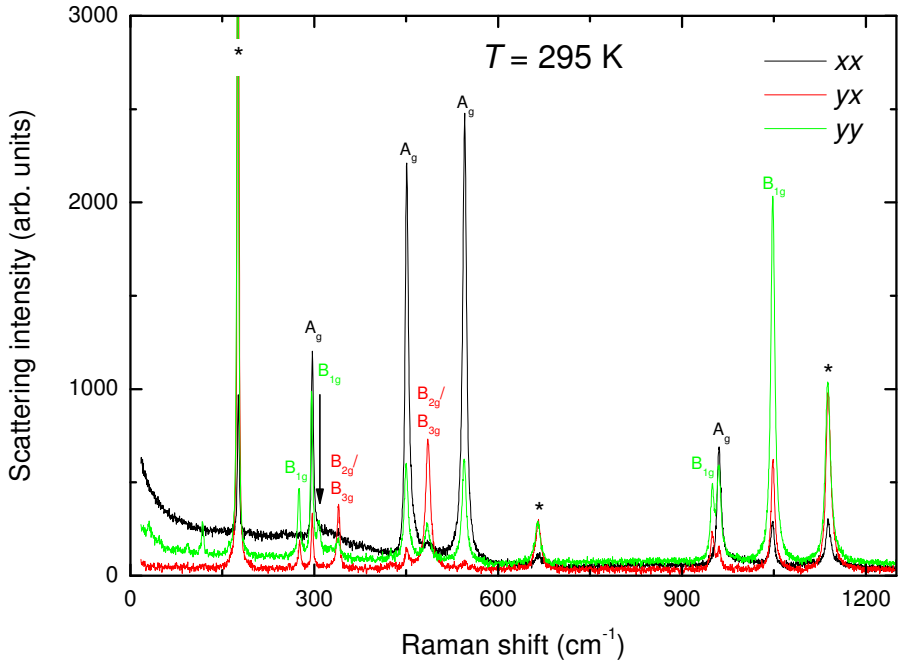

Figure 4.2: Phonon spectrum of $TiPO_4$ at room temperature in different polarizations.

be taken with caution, as DFT generally tends to overestimate the magnetic exchange in low dimensional spin systems. Nevertheless, we note the good agreement between experiment and theory. A second, next-nearest-neighbor interaction was found to be $J_2 = -1.4$ K and a third interchain interaction of $J_3 = -20$ K [29]. Due to the chain-like arrangement along the c axis and the dominating exchange interaction J_1 this leads to the realization of a quasi-1D $s = 1/2$ system. A broad maximum observed in magnetic susceptibility indicates the onset of short-range magnetic correlations around $T = 625$ K.

4.3 Spin-Peierls transition in $TiPO_4$

Rudolf Peierls found that in 1D chains of equally distanced atoms with 1 electron per site it is energetically favorable for every two ions to dimerize and thus to distort the chain. While originally only the electronic aspect was considered, it can be applicable to antiferromagnetic chains, which can undergo a transition into a nonmagnetic, dimerized ($S = 0$) ground state consequently. This so-called

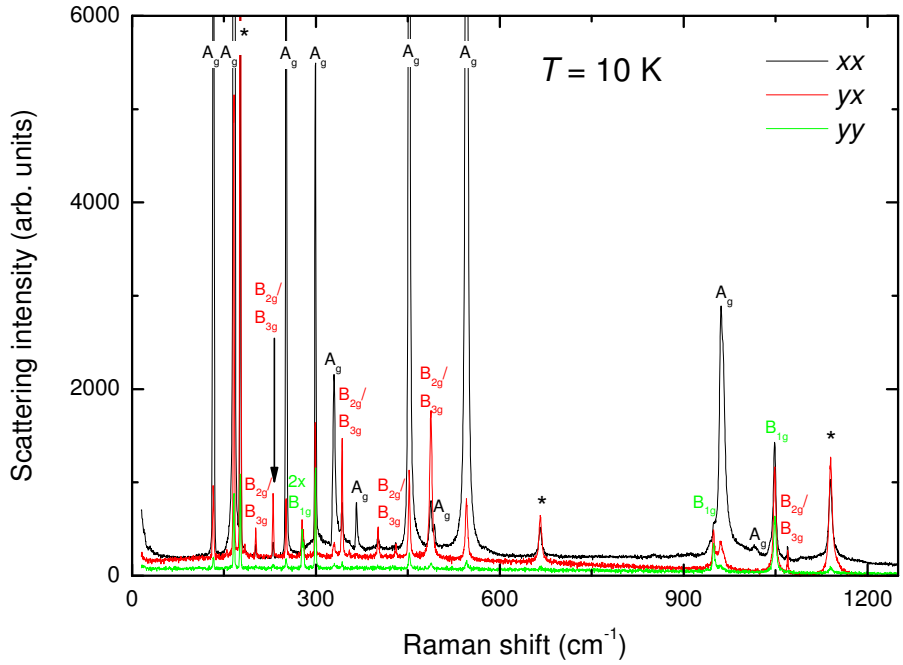

Figure 4.3: Phonon spectrum of $TiPO_4$ at 10 K in different polarizations.

spin-Peierls transition results in the opening of a spin gap. Indeed, a spin-Peierls transition was observed, e.g., in the compounds $TTFCuS_4C_4(CF_3)_4$ (with $T_{SP} = 12$ K and $J = 77$ K) [30] and $CuGeO_3$ (with $T_{SP} = 14$ K and $J = 88$ K) [31]. In $TiPO_4$ this instability leads to the dimerization of Ti^{3+} ions below $T_{SP} = 74$ K. This transition not only affects the magnetic subsystem and hence, its excitations, but also the lattice and thereby the phonons. Consequently, Raman scattering is a suitable probe to study the spin-Peierls transition in $TiPO_4$.

In a previous magic angle spinning ^{31}P nuclear magnetic resonance (NMR) study [29], two different P environments were observed below T_{SP}, owing to the structural dimerization. At high temperatures, there is a single P environment due to the uniform chain structure. However, in an intermediate temperature regime $T^* = 111$ K $> T > T_{SP} = 74$ K, a broad continuum of different P environments occurs. This signals the existence of an intermediate incommensurate phase. From a fit to the molar magnetic susceptibility χ_m, a spin gap of $\Delta = 830$ K (425 K) was estimated for the dimerized (incommensurate) regime [28]. This is in contrast to previously investigated spin-Peierls compounds, like $CuGeO_3$ and $TTFCuS_4C_4(CF_3)_4$, which transition into the dimerized phase without passing through an intermediate regime. TiOCl, on the other hand, evidences

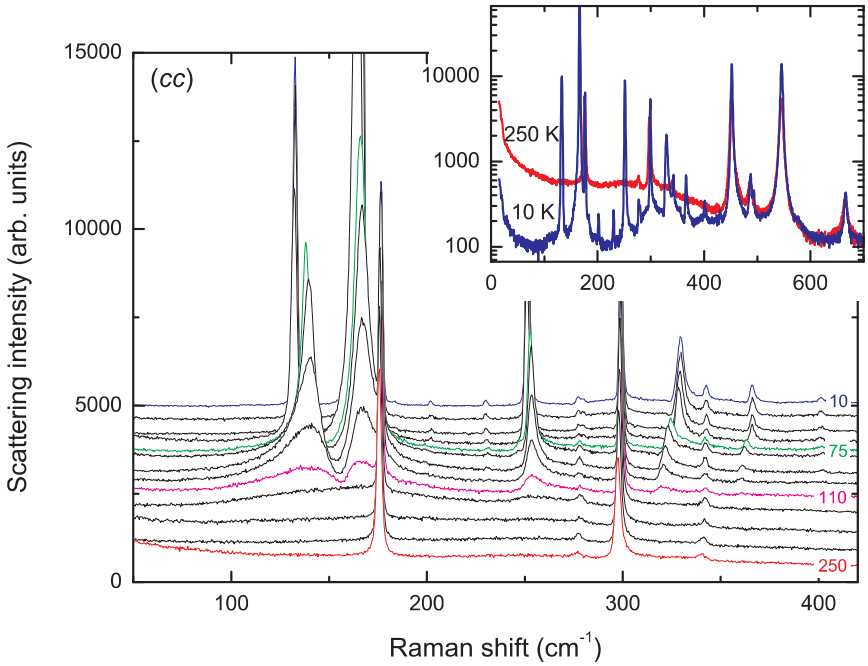

Figure 4.4: Raman spectra collected at T = 10, 30, 50, 70, 75, 80, 90, 100, 110, 120, 150, 200, and 250 K in cc polarization, i.e. along the chain direction. The depicted spectra range from 50 to 420 cm^{-1}. They are shifted in intensity for clarity. The inset shows a direct comparison between the 10 K and 250 K spectrum on a logarithmic intensity scale and for a wider spectral range [26].

an incommensurate regime above T_{SP}. This was originally attributed to strong orbital fluctuations, however, subsequent investigations revealed that rather frustration induced by comparably strong interchain interactions accounts for the incommensurate order [32]. For $TiPO_4$, the interchain interactions are negligible. Hence, another mechanism, possibly fluctuations of degenerate orbital t_{2g} states, drives the incommensurate transition in this compound. This peculiarity could lead to unusual features in $TiPO_4$.

4.4 Phonon anomalies

To gain an insight into the lattice dynamics, we look at the temperature dependence of the phonon spectra. An overview of the low energy regime (50 – 420 cm^{-1}) can be seen in Fig. 4.4, while in Fig. 4.5 we plot the energy of all phonons as a function of temperature. In particular, the latter figure highlights the enhanced lattice dynamics in the intermediate temperature range, i.e. in the incommensurate phase. For temperatures both above T^* and below T_{SP}, the lattice evidences rather static behaviour. The parameters of the four most intense new phonon

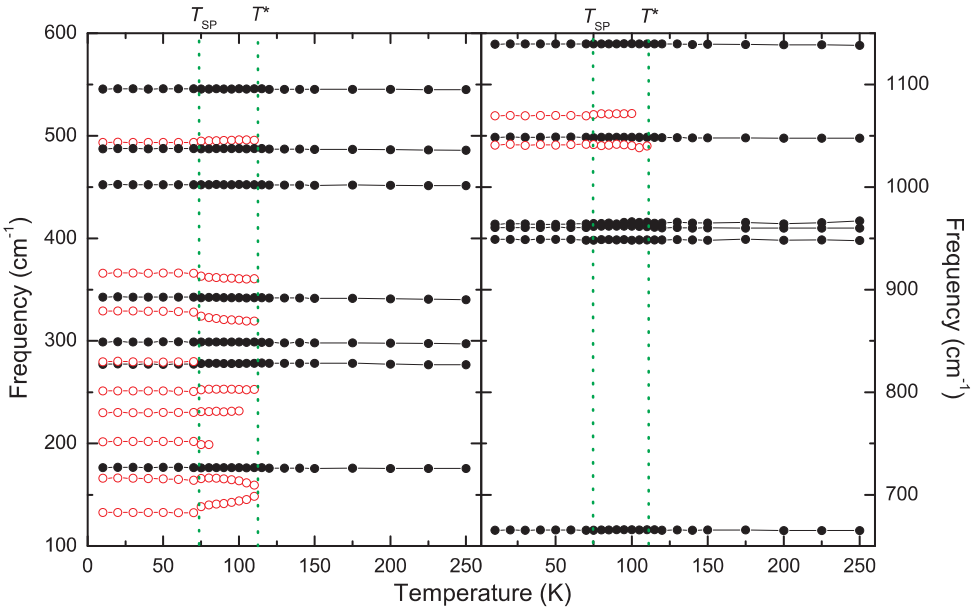

Figure 4.5: Temperature development of the phonon frequencies. Changes at the two characteristic temperatures T^* and T_{SP} are clearly visible together with the occurence of new phonon modes, marked by red, open circles [26].

modes are plotted over temperature in Fig. 4.6.

In spin-Peierls systems, spin-phonon coupling can account for strong lattice dynamics. To estimate the spin-phonon coupling in $TiPO_4$, we derive the spin-spin correlation function $\langle s_i, s_j \rangle_\chi$ from the magnetic susceptibility $\chi_m(T)$ [29]. Considering only nearest neighbor interactions, the spin-spin correlation function can be written as [33]

$$\langle s_i, s_j \rangle_\chi = \frac{k_B T \chi(T)}{N_A g^2 \mu_B^2} - \frac{s(s+1)}{3} \tag{4.1}$$

with $g = 1.94$. In Fig. 4.7 we plot the correlation function (red line) together with the frequency shift of the A_g mode at 132 cm^{-1} (solid black squares). Both quantities show a comparable temperature evolution. We can now estimate the spin-phonon coupling constant λ according to

$$\Delta\omega = \lambda \cdot \langle s_i, s_j \rangle_\chi \tag{4.2}$$

which yields a value of the order of $\lambda_{132} \approx 100$ cm^{-1}. The other three phonon modes with strong dynamics at 166, 250, and 330 cm^{-1} show similar temperature dependencies. Their corresponding spin-phonon coupling constants amount to $\lambda_{166} \approx -40$ cm^{-1}, $\lambda_{250} \approx 15$ cm^{-1}, and $\lambda_{330} \approx -80$ cm^{-1}. These values are larger than those in the spin-Peierls system $CuGeO_3$ (albeit comparable in magnitude), where spin-phonon coupling constants of -10, 40, -21, and -8 cm^{-1} where found [34].

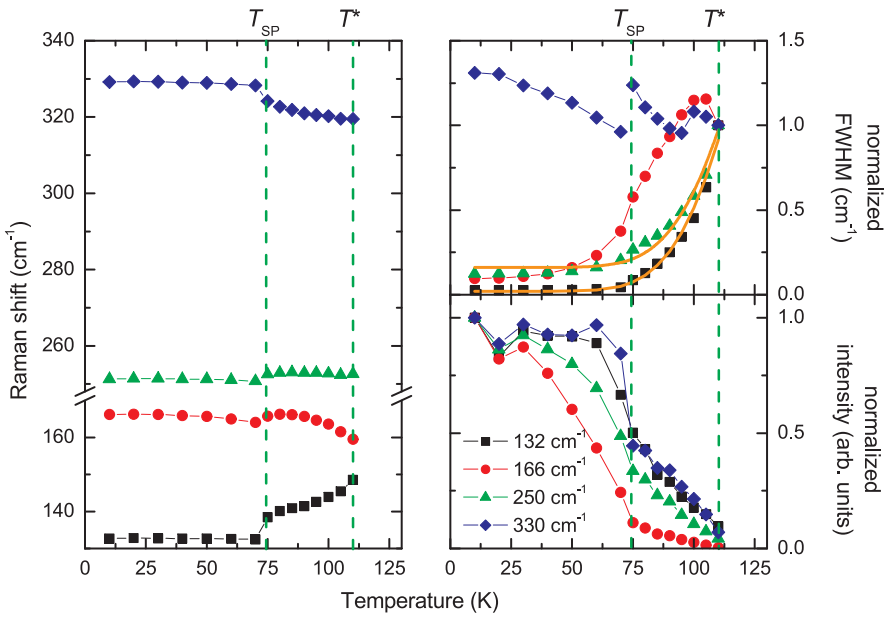

Figure 4.6: Temperature development of the phonon parameters frequency, normalized linewidth (full width at half maximum) and normalized intensity for the A_g modes at 132 cm^{-1} (black squares), 166 cm^{-1} (red circles), 250 cm^{-1} (green triangles), and 330 cm^{-1} (blue diamonds). The solid orange lines correspond to fits to the linewidths [26].

Further evidence for a strong coupling between the lattice and spin subsystems can be extracted by inspecting the linewidths. Both modes at 132 and at 250 cm^{-1} broaden exponentially above T_{SP}. We can describe this behaviour by an activated function

$$\Gamma(T) = \Gamma_0 + A \cdot e^{U/k_B T} \tag{4.3}$$

with Γ_0 and A being phonon dependent constants, and U corresponding to a potential barrier of lattice distortions. The fit curves are shown in Fig. 4.6. With a shared fit parameter for the energy barrier we obtain a value of $U = (662 \pm 48)$ K. In a SP mechanism, the magnetic binding energy (2Δ) should exceed this barrier and thus we can use this barrier to derive the SP gap $\Delta = (331 \pm 24)$ K.

We can separate the phonon modes into three regimes, in accordance with a previous infrared study on $TiPO_4$ [35]. Phonons below ~ 400 cm^{-1} are related to displacements originating from TiO_6 units, and phonons above ~ 500 cm^{-1} are related to PO_4 modes. Phonons occuring in the intermediate frequency range are related to both, due to the coupling of the building blocks. Hence, the strongest changes in the Raman spectra with temperature occur in the low energy regime, reflecting the modulation of Ti-Ti distances and angles. Similar lattice dynamics have been reported, e.g., in the quantum spin system TiOCl [36]. Here, a dimerized ground state is reached after passing through a temperature regime of strong

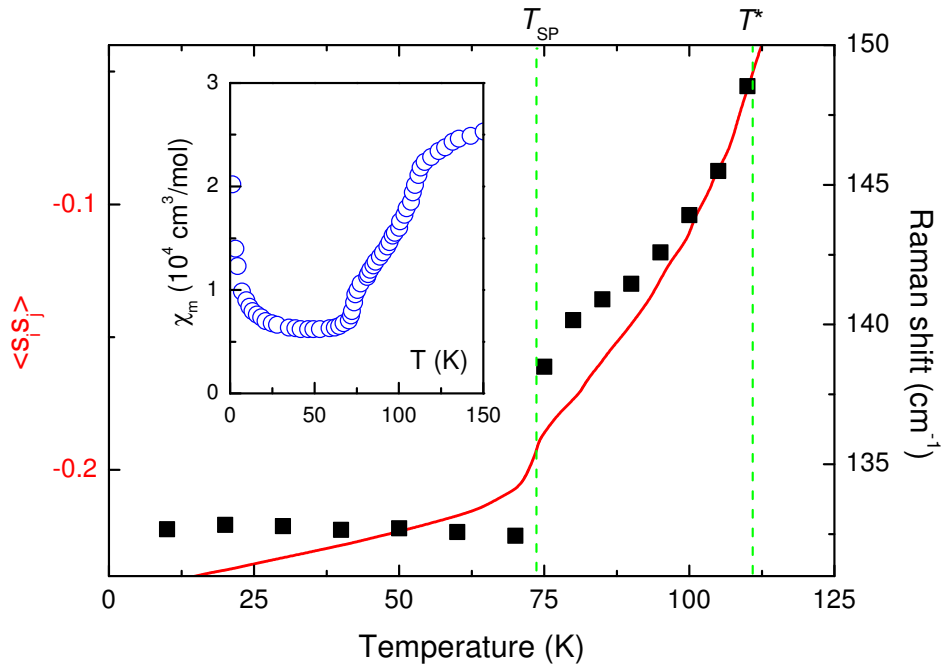

Figure 4.7: Comparison of the spin-spin correlation function $\langle s_i, s_j \rangle_\chi$ (solid red line) as obtained from magnetic susceptibility measurements (see inset, [29]) with the temperature evolution of the phonon frequency for the 132 cm^{-1} A_g mode (solid black squares).

fluctuations in the phonon sector.

4.5 Magnetic scattering in $TiPO_4$

In the left panel of Fig. 4.8 the Raman spectra at four different temperatures are plotted, ranging from 10 to 250 K. At 10 K, one observes a broad background of magnetic origin with a clear onset energy of 250 cm^{-1}, highlighted by the dashed blue line. Upon increasing the temperature, this background shows distinct changes as the spectral weight increases and shifts towards lower energies. In the inset of Fig. 4.8 we trace the temperature evolution of the continuum's integrated intensity. Upon the opening of the spin gap Δ the spectral weight of the magnetic scattering decreases exponentially with temperature. By applying an exponential fit function (red line) $\Gamma = B + C \cdot e^{-\Delta/k_B T}$ to the data points below $\approx$ 110 K, we obtain a gap size of $\Delta = (311 \pm 48)$ K. Note that for this analysis, only the spectral weight up to 600 cm^{-1} ($\widehat{=}$ 860 K) was taken into account as the influ-

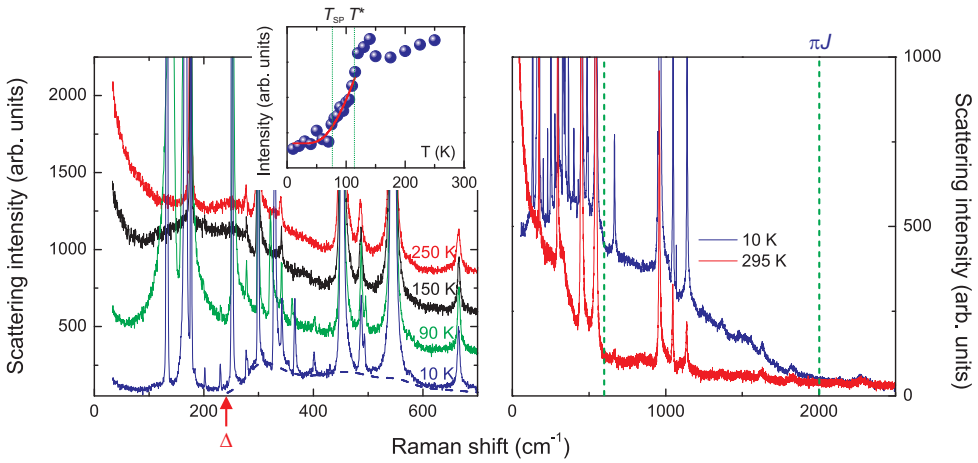

Figure 4.8: Left panel: Raman spectra obtained at 10, 90, 150, and 250 K. The dashed blue line denotes the magnetic scattering continuum at 10 K. The spectra are shifted in intensity for clarity. The inset depicts the integrated intensity of the continuum as a function of temperature. Right panel: Raman spectra obtained at base- and at room temperature. Shown is the complete spectral range of the magnetic scattering continuum. The dashed green lines mark the cut-off energies for the pronounced spectral weight around 600 cm^{-1} and the broad spinon-like continuum around 2000 cm^{-1} [26].

ence of the temperature (10 – 295 K) surely is most dramatic in this low energy regime.

A second, independent determination of the gap size can be achieved directly from the spectra, since a spin gap suppresses all magnetic scattering below the gap energy. We observe the onset of the magnetic scattering at lowest temperatures around 250 cm^{-1}. This corresponds to a gap size of $\Delta \approx 360$ K, which is in good agreement with the gap size obtained from both the exponential fit and the phonon linewidth analysis. Hence, the averaged spin gap value in $TiPO_4$ is $\Delta \approx 330$ K. While this value is much smaller than the gap extracted from a fit to the magnetic susceptibility ($\Delta_{sus} = 830$ K, [28]), it is important to note that we determine the gap size from three different, independent measurands. The susceptibility, on the other hand, might be plagued by additional terms due to imperfections or perturbations, that the model-based fit could not account for.

For a pure spin-Peierls mechanism, the ratio between spin-gap and transition temperature is given by $2\Delta/T_{SP} = 3.5$, based on a BCS-type relation [37]. In $CuGeO_3$, the ratio corresponds to ~ 3.4, hence its physics can be well described by a pure spin-Peierls mechanism. For TiOCl, on the other hand, the ratio amounts to 10 – 15, which cannot be explained by a simple spin-Peierls mechanism. Instead, substantial interchain interactions ($J' \sim 0.2 \cdot J$, [38]) are present, compared to $CuGeO_3$. This is contrasted by $TiPO_4$, which is dominated by a single exchange interaction along the spin chains. Yet, the ratio $2\Delta/T_{SP}$ yields 9.

Instead, the orbital degrees of freedom play a decisive role in this compound, as they are relatively close in energy to the magnetic subsystem. The interplay of these two quantities will be discussed further below.

Here, we also note the asymmetric, Fano-like line shape of phonon modes in the low energy range, due to a coupling between the phonons and the continuum of magnetic excitations (see, e.g., Fig. 4.4). The right panel of Fig. 4.8 extends the energy range up to 2500 cm^{-1} for the spectra at 10 K and at room temperature (295 K), showing the complete magnetic continuum. The upper limit of the spectral weight is around 2000 cm^{-1}. In the left panel of Fig. 4.9 we sketch the dispersion curve of magnetic excitations in a gapped 1D spin chain system, while in the right panel a rough draft of the resulting Raman spectrum is shown (dashed green line), together with a fit to the magnetic continuum measured at $T = 10$ K (solid black line). In accordance with the schematic dispersion curve, the low energy regime of the magnetic scattering in the dimerized phase corresponds to bosonic singlet to triplet excitations, while the high energy regime is governed by spinon excitations of fermionic nature. When the system transitions from a dimerized to a uniform spin chain upon heating through T_{SP}, the spin gap closes and hence, the low-energy bosonic excitations disappear. Instead, this energy regime is occupied by a diffusive, quasi-elastic tail due to thermally induced fluctuations of the magnetic energy density.

The qualitative spectrum compares very well with the calculated and the experimentally observed continuum in $CuGeO_3$ [39]. While the continuum in both systems should reach up to $2 \cdot \pi J$ for a 2 particle scattering process at the Brillouin zone boundary, thermal fluctuations at finite temperatures suppress scattering from the second half of the Brillouin zone ($\pi/2 < k < \pi$) and instead limit the observable range of magnetic excitations to the first half ($0 < k < \pi/2$) [39]. Hence, a filtering function $f_k = \cos^2(k/2)$ (the dotted orange line in the left panel of Fig. 4.9) is introduced. This restricts the magnetic excitations to an upper limit of $E_{max} \approx 2 \cdot \frac{\pi}{2} J$. From the observed cut-off energy, we can now extract the magnetic exchange constant as $J = 916$ K, which fits very well to the reported values from susceptibility and DFT calculations. The structure in the continuum that is observed experimentally can be ascribed to differently sized spin gaps Δ_k at different edges of the Brillouin zone.

One difference between $CuGeO_3$ and $TiPO_4$ occurs in the dimerized phase at $E < \Delta$. While the magnetic scattering intensity is totally suppressed in the former system, a finite spectral weight still remains in $TiPO_4$ (compare, e.g., the dashed green line to the fit in Fig. 4.9). We therefore assume that even at lowest temperatures not all spins are dimerized and a finite amount of free spins remain. This is in accordance with the sizeable magnetic susceptibility that remains at low temperatures (see inset of Fig. 4.7), even after subtracting a Curie-tail.

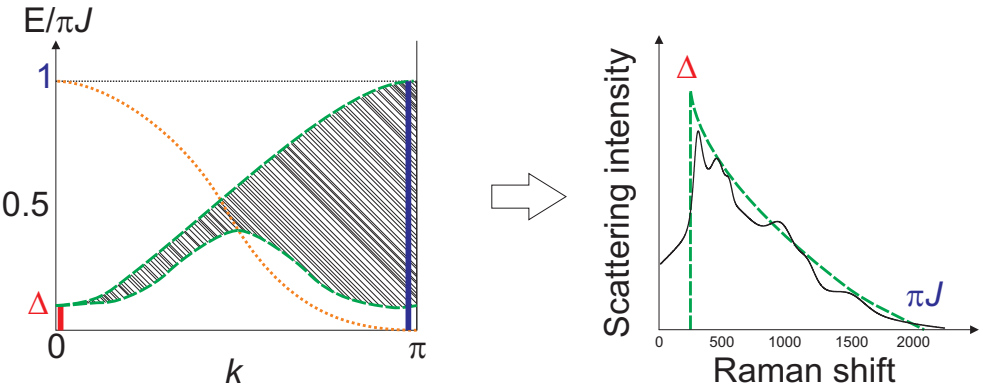

Figure 4.9: Left panel: Schematic dispersion curves with the continuum of magnon excitations in the dimerized phase with an excitation gap Δ. The dotted orange curve denotes a filtering function. Right panel: corresponding spectral weight (dashed green line) with the lower limit given by Δ and the upper limit by πJ. The solid black curve is obtained from a fit to the Raman data at $T = 10$ K.

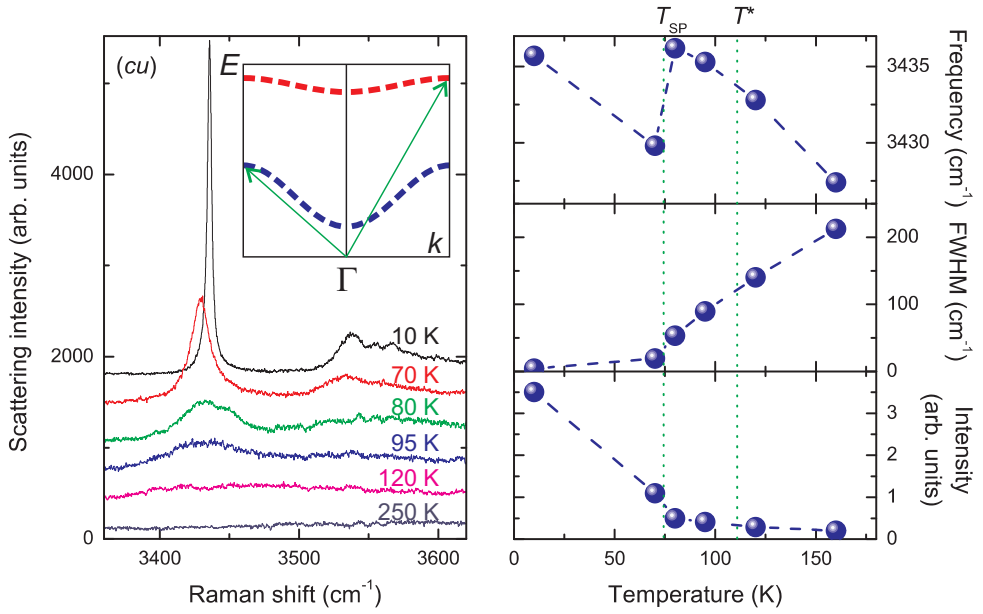

Figure 4.10: Left panel: Raman spectra of the high energy mode around 3430 cm^{-1} obtained at different temperatures in cu polarization, i.e. without analyzer, to maximize the scattering intensity. The inset sketches the scattering mechanism. Right panel: temperature development of the mode's parameters frequency, linewidth, and intensity [26].

4.6 High energy excitation in $TiPO_4$

In addition to the phonons, a high energy mode appears at 3430 cm^{-1} (shown in Fig. 4.10) with a narrow linewidth and a relatively strong intensity at low temperatures (i.e. below T_{SP}). The energy of this mode is too large for either a phonon or a magnetic scattering process. Upon increasing the temperature above the spin-Peierls transition the intensity quickly drops off, while the line width increases enormously. Furthermore, we observe a pronounced jump in energy around T_{SP}, as depicted in the right panel of Fig. 4.10. From theoretical calculations, a crystal field excitation energy of 2612 cm^{-1} ($\widehat{=}$ 0.33 eV) for the transition from the Ti^{3+} d_{xy} to the $d_{3z^2-r^2}$ level is found [40]. The energy of the magnetic exchange interaction ($J = 965$ K) corresponds to 670 cm^{-1}. Hence, a two particle process consisting of a magnetic and a crystal field excitation can account well for the observed maximum. Considering the temperature behaviour, we recall that upon increasing the temperature above T_{SP}, the system enters the incommensurate phase. Here, the magnetic excitation spectrum broadens considerably, as the spin gap starts to close. Finally, in the isotropic spin chain regime above T^*, the specific magnetic excitation energies have been replaced by a broad excitation continuum, which leads to a dramatic loss in intensity as well as a gain in linewidth for the mixed excitation at 3430 cm^{-1}. It is also noteworthy that the mixed excitation occurs only in cc polarization, i.e. with the light polarization parallel to the spin chains. No signal could be detected in either crossed or perpendicular polarization. This is a fingerprint of the magnetic contribution, which for a 1D spin chain system is only observed with the incident light polarized along the chain direction. Additionally, a change in laser line from $\lambda = 532$ nm to 561 nm had no influence on the mode's energy or the line shape, proving its intrinsic nature.

Besides the strong mode at 3430 cm^{-1}, a weaker feature is observed around 3540 cm^{-1}, which mimics the temperature behaviour of the former mode. In the related material TiOCl, a broad, high energy magnetic scattering continuum is observed which is periodically modulated in intensity by a characteristic energy of 60 – 70 cm^{-1} [36]. This modulation was attributed to a coupling of two phonon modes with strong dynamics to the spin degrees of freedom in TiOCl. In our case, the weaker feature is about 100 cm^{-1} apart from the main mode, which corresponds to the spin-phonon coupling constant λ_{132}. Hence, an interplay between the phonon at 132 cm^{-1} and the spin degrees of freedom can account for the additional scattering signal.

4.7 Conclusion

This chapter presented a Raman scattering study of the 1D spin chain system $TiPO_4$, undergoing two structural transitions, from uniform to incommensurate to dimerized. In the incommensurate phase unusual lattice dynamics are ob-

served which can be ascribed to strong spin-phonon coupling. The magnetic scattering shows a pronounced temperature dependence and can be separated into a bosonic low and a fermionic high energy part. From the low energy regime we extracted the size of the spin gap $\Delta \approx 330$ K. In contrast to other spin-Peierls systems, a significant amount of undimerized spins remain in $TiPO_4$ below the spin-Peierls transition temperature, as evidenced by a considerable spectral weight below the spin gap energy. Furthermore, a mode at high energies with a distinct temperature dependence has been attributed to an excitation of mixed electronic and magnetic nature. The strong spin-phonon coupling in $TiPO_4$ leads to a modulation of this excitation.

Table 4.2: Phonon frequencies in cm^{-1} with their respective symmetry assignments for the two structural phases measured at $T = 295$ K and at 10 K.

$T = 295$ K		$T = 10$ K		
Phonon frequency	Symmetry assignment	Phonon frequency	Symmetry assignment	Comment
		132	A_g	strong dynamics
		166	A_g	strong dynamics
175	*	176	*	
		202	B_{2g} / B_{3g}	
		230	B_{2g} / B_{3g}	
		250	A_g	strong asymmetry
276	B_{1g}	277	B_{1g}	
		280	B_{1g}	
297	A_g	299	A_g	
		330	A_g	strong dynamics
340	B_{2g} / B_{3g}	342	B_{2g} / B_{3g}	
		366	A_g	
451	A_g	452	A_g	
486	B_{2g} / B_{3g}	487	B_{2g} / B_{3g}	
		493	A_g	
545	A_g	546	A_g	
665	*	665	*	
948	B_{1g}	949	B_{1g}	
960	A_g	960	A_g	
967	A_g	964	A_g	
		1041	A_g	
1047	B_{1g}	1048	B_{1g}	
		1070	B_{2g} / B_{3g}	
1138	*	1139	*	

Chapter 5

Orbital fluctuations in the $s = 1/2$ dimer system $Sr_3Cr_2O_8$

Spin systems with several interacting quantities (such as structural, magnetic and electronic degrees of freedom) on a comparable energy scale are prone to show exotic phenomena and rich phase diagrams. In the previous chapter we discussed the interplay of spin and lattice degrees of freedom in the case of a quasi-1 dimensional chain with a spin-Peierls instability. In this chapter we investigate a compound with a 3D network of weakly interacting magnetic degrees of freedom with a spin gap. The system is orbitally degenerate at high temperatures and orbitally ordered at low temperatures, an unusually large, intermediate temperature regime is dominated by strong orbital and lattice fluctuations [41].

5.1 Crystal structure

Single crystals of $Sr_3Cr_2O_8$ were grown by A. T. M. N. Islam at the Helmholtz Zentrum Berlin (HZB) via a floating zone method. The investigated crystal was cut to a block of about $1 \times 0.5 \times 2$ mm^3 and oriented along the crystallographic c axis via single crystal Laue X-ray diffraction by D. Quintero-Castro at the HZB. To obtain an optically flat surface, the crystal was manually polished before the Raman scattering experiments, using diamond polishing paste.

The crystallographic structure of $Sr_3Cr_2O_8$ is shown in Fig. 5.1. The Cr ions are surrounded by 4 oxygen ions, forming tetrahedra. The unit cell contains three different Cr positions, each of which is occupied twice, resulting in an AA-BB-CC like stacking pattern along the c axis. At high temperatures, $Sr_3Cr_2O_8$ crystallizes in the hexagonal space group $R\bar{3}m$. At $T_S = 275$ K the compound undergoes a structural transition, as the apical oxygen ions in the tetrahedra shift from their position, thereby distorting the tetrahedra. This results in a lower, monoclinic $C2/c$ structure for $T < 275$ K [42]. In table 5.1, the Wyckoff position of each atom is listed together with the respective Raman active modes [27].

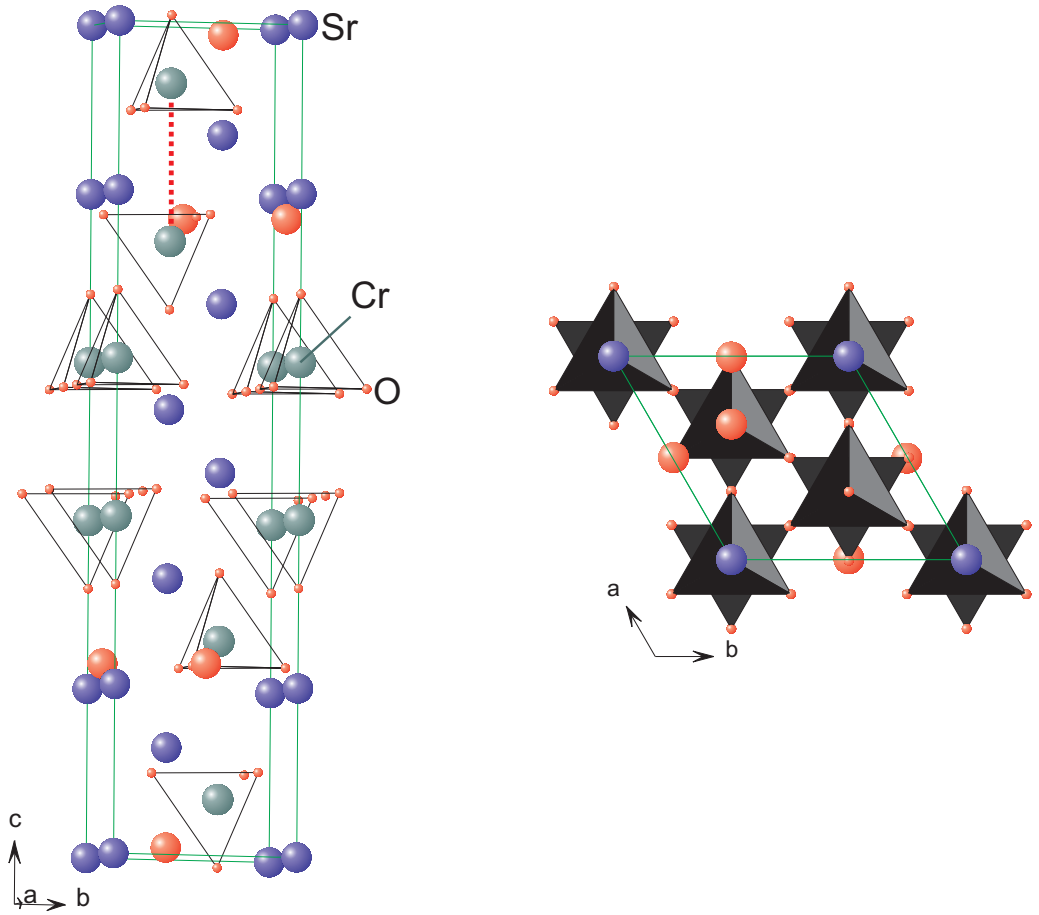

Figure 5.1: Crystal structure of $Sr_3Cr_2O_8$ along the crystallographic a axis (left) and c axis (right). The dotted red line marks the connection of two spins forming a dimer unit. The CrO_4 tetrahedra are denoted by closed faces in the right panel and black lines in the left panel.

Table 5.1: Symmetry analysis for $Sr_3Cr_2O_8$

Atom	Wyckoff position ($R\bar{3}m$)	allowed phonon modes	Wyckoff position ($C2/c$)	allowed phonon modes
Sr(1)	3a	–	4e	1 A_g + 2 B_g
Sr(2)	6c	1 A_{1g} + 1 E_g	8f	3 A_g + 3 B_g
Cr(1)	6c	1 A_{1g} + 1 E_g	8f	3 A_g + 3 B_g
O(1)	6c	1 A_{1g} + 1 E_g	8f	3 A_g + 3 B_g
O(2)	18h	2 A_{1g} + 3 E_g	8f	3 A_g + 3 B_g
O(3)	–	–	8f	3 A_g + 3 B_g
O(4)	–	–	8f	3 A_g + 3 B_g

Hence, for $T > T_S$ (i.e. for the $R\bar{3}m$ structure) the phonon spectrum consists of $\Gamma_{Raman} = 5 \cdot A_{1g} + 6 \cdot E_g$ Raman-active phonon modes, while at $T < T_S$ we expect $\Gamma_{Raman} = 19 \cdot A_g + 20 \cdot B_g$ modes. The corresponding Raman tensors are given by

$$A_{1g} = \begin{pmatrix} a & 0 & 0 \\ 0 & a & 0 \\ 0 & 0 & b \end{pmatrix}, E_{g,1} = \begin{pmatrix} c & 0 & 0 \\ 0 & -c & d \\ 0 & d & 0 \end{pmatrix}, E_{g,2} = \begin{pmatrix} 0 & -c & -d \\ -c & 0 & 0 \\ -d & 0 & 0 \end{pmatrix},$$
$$A_g = \begin{pmatrix} a & d & 0 \\ d & b & 0 \\ 0 & 0 & c \end{pmatrix}, B_g = \begin{pmatrix} 0 & 0 & e \\ 0 & 0 & f \\ e & f & 0 \end{pmatrix}.$$

To assign the phonon modes in $Sr_3Cr_2O_8$ to their respective symmetry, we performed light scattering experiments at room temperature (i.e. 295 K) and at 3 K with different light polarization configurations (zz, yy, and yz). Fig. 5.2 shows an overview of these spectra. Here, the laboratory z axis is parallel to the crystallographic c axis and therefore parallel to the direction of the Cr dimers. The y axis is perpendicular to the c axis and lies within the hexagonal ab plane. At room temperature only the A_{1g} phonon modes contribute to the zz polarization, while in crossed yz configuration, only E_g modes are allowed. The symmetry component yy contains both A_{1g} and E_g representations. In the structurally distorted, low temperature phase, the monoclinic ab plane is slightly canted from the hexagonal ab plane [42, 43]. Furthermore, three monoclinic twins exist below T_S that are obtained by rotating the unit cell by $\phi = \pm 60°$ within the ab plane. To take this into account, we introduce the angle ϕ to the Raman tensors A_g and B_g and obtain the following general expressions:

$$A_g = \begin{pmatrix} a\cos^2\phi - b\sin^2\phi & (a+b)\cos\phi\sin\phi & d\cos\phi \\ -(a+b)\cos\phi\sin\phi & b\cos^2\phi - a\sin^2\phi & -d\sin\phi \\ d\cos\phi & d\sin\phi & c \end{pmatrix},$$
$$B_g = \begin{pmatrix} 0 & e & f\sin\phi \\ e & 0 & f\cos\phi \\ -f\sin\phi & f\cos\phi & 0 \end{pmatrix}.$$

We find that the zz and yy polarizations lead to phonons with A_g symmetry, while the crossed polarization yz leads to A_g and B_g phonon modes. In the spectra of Fig. 5.2 taken at $T = 295$ K, we identify 10 of the expected 11 phonons. With decreasing temperatures, the spectra change drastically. At $T = 3$ K, we identify a total number of 26 out of the expected 39 phonon modes. Their corresponding mode frequencies and symmetry assignments are given in table 5.2. The discrepancy between the observed and expected modes in the low temperature phase can be due to a lack of phonon intensity of particular modes as well as to their overlap with larger intensity excitations.

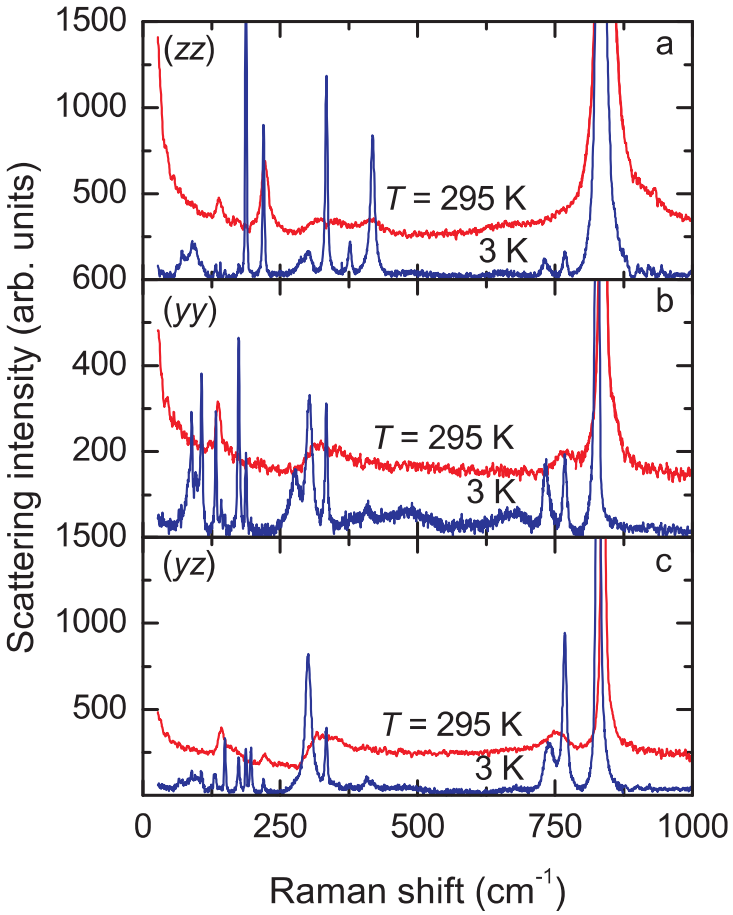

Figure 5.2: Comparison of the phonon spectrum of $Sr_3Cr_2O_8$ above and below T_S, obtained for different polarizations: a) zz, b) yy, and c) yz [41].

5.2 Electronic and magnetic properties

The Cr^{5+} ions in $Sr_3Cr_2O_8$ have a single $3d$ electron, leading to a $s = 1/2$ moment. At room temperature this electron resides in one of the two degenerate $d_{3z^2-r^2}$ and $d_{x^2-y^2}$ orbitals of the e level. At temperatures below $T_S = 275$ K, the degeneracy is lifted and the electron occupies the lower lying $d_{3z^2-r^2}$ orbital. Every unit of two nearest neighbor CrO_4 tetrahedra forms a dimer (with a Cr-Cr distance of 3.842 Å), as indicated in Fig. 5.1 by the dotted red line in the upper part. Assuming static orbital order, the low energy magnetism is described by Heisenberg exchange coupled $s = 1/2$ dimers of these pairwise arranged tetrahedra. The pairing into dimers leads to a gapped excitation spectrum.

The magnetic properties follow this scenario well: The magnetic susceptibility has a weak anisotropy, a maximum at $T_{max} = 38$ K and a rapid decrease towards lower temperatures suggesting gapped excitations [44]. In inelastic neutron scat-

Table 5.2: Phonon frequencies for $Sr_3Cr_2O_8$ in cm^{-1} with their respective symmetry assignments for the two structural phases $R\bar{3}m$ (at $T = 295$ K) and $C2/c$ (at 3 K).

$T = 295$ K, $R\bar{3}m$		$T = 3$ K, $C2/c$	
Phonon frequency [cm^{-1}]	Symmetry assignment	Phonon frequency [cm^{-1}]	Symmetry assignment
		71	A_g
		88	A_g
		106	A_g
		131	B_g
132	A_{1g} + E_g	133	A_g
		139	A_g
		149	B_g
		175	A_g
		188	A_g
		197	B_g
222	A_{1g}	220	A_g
		276	A_g
		288	A_g
300	E_g	302	B_g
330	E_g	334	A_g
		377	A_g
		407	B_g
415	A_{1g}	418	A_g
		732	A_g
750	E_g	740	B_g
765	A_{1g}	768	A_g + B_g
		824	B_g
840	A_{1g} + E_g	829	A_g + B_g
		835	A_g

tering experiments three gapped and dispersive magnetic excitation branches are observed with a spin gap of $\Delta = 3.5$ meV, a maximum energy $E_{max} = 7.0$ meV and a comparably large dispersion of ≈ 3.5 meV. A very satisfactory theoretical modeling is found for an intradimer exchange coupling constant of $J_0 = 5.55$ meV and comparably large interdimer couplings summing up to $J' \approx 3.58$ meV [44]. In ESR an excitation found at 1.250 Thz ($\widehat{=} 5.17$ meV) agrees well with that energy scale [45]. Its linewidth shows a strong broadening to higher temperatures due to a relaxation process involving the higher energy $d_{x^2-y^2}$ orbital state. The resolved orbital gap $\Delta_{orbital} = 388$ K is comparably small. In high magnetic

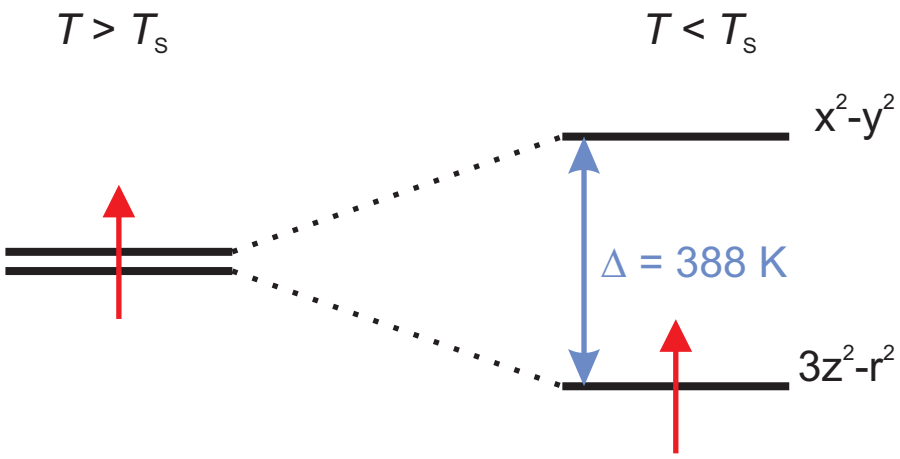

Figure 5.3: Orbital schematics in $Sr_3Cr_2O_8$ above and below T_S.

fields $Sr_3Cr_2O_8$ shows a Bose-Einstein condensation of diluted magnons. The magnetization increases with a threshold field at $H_{C1} = 30.4$ T and a saturation at $H_{C2} = 62$ T [46].

Summarizing the available experimental data, $Sr_3Cr_2O_8$ demonstrates a hierarchy of energy and temperature scales given by the orbital gap ($\Delta_{orbital} = 388$ K), the structural transition ($T_S = 275$ K), the magnetic exchange interaction ($J = 64$ K) and the spin gap ($\Delta = 40$ K). Most noteworthy is the small separation of thermal energy to $\Delta_{orbital}$ that still allows a considerable occupation of higher lying orbital states for $T < T_S$.

5.3 Cooperative Jahn-Teller distortion in $Sr_3Cr_2O_8$

At high temperatures, the electronic levels of the Cr e orbital are degenerate, i.e. both $3z^2 - r^2$ and $x^2 - y^2$ states are equally likely to be occupied. Energetically, this degeneracy is an unfavorable condition: *if the symmetry of the crystal field is so high that the ground state of an ion is [...] orbitally degenerate then it will be energetically preferable for the crystal to distort in such a way that the orbital degeneracy is lifted* [47]. Hence, towards low temperatures, a lifted orbital degeneracy through a distorted tetrahedral coordination is achieved, with the apical oxygen ions shifted from their initial position. This electronically driven structural instability, called Jahn-Teller distortion, leads to a lowering in crystal symmetry in $Sr_3Cr_2O_8$ below T_S.

5.4 Phonon anomalies

Figure 5.4 displays the temperature evolution of the low- and mid-frequency range of the Raman spectrum (from 25 to 350 cm^{-1}). In the intermediate temperature regime, we observe distinct changes in the phonon spectra, i.e., decreasing

phonon line width and intensity gain. In particular, the phonons at 188 and 334 cm^{-1} show a strong temperature dependence for temperatures $T < T_S$.

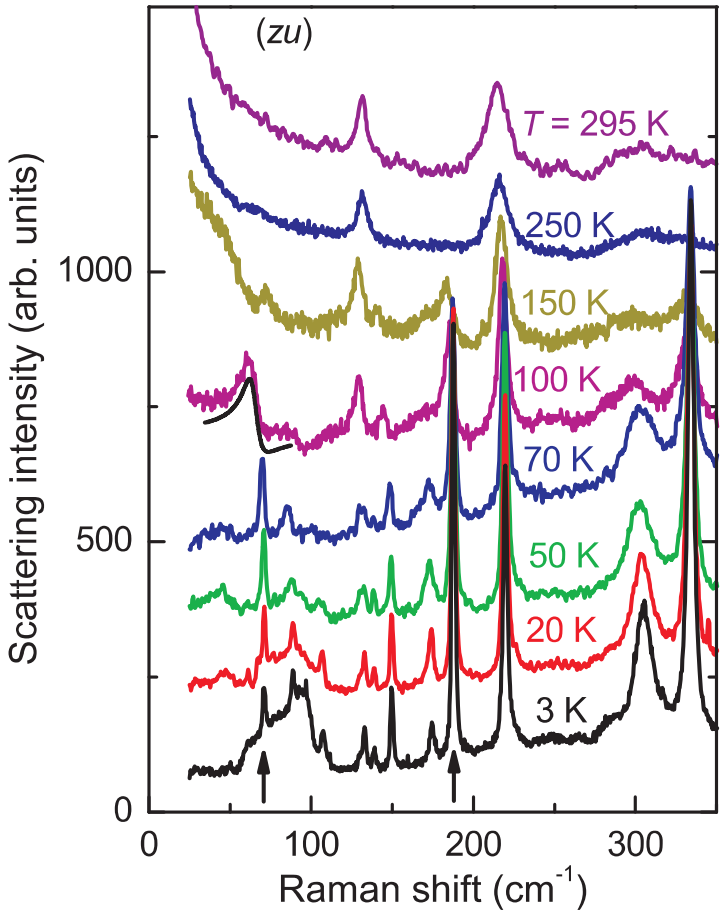

Figure 5.4: Temperature development of the low-frequency range (i.e. 25 – 350 cm^{-1}) from 3 to 295 K in zu polarization, i.e. without an analyzer. Spectra are shifted in intensity for clarity. The two arrows mark the phonons at 71 and 188 cm^{-1}. The black line below the 100 K data emphasizes the asymmetric line shape [41].

For a detailed analysis of the phonon dynamics, we plot the frequencies of important phonon modes in Fig. 5.5 a) as a function of temperature. For the group of phonons in the frequency range 125 – 150 cm^{-1} we observe two phonon splittings with decreasing temperature. The first one evolves very gradually, starting around T_S. The second, more pronounced one evolves at lower temperatures and marks a characteristic temperature $T^* \approx 150$ K. While the phonon at 188 cm^{-1} exhibits an energy shift by about 4% over the whole temperature range, the phonon at 71 cm^{-1}, which lies close in energy to two magnetic modes (as described below), shows an anomalous softening ($\approx 40\%$ between 3 and 150 K). Fitting this

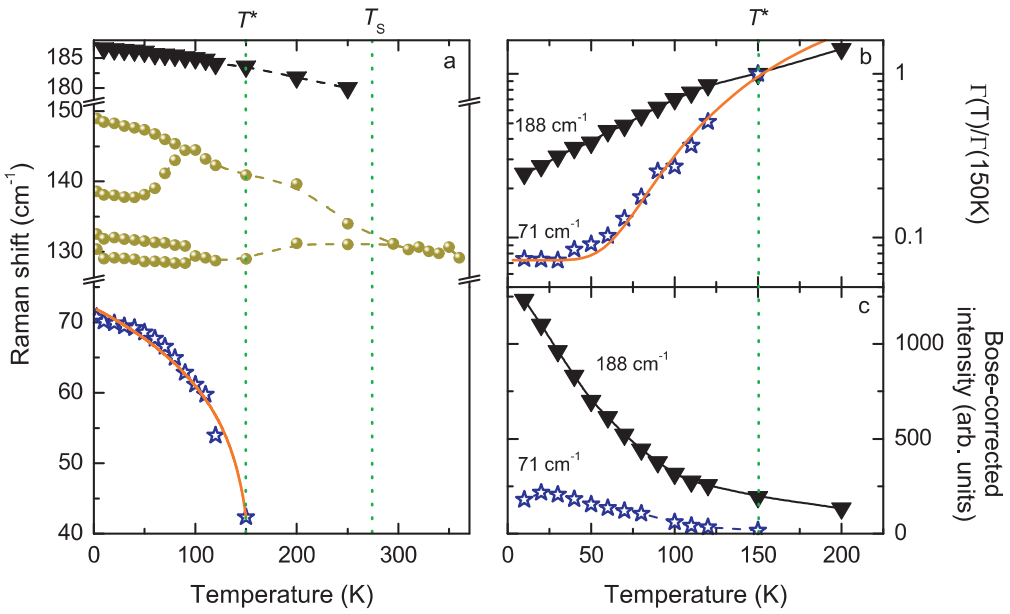

Figure 5.5: a) Temperature evolution of the phonon frequency at 71 (blue stars), 129, 132, 138 and 148 (yellow spheres), and 188 cm^{-1} (black triangles). The solid orange line is a fit to the 71 cm^{-1} data. b) Normalized line width $\Gamma(T)/\Gamma(150K)$ of the 188 and 71 cm^{-1} phonon modes. The solid orange line is a fit to the 71 cm^{-1} data. c) Bose-Einstein corrected phonon intensity at 188 and 71 cm^{-1}. The data of the 71 cm^{-1} mode has been scaled by a factor of 2; the 188 cm^{-1} data has been shifted by 250 arb. units for clarity. The green dashed lines in a), b), and c) indicate $T_S = 275$ K and $T^* \approx 150$ K [41].

energy to a power law, i.e., $\omega = A \cdot |T_C - T|^{\beta}$, leads to a good description in the regime below T^* with $A = 31.8$ cm^{-1}/K, $T_C = 156$ K, and $\beta = 1/6 \pm 0.016$. For a soft mode a critical exponent of $\beta = 1/2$ is expected from mean-field approximation. This is far from the fit to our data. It is noteworthy that T_C of this fit is inconsistent with T_S but comparable with T^*. This suggests that this critical behavior can be used as a second, independent way to determine the characteristic temperature T^*. For all phonon modes, the temperature dependence is reduced for temperatures below $T = 50$ K. One could describe this as a stabilization of the lattice.

In Fig. 5.5 b), the temperature dependence of the linewidth (full width at half maximum) for the phonons at 188 and 71 cm^{-1} is shown. The phonon at 71 cm^{-1} shows a dramatic decrease in linewidth by a factor of 11 between 150 and 3 K. At the same time, there is a change in lineshape from an asymmetric Fano line to a symmetric Lorentzian. This is indicated by the black solid line fitted to the 100 K spectrum in Fig. 5.4. In contrast, the line at 188 cm^{-1} shows only a moderate decrease in linewidth with a slight change in slope at T^*. We find that an activated function $\Gamma = B + C \cdot e^{-\Delta_{JT}/k_B T}$, with $B = 0.09$ cm^{-1}, $C = 18.1$ cm^{-1}, and

$\Delta_{JT}/k_B = (450 \pm 20)$ K provides a very reasonable description to the temperature dependence of the 71 cm^{-1} phonon linewidth. The characteristic energy Δ_{JT} is very similar to the orbital gap $\Delta_{orbital} = 388$ K that has been used to describe previous ESR data [45]. Here, the ESR absorption line increases exponentially with increasing temperature due to an Orbach spin relaxation process. In Fig. 5.5 c), the phonon intensity is plotted as a function of temperature for the two lines at 188 and 71 cm^{-1}. The intensity of the 188 cm^{-1} mode displays a strong increase for temperatures below T^* without saturation. On the other hand, the intensity of the phonon at 71 cm^{-1} increases gradually and reaches its maximum at $T \approx 25$ K.

It is important to note that we did not observe any sudden changes of the Raman phonon spectra between 295 K and 250 K, see Fig. 5.4. This means that the coherent part of lattice distortions develops only at lower temperatures. In contrast, the quasi-elastic scattering, a probe of fluctuations with similar evolution as the specific heat, discontinuously sets in for $T = T_S$. We therefore conclude an extended orbital fluctuation regime from T_S down to approximately $T^* = 150$ K. For $T < T^*$ the phonon modes show a gradual increase of intensity and a rapid increase below approximately 110 K. Additionally, below 110 K distinct phonon splittings show up and the quasi-elastic scattering is suppressed. Therefore T^* marks a crossover with a suppression of orbital fluctuations and an onset of long range structural distortions.

We carefully inspected whether collective orbital excitations (orbitons) show up in the frequency range of $\Delta_{JT} \approx 270$ – 330 cm^{-1}. At room temperature we observe a highly-damped peak in the respective energy interval (see Fig. 5.6). With lowering temperature two modes develop at about 300 and 330 cm^{-1}. In contrast to other sharp peaks at 3 K, the phonon mode at 300 cm^{-1} ($\widehat{=}$ 430 K) is relatively broad. This indicates the possibility that the corresponding mode is an orbital excitation mixed with a phonon. Further evidence for mixing of phonon and orbital degrees of freedom is gained from the temperature dependence of the 71 cm^{-1} phonon mode, in energy, linewidth and lineshape. Actually, the evolution of the linewidth with the temperature strongly resembles that of a crystalline electric field transition found in the rare earth compound Pr_2CuO_4 [48]. However, in a $3d$ electron system such modes should be broadened by dispersion. In band structure calculations [49] for $Sr_3Cr_2O_8$ the respective energy scale is of the order of 300 meV, i.e. also one order larger than Δ_{JT}. Therefore, the origin of the 71 cm^{-1} mode is very likely a mixed phonon-orbiton mode. Related displacements could be rotational motions of the CrO_4 tetrahedra. Such displacements simultaneously modify all Cr-O bond lengths and therefore couple to the $d_{3z^2-r^2}$ orbitals.

5.5 Quasi-elastic scattering

Upon approaching T_S, a broad, quasi-elastic ($E \approx 0$) scattering contribution with Lorentzian lineshape and A_{1g} symmetry increases in intensity and decreases

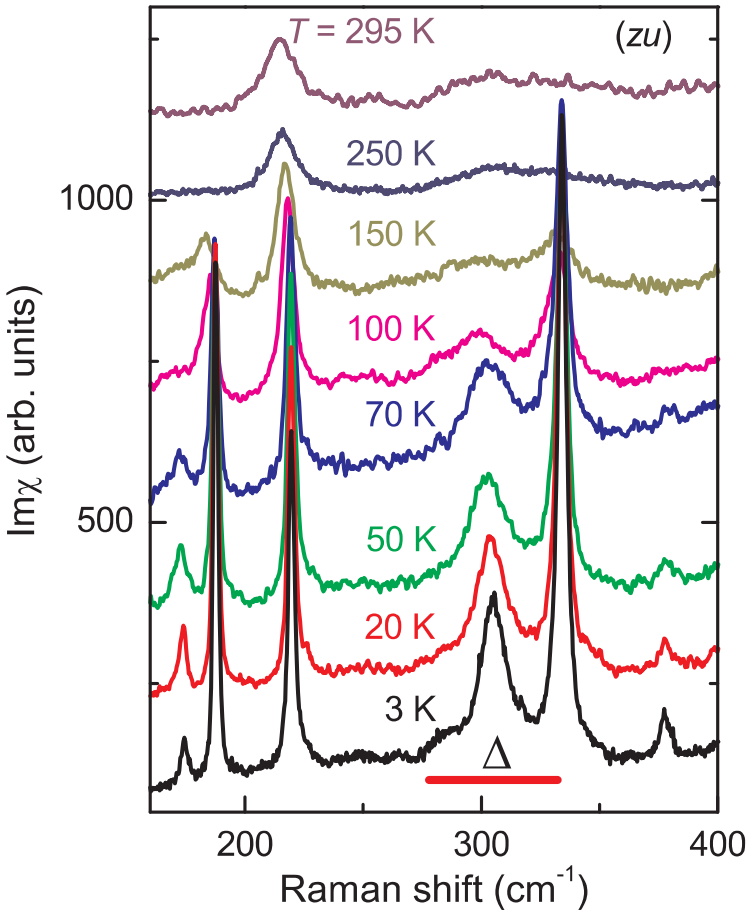

Figure 5.6: Temperature development of the mid-frequency range (i.e. 250 – 400 cm^{-1}) from 3 to 295 K in zu polarization, i.e. without an analyzer, and without Bose-Einstein correction; spectra are shifted in intensity for clarity. The red bar marks the energy scale of the orbital gap Δ around 300 cm^{-1}.

again continuously for temperatures below approximately 200 K; see Fig. 5.4 and 5.7 for its intensity. The data clearly reveal pronounced fluctuations and can be deconvoluted into two contributions: a sharp onset at T_S and a broad maximum at lower temperatures with a softer leveling off below T^*, as indicated by the solid blue lines. This behavior is in stark contrast to the evolution of the phonon intensity. One could compare this contribution to a so-called central mode, induced by fluctuations at a structural phase transition [50]. However, in this case, for temperatures below T_S the fluctuations should be suppressed and no second maximum is expected. Therefore structural fluctuations are unlikely to be the origin for this scattering contribution. Further candidates are orbital or spin fluctuations. Such fluctuations as energy density fluctuations should scale with a corresponding contribution to the specific heat [4]. Indeed, also the resid-

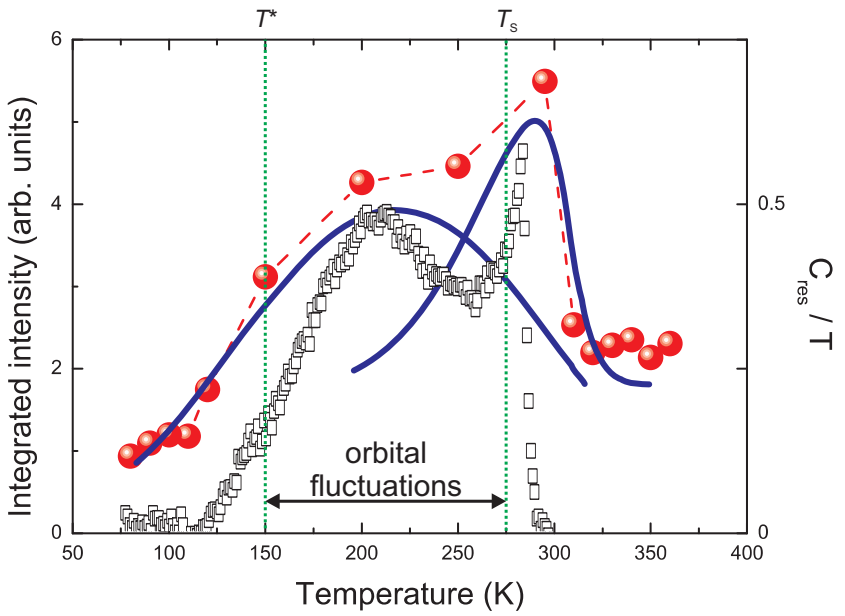

Figure 5.7: Integrated intensity of the quasi-elastic signal over temperature (red spheres). The solid blue lines represent the two contributions from orbital fluctuations and the structural transition. The open squares are derived from specific heat measurements [45].

ual specific heat (i.e. with lattice and magnetic contributions subtracted) shows a second, broader maximum at $T = 200$ K [45], as displayed by the empty boxes in Fig. 5.7.

5.6 2- and 3-magnon scattering

Figures 5.8 a) – c) zoom into the low-energy part of the Raman spectra. Two modes are observed at around 45 and 90 cm^{-1} with a larger linewidth compared to the previously discussed phonon modes. While the 90 cm^{-1} mode is most prominent at lowest temperature, the one at 45 cm^{-1} exhibits a finite intensity only in the temperature interval 10 K $< T <$ 75 K. To confirm that these modes are of intrinsic nature, we probe the sample with different laser wavelengths and compare the spectra. The result is shown in Figs. 5.8 a) and b). Fits to the two modes are shown by a highlighted area below the $\lambda = 532$ nm spectrum in Fig. 5.8 a). In Fig. 5.8 c), different polarizations at $T = 3$ K are probed with the $\lambda = 488$ nm excitation wavelength. Finally, the temperature dependence of the Bose-Einstein corrected broad modes' integrated intensities is plotted in Fig. 5.8 d). While the 90 cm^{-1} mode increases steadily with decreasing temperature, the 45 cm^{-1} mode clearly shows a maximum in intensity at around 30 K, before further decreasing and finally vanishing at lowest temperature. The intensity decrease

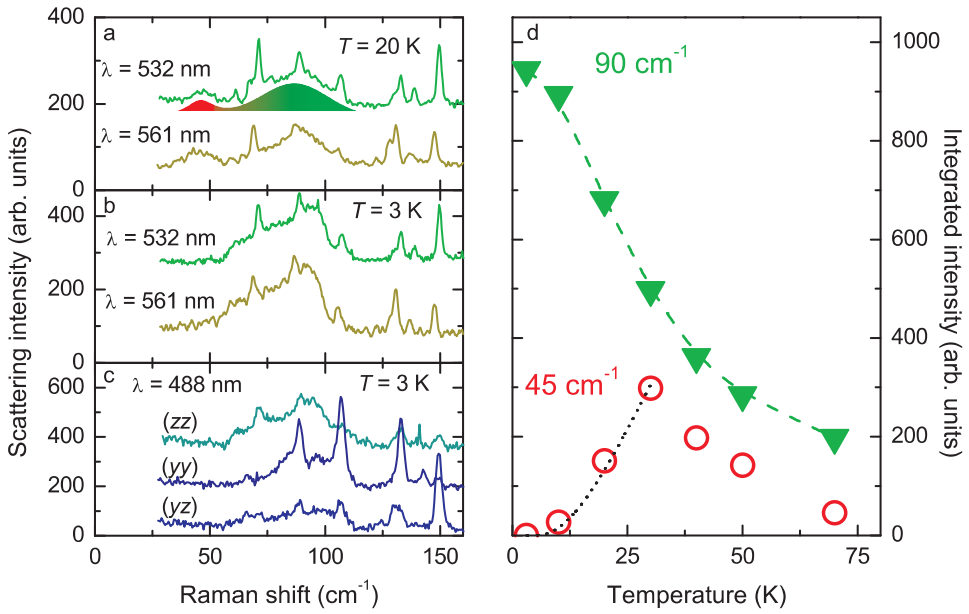

Figure 5.8: a) and b) Low-energy range of Raman spectra (ranging from 25 to 165 cm^{-1}) taken at $T = 20$ K a) and $T = 3$ K b) with the excitation wavelengths $\lambda = 532$ nm and $\lambda = 561$ nm in zu polarization. The filled area under the spectrum in a) are fits to the modes at 45 and 90 cm^{-1}. c) Low-energy spectral range in different polarizations obtained at $T = 3$ K with the $\lambda = 488$ nm laser line. d) Bose-Einstein corrected integrated intensity of the 45 and 90 cm^{-1} modes. The black dotted line corresponds to a fit to the Bose-Einstein statistics of an excited level with $\Delta = 40$ K [41].

fits well to a Bose-Einstein factor of an excited level as shown by the dotted line, $n_i \sim 1/[e^{(E_i-\Delta)/T} - 1]$ with $\Delta = 40$ K ($\widehat{=}$ 28 cm^{-1}). This is in excellent agreement with the spin gap value reported by neutron scattering [44].

In Fig. 5.8 a), two magnetic modes are observed at low but finite temperatures. The high-energy magnetic mode at 90 cm^{-1} is observed in all measured polarizations, i.e., zu, zz, yy, and yz, but has its strongest contribution in zz and zu polarization, i.e., the polarization along the dimer direction. In crossed (yz) polarization its intensity is weakest. Since the magnetic Raman scattering intensity is given by $I \propto |\langle i| \sum_{i,j} \vec{S}_i \cdot \vec{S}_j |j\rangle|^2$, it scales in each polarization with the strength of exchange interactions between dimers. In this sense, the presence of the substantial spectral weight in the yy polarization implies moderate interdimer interactions in the ab plane. The onset energy of the magnetic excitations is roughly 56 cm^{-1}, which corresponds to 7 meV or 81 K and is therefore twice the size of the spin gap. The high-energy cut-off at 118 cm^{-1} corresponds to 14.75 meV. As the triplet branch of excitations observed in inelastic neutron spectroscopy reaches up to 7.2 meV, we attribute this mode to two-magnon scattering, i.e., a scatter-

ing process involving the simultaneous spin flip of two neighboring spins, hence costing twice the magnetic exchange energy. The intensity of the two-magnon mode is plotted over temperature in Fig.5.8 d) (green triangles). It continuously decreases in intensity as the temperature is increased and fully depletes below 100 K. This is associated with a thermal population of the singlet ground state into an excited triplet state.

The intensity of the mode at 45 cm^{-1}, on the other hand, shows a clear maximum at around 30 K before steadily decreasing toward ≈ 80 K. Therefore, we can rule out one-magnon scattering, which would show a monotonous increase in intensity down to lowest temperature. Instead, a three-magnon scattering process might account for this observed mode [51]. Three-magnon scattering can occur through a transition from one singlet and one excited triplet state to two neighboring triplet states, i.e., $(|\uparrow\downarrow\rangle - |\downarrow\uparrow\rangle) \otimes (|\uparrow\downarrow\rangle + |\downarrow\uparrow\rangle) \rightarrow |\uparrow\uparrow\rangle \otimes |\downarrow\downarrow\rangle$. Therefore, it can only arise in the environment of thermally excited triplet states at finite temperatures. Such a thermal population is described by the Bose-Einstein statistics of the excited level. Our data is in good agreement with theory, as the fit to the integrated intensity at low temperatures in Fig. 5.8 d) shows. Upon additional temperature increase, one furthermore increases the population of triplets, which eventually leads to saturation. This causes the intensity of the three-magnon mode to drop again toward high temperatures. The onset of the mode is at roughly 30 cm^{-1}. As a three-magnon process corresponds to a transition from the triplet branch at the Γ-point of the Brillouin zone to the two-magnon band, the onset energy can be estimated by $E_{2M,onset} - \Delta \approx \Delta = 28$ cm^{-1}, which fits well to the observed value. The cut-off energy would therefore be expected around $E_{2M,cutoff} - \Delta \approx 90$ cm^{-1}. However, it can only unambiguously be traced up to 56 cm^{-1}, i.e., the onset of the two-magnon signal. Above this energy the two modes overlap, therefore a clear determination of the cut-off energy is rather difficult.

We can now compare our observations to related systems: The extended fluctuations observed in $Sr_3Cr_2O_8$ are different from those observed in quasi-one-dimensional correlated electronic systems like $BaVS_3$ [52] or weakly doped manganites, where persisting orbital fluctuations are attributed to an entangled instability of the orbital, electronic, and lattice subsystems [53]. Since $Sr_3Cr_2O_8$ has no electronic instability or low dimensionality, the origin of the fluctuations should be sought in the relation between the orbital ordering and the structural instability. Introducing a ratio of the Jahn-Teller gap versus the structural phase transition temperature, $\Delta_{JT}/T_S = 1.4$ – 1.6, shows that thermal fluctuations even well below T_S can smear out the Jahn-Teller gap and thus destabilize orbital ordering. A similar observation of a mixed excitation was reported for the vanadates RVO_3, where orbital excitations couple to the Jahn-Teller phonon [54]. This phenomenology is different from observations of "pure orbitons" in the three dimensional perovskites $LaTiO_3$ and $YTiO_3$ as in these compounds the energy scale of the orbital excitations (2700 K) is clearly separated from the phonon system and does not overlap with other excitations, either [55]. Considering the observed mag-

netic excitations, a three-magnon scattering process has also been reported in the weakly coupled spin dimer compound $KCuCl_3$ with a spin gap of $\Delta = 31$ K [56] and in the Spin-Peierls system $CuGeO_3$ with $\Delta = 23$ K [51]. All three compounds show a maximum in scattering intensity around the spin gap temperature. However, for $KCuCl_3$, the three-magnon signal is observed up to $T \approx 5 \cdot \Delta$, while for $Sr_3Cr_2O_8$ it is obscured by the lattice fluctuations even at $T \approx 2 \cdot \Delta$. All three systems show an instability in large magnetic fields. For $KCuCl_3$ and $Sr_3Cr_2O_8$ this is a Bose-Einstein condensation of diluted magnons, while $CuGeO_3$ becomes an incommensurate antiferromagnet. The common observation of three-magnon Raman scattering and a field-induced transition is due to enhanced hopping, i.e., a not too large gap compared to the available magnetic fields.

5.7 Comparison with $Ba_3Cr_2O_8$

The sister compound $Ba_3Cr_2O_8$ crystallizes in the same $R\bar{3}m$ structure as $Sr_3Cr_2O_8$, with Ba ions replacing Sr and all atoms residing at the same Wyckoff positions as in $Sr_3Cr_2O_8$. Due to the larger ionic radius of Ba compared to Sr, the volume of the unit cell is increased by 12.8% and the Cr-Cr distance is 3.9765 Å(corresponding to a 3.5% increase). In comparison, the energies of $Ba_3Cr_2O_8$ are scaled down, with $J_0 = 2.38$ meV, $H_{C1} = 12$ T, $H_{C2} = 23$ T, and $T_{JT} = 70$ K [57]. The ratio of inter- to intradimer interaction was found to be $J'/J_0 = 0.8151$ [44, 57], which is slightly larger than the ratio in $Sr_3Cr_2O_8$ (with $J'/J_0 = 0.64$ [44]). Below T_{JT} the crystal structure transitions from hexagonal $R\bar{3}m$ to monoclinic $C2/c$, similar to $Sr_3Cr_2O_8$. Single crystals were grown in the labs of Y. Ueda at ISSP Tokyo and oriented via Laue X-ray diffraction by Dirk Menzel. To obtain an optically flat surface, the sample was polished mechanically using diamond polishing paste.

In Fig. 5.9 we show Raman spectra of $Ba_3Cr_2O_8$ at 295 K (red curves) and at 3 K (blue curves) with different light polarizations. Again, the laboratory z axis is parallel to the crystallographic c axis and thereby parallel to the spin dimers. The y axis is perpendicular to the c axis and lies within the ab plane. At high temperatures a phonon spectrum comparable to $Sr_3Cr_2O_8$ is observed, with 10 out of 11 expected phonon modes. However, with decreasing temperature, the changes are far less dramatic than in the sister compound $Sr_3Cr_2O_8$ (cf. Fig. 5.2) and down to 3 K the number of phonon modes remains comparable to the high temperature phase. A subsequent infrared spectroscopy study found a clear change in the spectra at T_{JT}, which lead to the conclusion that no extended fluctuation regime is present in $Ba_3Cr_2O_8$ [58].

In crossed yz polarization and at $T = 3$ K a broad scattering contribution ranging from 400 – 650 cm^{-1} is observed, marked by the black arrow in Fig. 5.9 c). It is tempting to assign this signal to Raman scattering on orbital excitations, as reported in $LaTiO_3$ and $YTiO_3$ [55]. In contrast to $Sr_3Cr_2O_8$, the spectral range of this signal is not populated with other (phonon) excitations. On the other hand,

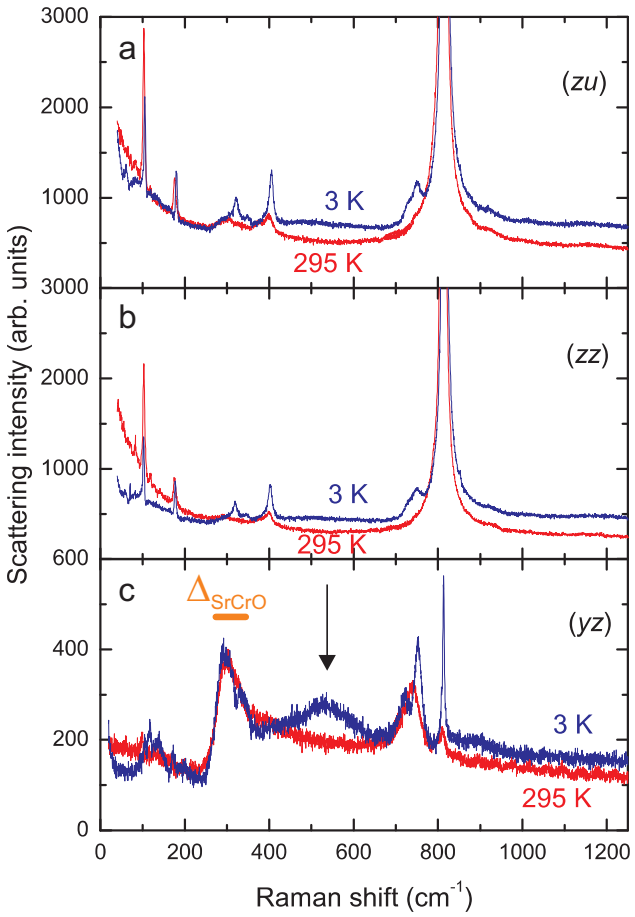

Figure 5.9: Comparison of the phonon spectrum of $Ba_3Cr_2O_8$ at 295 K (red lines) and 3 K (blue lines), obtained for different polarizations: a) zu, b) zz, and c) yz. The orange bar in c) marks the energy scale of the orbital gap Δ around 300 cm^{-1} for $Sr_3Cr_2O_8$.

the reduced energy scales in $Ba_3Cr_2O_8$ will lower the size of the orbital gap. For comparison, we indicate the energy range of the orbital gap in $Sr_3Cr_2O_8$ by an orange bar. Therefore, a possible scattering contribution due to orbital excitation could be rather expected around $\approx$ 100 cm^{-1}. In this regime several phonons are located together with quasi-elastic scattering in the other polarizations. Furthermore, imperfections of the sample (surface), as reported in infrared experiments [58], might lead to unexpected scattering contributions. We therefore assign the additional spectral weight at 400 – 650 cm^{-1} to phonon density of states related to disorder.

5.8 Conclusion

Our Raman data presented in this chapter reveal an extended regime of strong orbital fluctuations in the spin dimer system $Sr_3Cr_2O_8$ that couple to the lattice degrees of freedom. This is evidenced for one by an unusually wide temperature regime over which the crystal symmetry is reduced from hexagonal $R\bar{3}m$ to monoclinic $C2/c$. Phonon anomalies due to coupling between lattice and spins include a soft mode arising below $T^* = 150$ K with a critical broadening, related to orbital ordering. This allows us to estimate the orbital gap $\Delta_{JT} = 450$ K. The observed quasi-elastic scattering as function of temperature further evidences strong orbital fluctuations and compares very well with the residual specific heat. As the quasi-elastic signal is related to the two characteristic temperatures, it can be used as an independent probe for T_S and T^*. From the 2- and 3-magnon Raman scattering signals we derive the size of the spin gap $\Delta = 40$ K.

In contrast to $Sr_3Cr_2O_8$ the isostructural sister compound shows no sign of orbital fluctuations. On the one hand, $Ba_3Cr_2O_8$ shows the same hierarchy of energies, with all quantities scaled down in energy. On the other hand, the ratios of the interacting quantities are different, with slightly more dominating interdimer interactions in $Ba_3Cr_2O_8$. This could stabilize a 3D dimer network below T_S and suppress any lattice and orbital fluctuations. The comparison of these two seemingly similar compounds demonstrates impressively how minor details can strongly modify the physics of correlated electron systems.

Chapter 6

Raman scattering in kagome lattices

The study of the kagome lattice as a promising candidate for a spin liquid in 2D has attracted a great deal of interest over the years. For a long time, however, the lack of appropriate materials has confined the study to theoretical calculations. Recently, it was found that herbertsmithite ($ZnCu_3(OH)_6Cl_2$) realizes a structurally perfect $s = 1/2$ kagome lattice. From this point of view, herbertsmithite with its corner-sharing triangles is a paradigm of a highly frustrated spin system, with low dimensionality (2D), low coordination number ($z = 4$) and small spin quantum number s. This compound is available as a natural grown mineral as well as synthesized single crystals. In this chapter, Raman scattering experiments on both mineral and synthesized herbertsmithite are presented and discussed [59]. Furthermore, a comparison with the slightly distorted kagome systems vesignieite and volborthite will be made [60].

6.1 Crystal structure of herbertsmithite

Single crystal samples of herbertsmithite from two different sources were available to investigate the magnetic and electronic properties: Natural crystallites obtained from a copper mine in Chile, with typical dimensions of $0.5 \times 0.5 \times 0.5$ mm, and a single crystal grown via hydrothermal synthesis in the labs of Young S. Lee, MIT, with a dimension of about $1 \times 0.2 \times 0.2$ mm [61]. The color of the samples is dark green and they are semi transparent. Furthermore, a study of the structural properties has been carried out on a set of powder samples with the stoichiometry $Zn_xCu_{4-x}(OH)_6Cl_2$ and $0.5 \leqslant x \leqslant 1.4$, together with a deuterated powder sample of herbertsmithite, i.e. $ZnCu_3(OD)_6Cl_2$.

Herbertsmithite crystallizes in the rhombohedral space group $R\bar{3}m$ with the lattice constants $a = b = 6.83$ Å, $c = 14.03$ Å, and $\gamma = 120°$. It is the $x = 1$ end member of the zinc paratacamite family $Zn_xCu_{4-x}(OH)_6Cl_2$, with $0 \leqslant x \leqslant 1$. The Cu^{2+} ions ($s = 1/2$) are located on the intersection points of a two dimensional

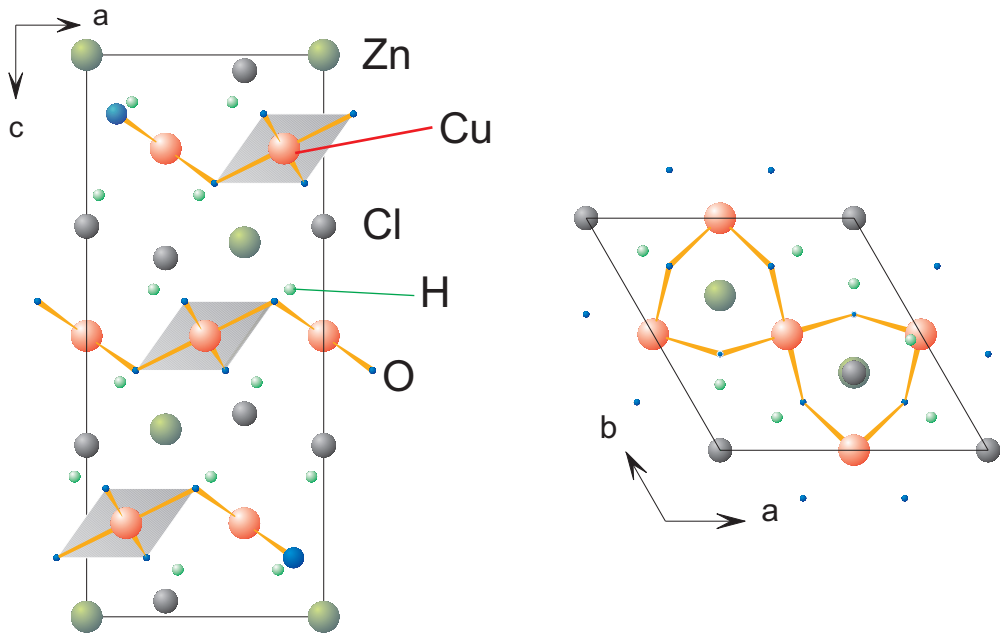

Figure 6.1: Crystal structure of herbertsmithite – left figure: projection along the b axis, right figure: projection along the c axis.

kagome lattice within the ab plane and coupled via O-H groups. The kagome planes are separated by non-magnetic layers of Cl and Zn ions and stacked along the c axis, as shown in the left panel of Fig. 6.1.

6.2 Electronic and magnetic properties

The Cu^{2+} ions ($3d^9$, $s = 1/2$) forming the kagome lattice are magnetically coupled by super-exchange via O-H groups. Susceptibility measurements yield a Curie-Weiss temperature of $\Theta_{CW} = -300$ K. The antiferromagnetic exchange interaction has a value of about $J = 180$ K ($\widehat{=}$ 125 cm^{-1}). Despite this strong coupling, magnetic susceptibility measurements reveal no magnetic ordering down to 50 mK [62]. Thus, the level of frustration with $f = |\Theta_{CW}/T_N| > 6000$ is immense. The planes of these kagome structures are separated by intermediate layers of Zn and Cl atoms and can therefore ideally be considered as two-dimensional layers with negligible magnetic interactions along the third dimension. However, Zn/Cu antisite disorder of about 6% [63] is believed to be present in previously studied herbertsmithite samples. Hence, the presence of a small number of impurities may affect the spin correlations in the kagome plane.

Muon spin rotation (μSR) measurements on the paratacamite $Zn_{0.5}Cu_{3.5}(OH)_6Cl_2$ show a partly frozen ground state [64], which however disappears for higher Zn/Cu ratios. Electron spin resonance measurements on herbertsmithite reveal DM interactions of about $D = 0.08 \cdot J$ magnitude [65],

Table 6.1: Symmetry analysis for herbertsmithite

Atom	Wyckoff position	allowed phonon modes
Zn	3a	–
Cu	9d	–
O	18h	2 A_{1g} + 3 E_g
H (D)	18h	2 A_{1g} + 3 E_g
Cl	6c	1 A_{1g} + 1 E_g

which, together with the antisite disorder, causes a ferromagnetic-like increase of susceptibility at low temperature. These and other experiments have been performed either on natural (mineral) crystals or powder samples [66].

6.3 Phonon modes in herbertsmithite

In table 6.1 the Wyckoff position for each atom is listed together with the respective Raman active modes [27].

This yields a total of $\Gamma_{Raman} = 5 \cdot A_{1g} + 7 \cdot E_g = 12$ Raman active phonon modes. Furthermore, magnetic Raman scattering of A_{2g} symmetry is allowed in this compound, as discussed later on. The corresponding Raman tensors are given by

$$A_{1g} = \begin{pmatrix} a & 0 & 0 \\ 0 & a & 0 \\ 0 & 0 & b \end{pmatrix}, A_{2g} = \begin{pmatrix} 0 & e & 0 \\ -e & 0 & 0 \\ 0 & 0 & 0 \end{pmatrix}, \text{and } E_g = \begin{pmatrix} c & 0 & 0 \\ 0 & -c & d \\ 0 & d & 0 \end{pmatrix}.$$

Fig. 6.2 shows an overview of the 12 phonon modes. 7 modes appear in the energy range below 1000 cm^{-1}, while 5 modes are situated at higher energies around 3400 cm^{-1}. They are attributed to hydrogen displacements. To differentiate between A_{1g} and E_g modes, a polarization dependent study of the phonon modes within the crystallographic ab plane was conducted. While E_g modes appear in both xx and yx polarization (i.e. parallel and crossed polarization), A_{1g} modes only contribute to spectra obtained in xx polarization. In addition, by rotating the samples within the ab plane (corresponding to the $x - y$ plane in the laboratory frame of reference) the A_{1g} modes are expected to give a rotation invariant contribution in xx polarization and disappear in yx polarization. The E_g modes should show a fourfold symmetry in both polarizations. Due to the semi-transparent character of the samples the light polarization and thereby the symmetry components will be partially scrambled. In addition, the anisotropic electronic polarizability related to the layered structure will cause slight misalignments of the crystal to show up as an additional twofold modulation of the scattering intensity. The assignments of the phonon modes are given in Fig. 6.2.

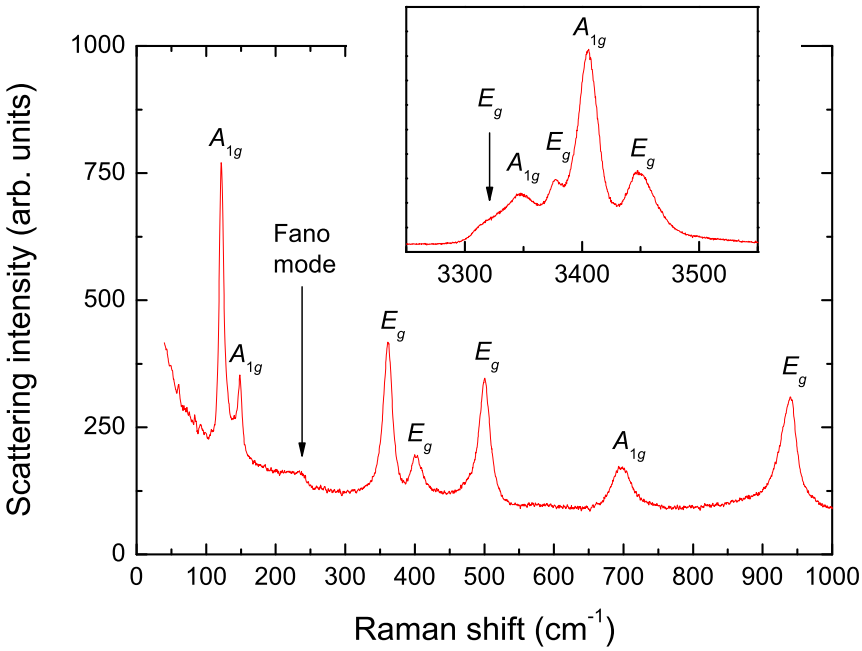

Figure 6.2: Phonon modes in $ZnCu_3(OH)_6Cl_2$. Main panel: 0 – 1000 cm^{-1} range, inset: the 5 high frequency H modes around 3400 cm^{-1}.

To confirm the origin of the high energy modes, a second sample with hydrogen substituted by deuterium was measured. In a simplified harmonic oscillator picture, the phonon frequency is given by $\omega \sim \sqrt{\frac{k}{m}}$, where m is the mass of the involved atom and k is the spring constant. Upon exchanging hydrogen atoms with deuterium, the atomic mass is doubled and therefore all hydrogen-assigned modes are expected to shift by a factor of $\sqrt{m_H/m_D} = \sqrt{1/2} \sim 0.71$. Indeed, we observe a renormalization of all 5 high frequency phonon modes by a factor of about 0.74 with substitution, while the other, low frequency modes, remain unaffected [59].

The phonon mode around 700 cm^{-1} can be used as a measure for the stoichiometry. Upon changing the Zn-Cu ratio in $Zn_xCu_{4-x}(OH)_6Cl_2$ within the range of $0.5 \leqslant x \leqslant 1.2$ this phonon shifts linearly in energy (see Fig. 6.3). With this relation, which is approximated by $E_{\text{phonon}} = 725.7\text{cm}^{-1} - 30.2\text{cm}^{-1} \cdot x$, we can determine the stoichiometry of single crystalline samples. Comparing both mineral and synthesized crystals to the powder sample data, we obtain for the latter sample a stoichiometry of $Zn_1Cu_3(OH)_6Cl_2$, while the mineral crystal yields $Zn_{0.8}Cu_{3.2}(OH)_6Cl_2$. Therefore, the synthesized single crystal is in the regime of

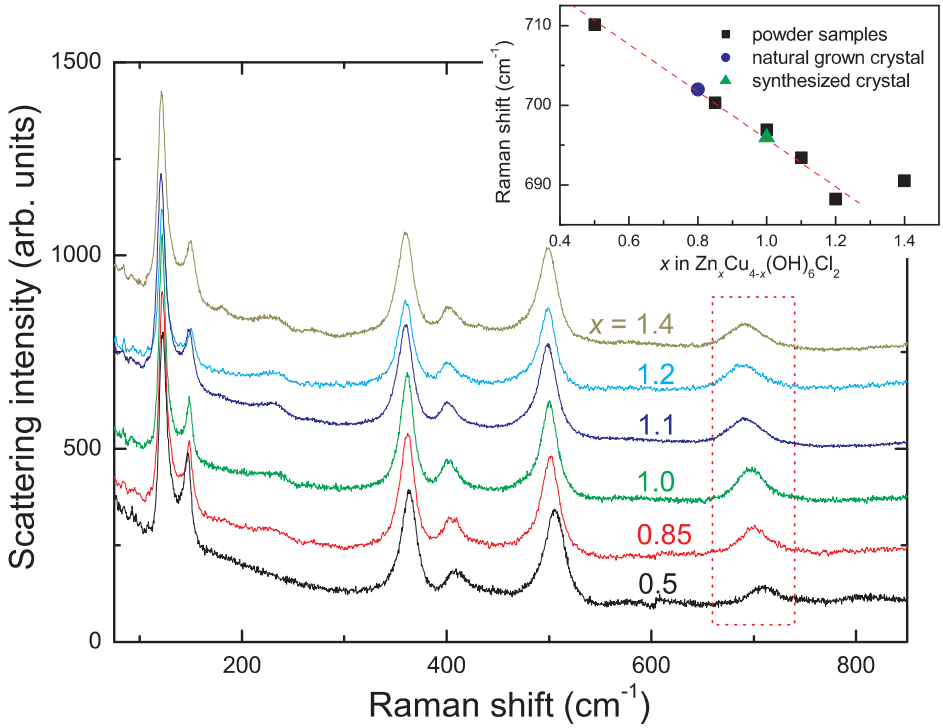

Figure 6.3: Raman spectra for $Zn_xCu_{4-x}(OH)_6Cl_2$ with x = 0.5, 0.85, 1.0, 1.1, 1.2, and 1.4. The spectra are shifted in intensity for clarity. The inset shows the linear frequency dependence of the phonon mode at 700 cm^{-1} with the Cu/Zn ratio [67].

herbertsmithite stoichiometry. Yet, the mineral single crystal is still reasonably close to this regime in the sense that thermodynamic and spectroscopic experiments did not observe any long range ordering for $x = 0.8$ [64]. Comparing the two different samples should therefore allow determining the influence of spin defects on the spin dynamics.

6.4 Quasi-elastic scattering in herbertsmithite

To gain information about the temperature evolution of spin correlations, we analyze the quasi-elastic scattering in both mineral and synthesized herbertsmithite single crystal samples. Fig. 6.4 a) zooms into the quasi-elastic tail obtained in mineral herbertsmithite crystallites at room temperature (i.e. 295 K) and in xx polarization. The phonon modes in the displayed low-energy range have been subtracted for clarity. To check for the origin of this signal (i.e. spin diffusion [7] or energy fluctuations [6]), a gaussian and a lorentzian fit are applied to the data. It can be clearly seen that the lorentzian curve describes the data very well, while

the gaussian diverges from the data at low energies. The observation of QES is a very general feature of low dimensional spin systems, such as spin chains [68] or frustrated dimer systems [69]. Here, energy density fluctuations can couple via spin-phonon coupling to the lattice. Its symmetry should be of A_{1g} symmetry [5]. The rotational invariance shown in the inset of Fig. 6.4 is distorted with two-fold symmetry but within experimental error identical to the one of the phonon modes identified as belonging to the A_{1g} symmetry representation.

The temperature development of the QES is displayed in Fig. 6.4 b). Its intensity can be mapped onto the specific heat C_m of the spin system, $I(\omega \rightarrow 0, T) \sim C_m\ T^2$. With decreasing temperatures a decrease in intensity is observed, which can be best fitted by a power law. The observed exponent varies from $I(\omega \rightarrow 0, T) \sim T^{(1.49\pm0.21)}$ to $I(\omega \rightarrow 0, T) \sim T^{(4.95\pm0.24)}$ for the synthesized and the mineral sample, respectively. From this temperature dependence $I(\omega \rightarrow 0, T)$ we can derive information on the evolution of low energy excitations. In, e.g., the Shastry-Sutherland compound $SrCu_2(BO_3)_2$ the exponential drop of the respective intensity has been used to derive a spin gap [69]. The power law-like temperature dependence in $ZnCu_3(OH)_6Cl_2$ differs clearly from that and implies a spin liquid with more gradually evolving correlations [70]. In the synthesized crystal the power law is much softer, with $I(\omega \rightarrow 0, T) \sim T^{3/2}$. We attribute this fact to the reduced number of defects leading to a much more gradual evolution of spin correlations.

6.5 Spinon continuum in herbertsmithite

At temperatures below ~ 50 K a broad maximum at finite energy is observed in Raman spectra for both the mineral as well as the synthesized single crystal. This is depicted in Fig. 6.5 b) and c). For the synthesized sample the maximum position is slightly higher ($E_{max} = 265$ cm$^{-1} \approx 2.1J$) compared to the mineral one (215 cm$^{-1} \approx 1.7J$). In addition, the synthesized sample also shows a more pronounced decrease of scattering intensity towards higher energies. We attribute the broad continuum in both samples of $ZnCu_3(OH)_6Cl_2$ to scattering on magnetic correlations as it resembles two-magnon scattering of a quantum antiferromagnet in the paramagnetic state [5]. The dashed lines in Fig. 6.5 b) and c) show the corresponding results in crossed polarization (represented by a fit). The fact that the shape of the spectral weight for both samples is comparable suggests a comparable sample quality.

We observe a larger spectral weight of the continuum in the synthesized sample, especially in parallel xx polarization. For both samples there is less spectral weight at low energies in crossed yx polarization. This suggests the possibility of decomposing the spectral weight into a low and a high energy part, to which the allowed symmetry channels A_{1g}, A_{2g} and E_g contribute to varying extent. Previously, the spectral weight for magnetic excitations in the kagome lattice has been theoretically modelled separately for all three symmetry channels [71]. We

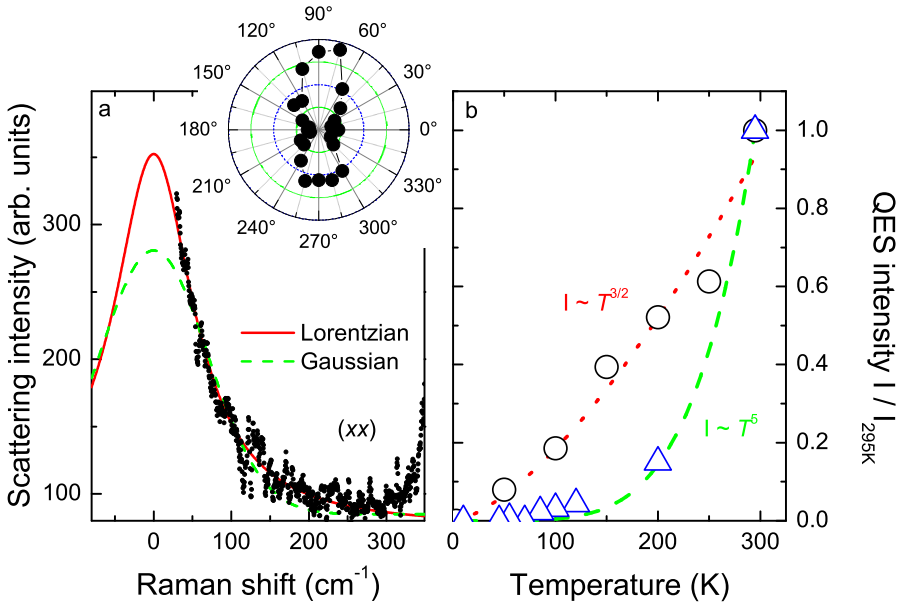

Figure 6.4: a) black dots: measured data. A gaussian (green curve) and a lorentzian (red curve) model fitted to the data. b) normalized intensity of the quasi-elastic contribution for the mineral sample (open triangles) and the synthesized crystal (open circles) together with power-law fits. The inset in a) shows the intensity of the QES at 295 K as function of the angle between the light scattering polarization and a fixed direction within the ab plane [59].

can estimate their magnitudes by carefully studying the rotational anisotropies of these signals as described later on. It is important to note that apart from the continuum we observe no further signal that could be interpreted as of magnetic origin. In particular, there are no sharp modes at low energies. This statement is assured down to energy scales of approximately 5-10 cm^{-1} (i.e. 0.04-0.08 J) as no upturn is visible at the edge of the experimentally accessible energy window.

Figure 6.6 a) zooms into the low frequency regime (up to 100 cm^{-1}) at low temperature ($T = 5$ K). There is a linear frequency dependence towards the maximum and we can use its slope as a measurand of the integrated intensity, less sensitive to fluorescence backgrounds. In Fig. 6.6 b) the slope of the low energy

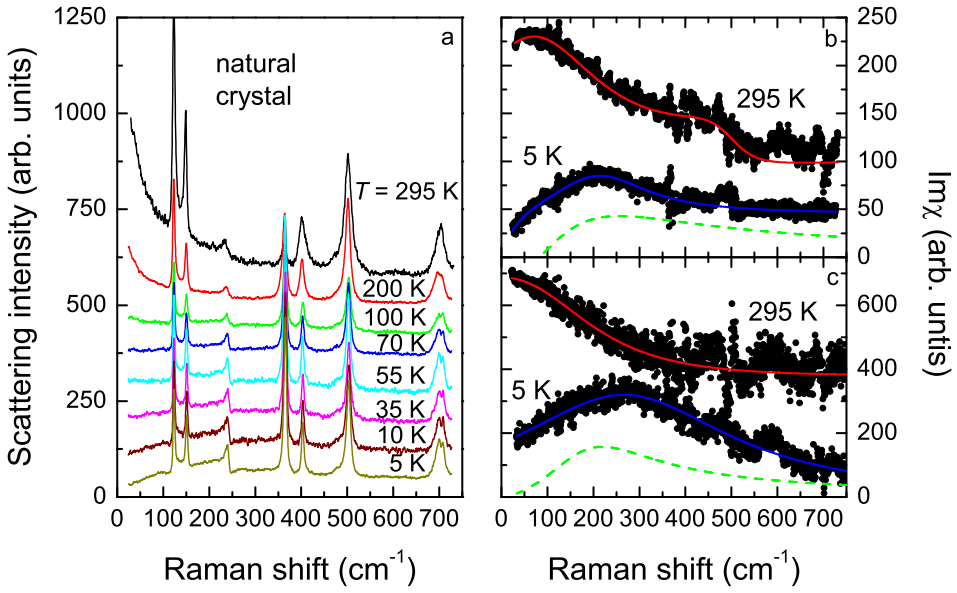

Figure 6.5: a) Temperature evolution of Raman spectra of the mineral sample in parallel xx polarization. Spectra are shifted in intensity for clarity. b) and c) show the Bose corrected spectra for the mineral crystal and the synthesized sample, respectively, with phonon modes subtracted (dots) together with a fit to the background. The dashed green lines in b) and c) correspond to the fitted background in crossed yx polarization at $T = 5$ K. The spectra at $T = 295$ K in b) and c) are shifted in intensity [59].

scattering is plotted as function of temperature. It increases approximately linearly with decreasing temperature ($T < 50$ K). Both samples show this linear temperature dependence. However, at higher temperatures the synthesized sample has again the more pronounced T dependence as shown in Fig. 6.6 c). Such a linear increase of scattering intensity is anomalous and not compatible with the expected Bose factor. However, it is frequently observed for magnetic Raman scattering in low dimensional spin systems that are close to quantum criticality.

Finally, in Fig. 6.7 we plot the rotational anisotropy of the low energy slope in xx and yx polarization (shown in a) and the rotational anisotropy of the intensity of the broad continuum (shown in b) in the mineral sample at $T = 5$ K. The low energy slope in a) shows a four fold E_g-like symmetry in parallel polarization, while in crossed polarization the rotational anisotropy is rather two-fold or of mixed character. The intensity of the broad continuum in b) was obtained by integrating over the signal, starting from 200 cm^{-1} to rule out contribution from

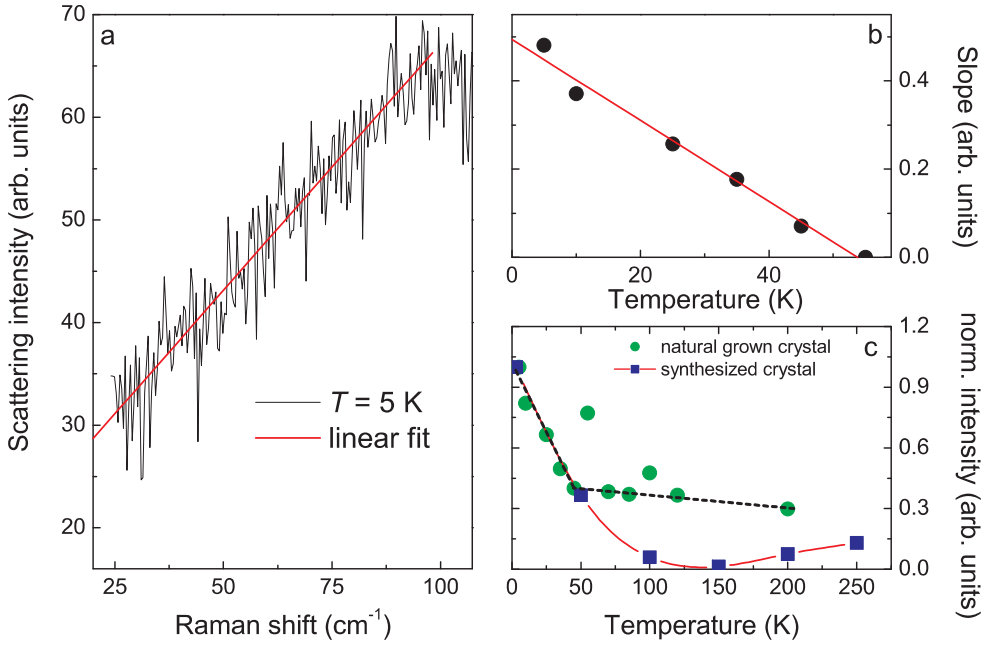

Figure 6.6: a) Linear fit to the low-frequency scattering in xx polarization of the mineral sample at $T = 5$ K. b) Temperature development of its slope including a linear fit. c) Temperature development of the intensity of the continuum in both the mineral and synthesized sample with guides to the eyes [59].

the low energy slope. It shows slight anisotropies in both xx and yx polarization.

It was suggested by Cépas et al. [72] that the formation of a valence bond crystal ground state leads to a weakly broken translation symmetry of the spin system. Thereby the magnetic Raman response of the kagome plane should depend in a decisive way on the relation of the polarization vectors in the ab plane, i.e. there should be characteristic intensity modulations of magnetic modes in the energy range of J when the polarizations are rotated within the plane, see Fig. 6.8, left panel, lower graph. In contrast, the "true" spin liquid exhibiting no broken symmetry should show a polarization independent magnetic Raman response (upper graph). Since experimental investigations using different techniques have up to now not observed a spin gap, the Raman experiment is highlighted to be potentially sensitive to even weakly broken symmetries in the kagome plane. It should be noted that in the second order perturbational treatment used by Cépas et al. magnetic scattering is only observed in E_g symmetry, as the A_{1g} component commutes with the used exchange scattering Hamiltonian.

Calculations based on a modified Shastry-Shraiman model by Ko, et al. [71] favor a $U(1)$ Dirac spin liquid as the ground state. In contrast to Cépas et al., this approximation also considers higher order terms, induced e.g. by electronic resonances of the photon energy with correlated states of the system. Here, the

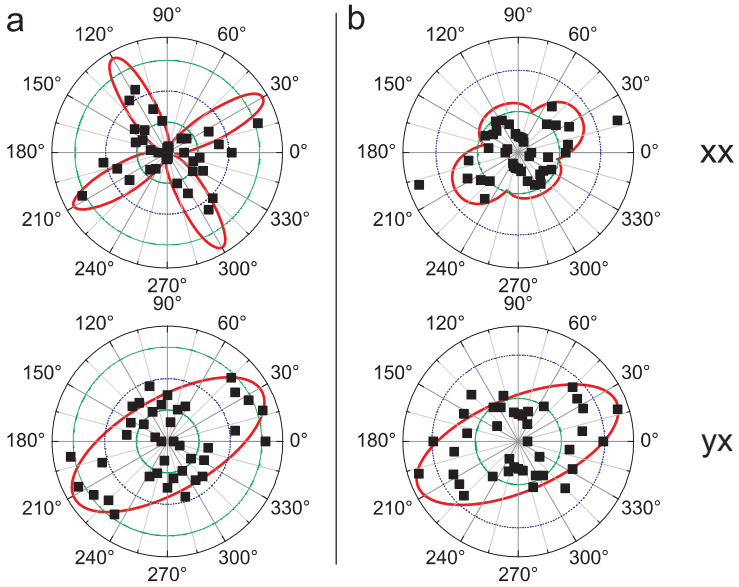

Figure 6.7: Angular dependence at $T = 5$ K of (a) the low-energy slope in the mineral sample and (b) its continuum intensity obtained in xx and yx polarization, respectively. The solid lines are obtained from superpositions of E_g and A_{1g} symmetries as guide to the eyes. Note that measurements were performed only in the range from 0° to 180°. The datasets were extrapolated to 360° assuming point symmetry [59].

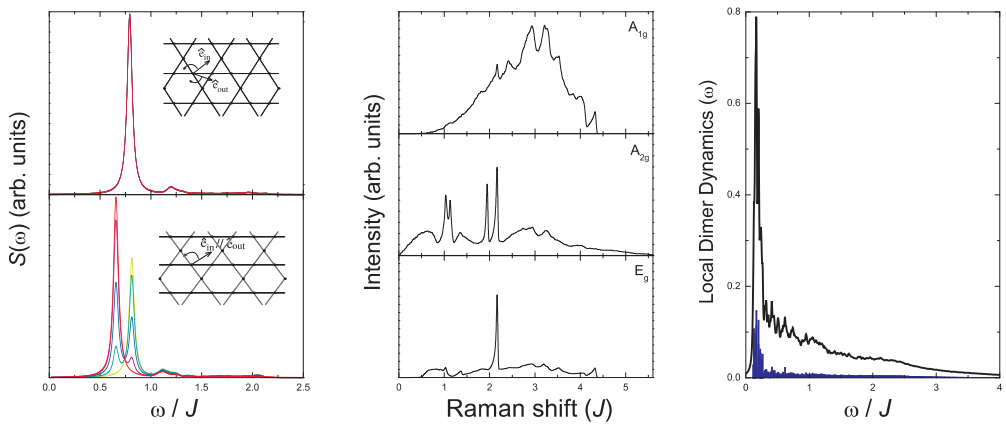

Figure 6.8: Left panel: Magnetic Raman cross-section based on the Fleury-Loudon model for a spin liquid (upper graph) and a RVB state (lower graph) for different orientations [72]. Center panel: Raman signature of a $U(1)$ Dirac spin liquid state, based on a higher order Shastry-Shraiman model. The final response is decomposed into the three contributing symmetry components [71]. Right panel: Dynamical singlet fluctuations obtained from large scale (N=36) exact diagonalization [73].

included chiral $\vec{s}\times\vec{s}$ component leads to additional scattering contributions in the A_{1g}, A_{2g} and E_g symmetry components. From the Raman tensors given above we notice that the now allowed A_{2g} component is only observed in yx polarization as a rotational invariant contribution. It does not contribute to xx polarization at all. The spectral distribution of the Raman scattering cross section derived by Ko, et al. shows a broad continuum that extends up to about 600 cm^{-1} ($\approx 5 \cdot J$), see center panel in Fig. 6.8.

In addition, Läuchli et al. [73] calculated dynamical singlet fluctuations on the kagome lattice using large-scale exact diagonalizations on a 36 site lattice. The results show a broad continuum extending over a range of 2 – 3J. There is also a pronounced intensity shooting up at lowest energies, $\omega/J \leq 0.2 \approx 25$ cm^{-1}, caused by a high density of low energy singlet and triplet excitations, see right panel in Fig. 6.8.

To analyze our observed scattering continuum, we decompose it into two contributions, that are both attributed to specific spin liquid excitations. The rotation dependence of the low energy slope (Fig. 6.7 a) shows a clear E_g-like contribution in xx polarization, while in the yx configuration it is oval shaped, most likely a mix of both E_g and A_{2g} symmetry. The dominance of the E_g channel at frequencies below 100 cm^{-1} is in contrast to theory [71]. The rotation dependence of the overall continuum's intensity (Fig. 6.7 b) shows a weak asymmetry in both xx and yx configurations for the mineral and the synthesized sample. This anisotropy has no dominant four-fold contribution. However, a superposition of a four-fold and a two-fold contribution leads to a good description of the scattering intensity. We conclude that the A_{1g} (for xx) and the A_{2g} (for yx) symmetry channels are major contributions for the continuum at an energy of $\approx 2J$. These components are proposed to be due to higher order perturbation theory [71]. Comparing our experimental data in crossed polarization to the data in parallel polarization, no clear separation of the respective spectral weight is evident.

This behavior is in contrast to the phonon Raman scattering, where modes of A_{1g} and E_g show clear selection rules and different in-plane anisotropies. In addition, the Fano-like line shape of phonons is only observed for modes with A_{1g} symmetry. On the other hand, phonon and magnetic scattering react differently on certain perturbations: (i) defects play a different role for the local spin excitations than for optical phonons at $q \approx 0$ with large coherence lengths, while (ii) DM interaction mixes singlet and triplet excitations. It is possible for DM interaction and defects such as antisite disorder to allow, further enhance and possibly mix A_{1g} and A_{2g} contributions, while spin defects in the plane reduce the magnetic scattering intensity. Therefore, a clear assignment of contributions from the A_{1g}, A_{2g} and E_g channels to the background is not straight forward. Still, the energy range and general shape of the observed background are in very good agreement with the above mentioned calculations by Ko, et al. [71].

The effect of impurities in the intermediate layer needs to be considered as well: Cu atoms in the intermediate layer may induce lattice deformations due to Jahn-Teller distortion, as well as additional magnetic coupling to the kagome Cu

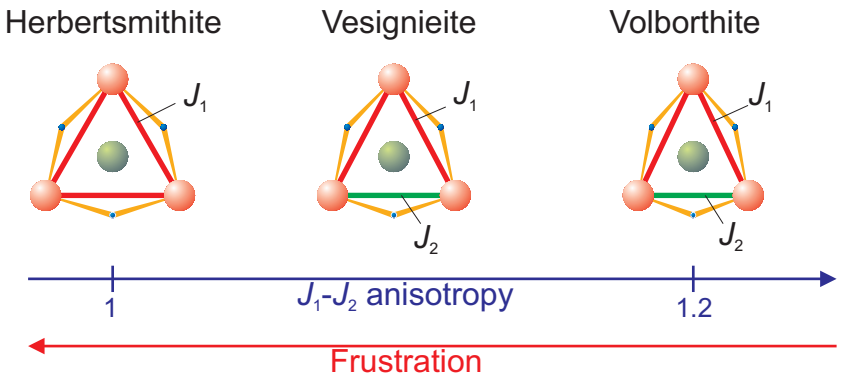

Figure 6.9: Schematic representation of the exchange interactions in herbertsmithite, and in the distorted kagome lattices vesignieite and volborthite.

atoms. Furthermore, the effect of non-magnetic impurities (i.e. Zn ions substituting Cu in the kagome layer) in quantum spin systems with dedicated low energy excitations can be exemplified using the frustrated dimer system $SrCu_2(BO_3)_2$, where 1-2% of Zn doping on Cu broadens the low energy excitations and considerably redistributes their spectral weight [5]. Indeed, our experimental data do not show sharp magnetic modes or a pronounced low energy maximum, in contrast to theory [71, 72]. In NMR experiments on herbertsmithite it has been shown that the local susceptibility in the proximity to such impurities is different and anomalous compared to the regular behavior [74]. With respect to Raman scattering it can be assumed that the excitations in the continuum that consist mainly of two-pair states [71] should be reduced in intensity, comparing the mineral and the synthesized sample. This reduction of scattering intensity can be clearly seen in Fig. 6.5 b) and c), together with a softening of about 20%.

6.6 Slightly distorted compounds volborthite and vesignieite

Aside from disorder and impurities, the effect of lattice distortions in kagome systems on the spin liquid ground state is an important issue. We therefore conducted a comparative Raman study on the two kagome lattice compounds vesignieite and volborthite [60]. At the time of the study, only powder samples were available. Therefore, rotational anisotropies could not be probed.

In both compounds volborthite ($Cu_3V_2O_7(OH)_2{\cdot}2H_2O$) and vesignieite ($BaCu_3V_2O_8(OH)_2$) the kagome planes are slightly distorted (see Fig. 6.9), resulting in two inequivalent Cu sites per triangle (Cu1 and Cu2). Such a reduced symmetry can either enhance or result from a spin gap, from dimerization, or from some kind of long range order. The crystal structure for both compounds is shown in Fig. 6.10.

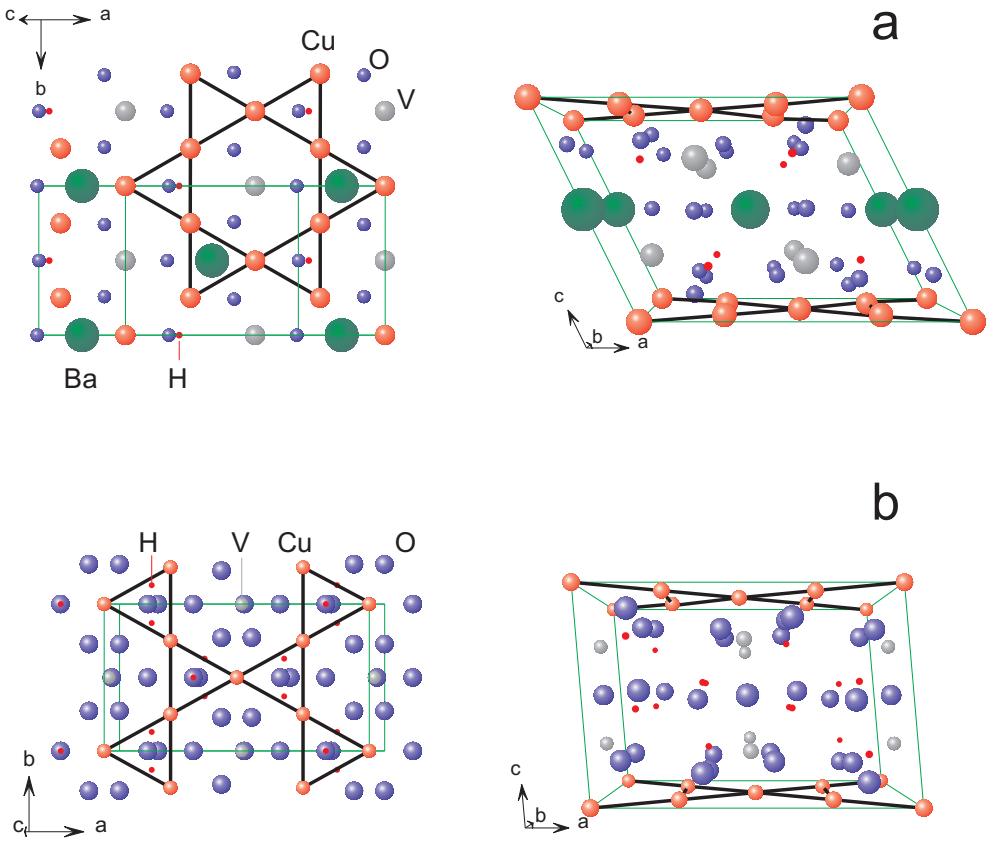

Figure 6.10: a) Crystal structure of vesignieite, b) crystal structure of volborthite. The left panels show the 2D kagome layers within the crystallographic ab plane, while the right panels show the stacking of the planes along the c axis. The solid black lines illustrate the cornersharing triangles.

For volborthite, the distortion leads to a difference in Cu1-Cu2 and Cu2-Cu2 bond length of about 3%, based on X-ray and neutron diffraction studies [75]. This results subsequently in two different magnetic exchange interactions J_1 and J_2. Theoretical modelling of thermodynamic properties suggests that the anisotropy is of the order of 20% or less [76] with an average value of $J_{volb} = 86$ K, as determined from magnetic susceptibility and specific heat measurements [77]. In magnetic susceptibility measurements a broad maximum is observed around 22 K that points to the onset of short-range magnetic order. Neutron scattering experiments detect nearest neighbor spin-spin correlations settling for temperatures below $T = 50$ K [78]. Finally, ^{51}V-NMR reveals a magnetic transition around $T = 0.9$ K, with anomalously slow energy spin fluctuations persisting down to lowest temperatures [79].

The kagome planes in vesignieite are less distorted, with a difference in bond length of only 0.07% [80]. The magnetic exchange interaction is determined as

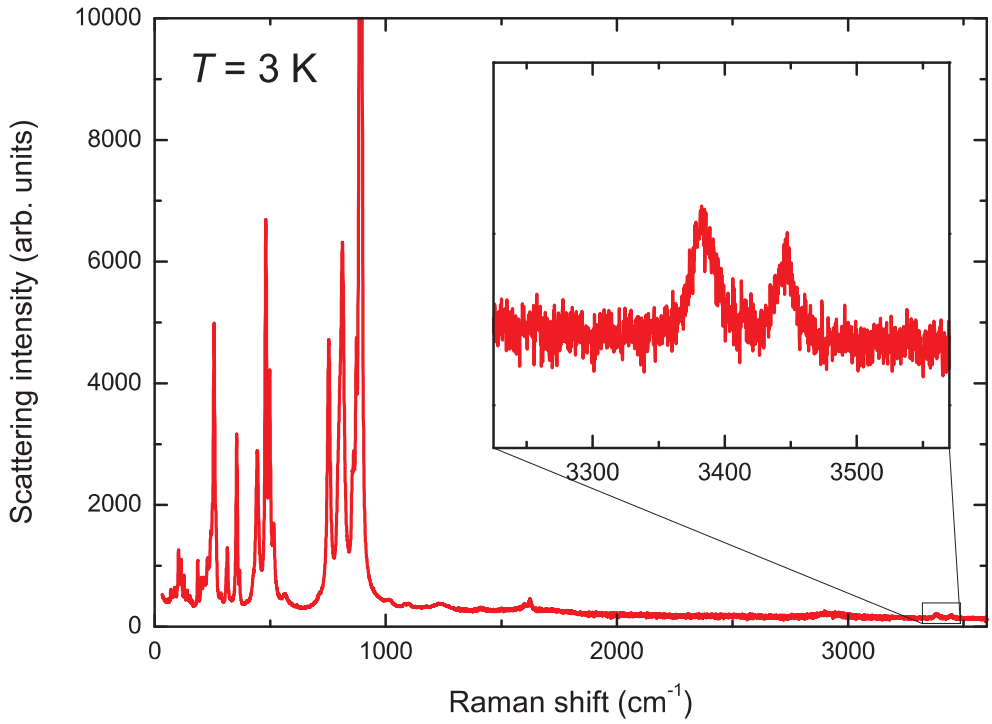

Figure 6.11: Raman spectrum of volborthite at $T = 3$ K and in xx polarization, ranging from 30 to 3600 cm^{-1}. The inset zooms into the high energy O-H modes.

$J_{vesi} = 53$ K. Bulk susceptibility measurements reveal a broad maximum around 21 K [81]. The estimated Dzyaloshinsky-Moriya (DM) interaction is around 0.14 J, i.e. larger than the quantum critical value of 0.1 J [23] and thus the ground state of vesignieite should be in the Néel-ordered regime [80]. Indeed, ^{51}V NMR shows a partial spin freezing at $T_c = 9$ K [82].

It is important to note that the drawback of antisite disorder, present in herbertsmithite, is avoided in both volborthite and vesignieite. Here, the intermediate layers are comprised of V^{5+} ions. Thus, antisite disorder of the Cu ions is prevented.

Both compounds volborthite and vesignieite belong to the monoclinic space group $C2/m$. A symmetry analysis [27] yields the following Raman active modes for volborthite: $\Gamma_{Raman} = 16A_g + 11B_g$ and for vesignieite: $\Gamma_{Raman} = 13A_g + 8B_g$. The corresponding Raman tensors are:

$$\mathrm{A}_g = \begin{pmatrix} a & d & 0 \\ d & b & 0 \\ 0 & 0 & c \end{pmatrix} \text{ and } \mathrm{B}_g = \begin{pmatrix} 0 & 0 & e \\ 0 & 0 & f \\ e & f & 0 \end{pmatrix}.$$

All measurements shown here are performed in xx polarization, i.e. with parallel incoming and scattered light. The crystallites in the powder sample are

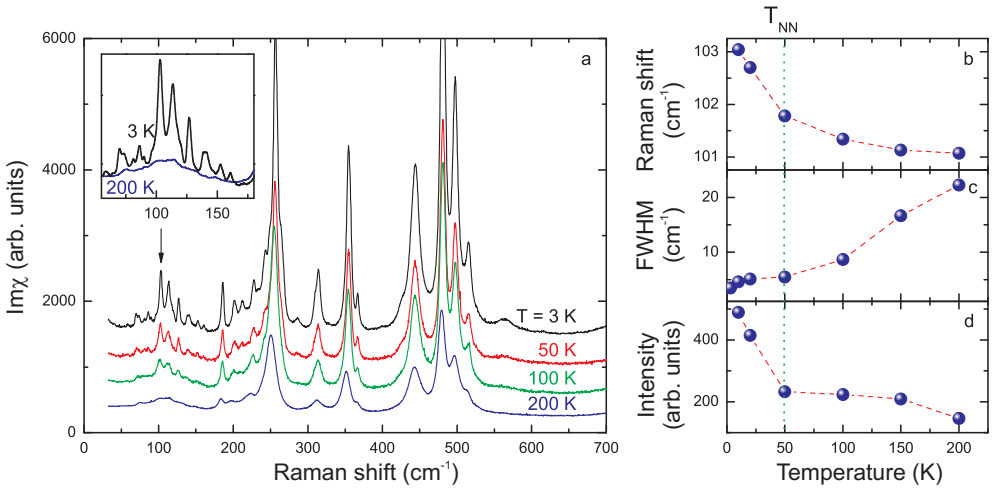

Figure 6.12: a) Bose-corrected Raman spectra of volborthite at T =3, 50, 100 and 200 K in xx polarization; the spectra are shifted in intensity for clarity. b) – d) Plots of frequency, linewidth and intensity of the phonon mode at 103 cm^{-1} (see arrow) as function of temperature. The inset zooms into the low energy regime for spectra obtained at 200 and 3 K [60].

semi-transparent and partially scramble the light polarization upon scattering. Polarization dependent experiments (not shown here) did not lead to additional information. In fact, the spectra obtained in crossed yx polarization are identical to the xx spectra. Both compounds show modes around 800 cm^{-1} and, as in herbertsmithite, around 3400 cm^{-1}, due to O-H vibrations (showcased for volborthite in Fig. 6.11). The energies of these modes correspond to 1150 K and 4900 K, and are therefore much larger than the magnetic exchange interaction. Hence, magnetic excitations do not interact with these phonon modes at high energy and we will only concentrate on the low energy spectral regime.

In Fig. 6.12 a) Raman spectra of volborthite are shown at different temperatures, ranging from 3 to 200 K. With decreasing temperature, the intensity of the phonons increases. Furthermore, in the low energy range below ≈ 175 cm^{-1}, a set of new, sharp phonons appears (see inset). The temperature evolution is showcased for one phonon at 103 cm^{-1} in Fig. 6.12 b) – d). The energy scale of this phonon group is in the range of $1J_{volb}$ – $3J_{volb}$.

The frequency evolution shown in Fig. 6.12 b) exhibits no anomalies, as a hardening of a few percent is expected from anharmonic effects according to the Grüneisen law when cooling from 200 K – 3 K. The linewidth in Fig. 6.12 c) shows a dramatic decrease with lowering temperature. The width is inverse proportional to the phonon lifetime. We attribute this temperature dependence to a pronounced anharmonicity of the lattice at high temperatures. The gradual freezing of these fluctuations is related to a symmetry lower than $C2/m$.

Finally, a strong gain of intensity is observed for temperatures below 50 K,

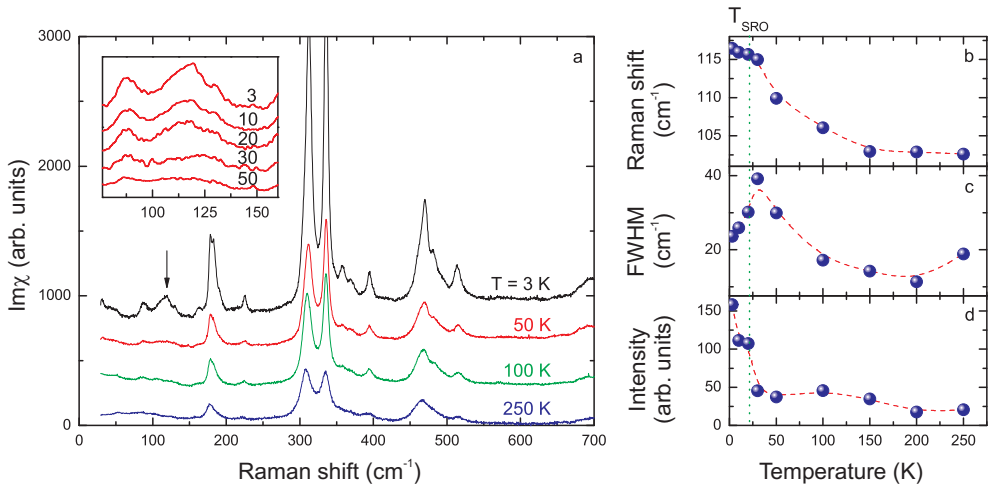

Figure 6.13: a) Bose-corrected Raman spectra of vesignieite at $T = 3$, 50, 100 and 250 K in xx polarization; the spectra are shifted in intensity for clarity. b) – d) Plots of the temperature development of the broad mode at 115 cm^{-1} (see arrow). The left inset in a) shows the spectral range of magnetic scattering for the temperature range 50 – 3 K [60].

see Fig. 6.12 d). Around this temperature, the onset of nearest neighbor spin-spin correlations is found in measurements of the magnetic susceptibility. At low temperatures at least 36 modes can be clearly differentiated. This total number exceeds the expected 27 modes. Therefore, we suggest that with decreasing temperature a gradual structural distortion occurs due to spin-phonon coupling. Through this moderate distortion, frustration is reduced. This is the first observation of a symmetry lowering in polycrystalline volborthite. Only very recently, volborthite single crystals were successfully synthesized. In the latter material a structural phase transition was observed at temperatures as high as 310 K, below which the symmetry is lowered from $C2/m$ to $I2/a$ due to orbital switching [83]. With this lower symmetry a total of $\Gamma_{Raman} = 26A_g + 25B_g$ Raman active phonon modes are expected. This number is in accordance with our Raman data at low temperatures taking an overlap of phonon modes as well as minor phonon intensities into account.

Fig. 6.13 a) plots the Raman spectra of vesignieite at different temperatures, in analogy to Fig. 6.12 a). The phonon modes sharpen and gain in intensity with decreasing temperature, comparable to the spectral changes in volborthite. In the whole spectral range we observe at low temperatures 19 phonon modes which is in good accordance with the expected 21 modes, i.e. there is no sign for structural distortion. In the low energy range a broader mode appears, extending from about 95 cm^{-1} to 140 cm^{-1}, or roughly $2.6J_{vesi}$ – $3.8J_{vesi}$ (see left inset). In contrast to the phonons, this mode has a different line shape that can not be described by a Lorentzian. While for the phonon modes a hardening of a few percent is com-

mon, the maximum frequency of this mode shifts by about 10 %, as shown in Fig. 6.13 b). Furthermore, the linewidth increases by a factor of 2 up to ∼25 K (Fig. 6.13 c)). This temperature is close to $T_{SRO} = 22$ K, where short-range magnetic correlations set in. Following the temperature development of the mode's intensity (Fig. 6.13 d)), it becomes strongly pronounced below about 25 K.

A broad spinon continuum as we observed in herbertsmithite is absent in vesignieite. Here, the mode at low temperatures is less broad, with an onset at a finite energy. Its maximum position around 115 cm^{-1} corresponds to $3.1 \cdot J_{vesi}$, with $J_{vesi} = 53$ K [81]. This is in very good agreement with the approximation of a typical energy for magnetic Raman scattering in a Heisenberg antiferromagnet [84] at $E_{2M} = 2J(zS - 1) = 110$ cm^{-1}, where $z = 5$ is the number of nearest neighbors and $s = 1/2$ is the spin. Additionally, the temperature behaviour of the mode's frequency, linewidth and intensity is very typical for a mode of magnetic origin (see, e.g., [85]). Therefore, we attribute this mode to a magnetic scattering process. The analogous approximation for volborthite leads to $E_{2M} = 180$ cm^{-1}. In this energy range no corresponding signal is observed. Instead, the observation of new phonon modes in volborthite hints towards an enhanced spin-lattice coupling.

6.7 Conclusion

In this chapter, the excitation spectra of three different kagome compounds and one slightly distorted triangular lattice system were studied and compared. In the structurally perfect $s = 1/2$ kagome lattice herbertsmithite, a broad, unstructured excitation continuum was observed at low temperatures due to spinon excitations, ranging from lowest energies up to $\sim 5 \cdot J$. A comparison between the mineral crystal with considerable antisite disorder and the synthesized sample with reduced antisite disorder revealed only minor differences, suggesting only a weak influence of this kind of defects on the spin dynamics. In addition, a strong quasi-elastic tail at high temperatures evidences substantial fluctuations of the magnetic energy density. Its temperature evolution points towards an algebraic spin liquid as the ground state of herbertsmithite.

These observations are fundamentally different from the spin dynamics in the slightly distorted kagome lattice compounds vesignieite and volborthite. In the former, a minor distortion results in a weak $J_1 - J_2$ anisotropy. In addition, a DM anisotropy of $0.14 \cdot J$ leads to an onset of short-ranged correlations below 22 K. Hence, a 2-magnon mode can be observed at an energy which is in accordance with the exchange interaction. Volborthite, on the other hand, with stronger distortions, has a $J_1 - J_2$ anisotropy of about 20 % which results in a strong spin-lattice coupling. The observation of new phonon modes below the onset temperature of nearest-neighbor spin-spin correlations evidences a lowering of the crystal symmetry with a subsequent reduction of spin frustration.

Chapter 7

Raman scattering in the triangular lattice system α-$CaCr_2O_4$

In this chapter we will discuss the magnetic excitation spectrum of a triangular lattice with $s = 3/2$, as realized in α-$CaCr_2O_4$ [86]. In contrast to the previously discussed kagome systems with corner-sharing triangles, this lattice is built up of edge-sharing triangles. While this model has been thoroughly studied theoretically, experimental realizations generally have to deal with small deviations from the model system: On the one hand, the existence of two slightly different nearest neighbor exchange interactions J_{nn} due to the formation of isosceles triangles can drive the system into a state of long range order, spin liquid, gapped dimer, or valence bond crystal, depending on the ratio of J_{nn1} and J_{nn2} [25]. On the other hand, an inclusion of next-nearest neighbor interactions J_{nnn} can induce a transition to a collinear phase when $J_{nnn}/J_{nn} > 0.125$ [87]. This raises important questions about the ground state and its low energy excitations if these two mentioned factors are integrated in a single lattice.

7.1 Crystal structure and magnetic properties

In the distorted delafossite α-$CaCr_2O_4$ the Cr^{3+} ($s = 3/2$) ions form a slightly distorted triangular lattice with substantial next-nearest neighbor interactions. There are four inequivalent nearest neighbor Cr^{3+}-Cr^{3+} distances varying between 2.889 Åand 2.939 Å[88, 89]. This leads to a spin network consisting of two straight and two zig-zag chains, see Fig. 7.1. Measurements of the magnetic susceptibility yield the mean strength of the exchange interaction $J_{mean} = 6.48$ meV ($\widehat{=}$ 75 K), the Curie-Weiss temperature $\Theta_{CW} = -564$ K, and the effective magnetic moment $\mu_{eff} = 3.68\mu_B$, i.e. close to the spin-only value of 3.87 μ_B [89]. An inelastic neutron scattering (INS) study extracted the following magnetic parameters: the average nearest neighbor exchange interaction $J^{av}_{nn} = 8.8(8)$ meV and the average next-nearest neighbor exchange interaction $J^{av}_{nnn} = 0.69$ meV [90]. Below $T_N = 42.6$ K, the compound orders magnetically with a helical 120°

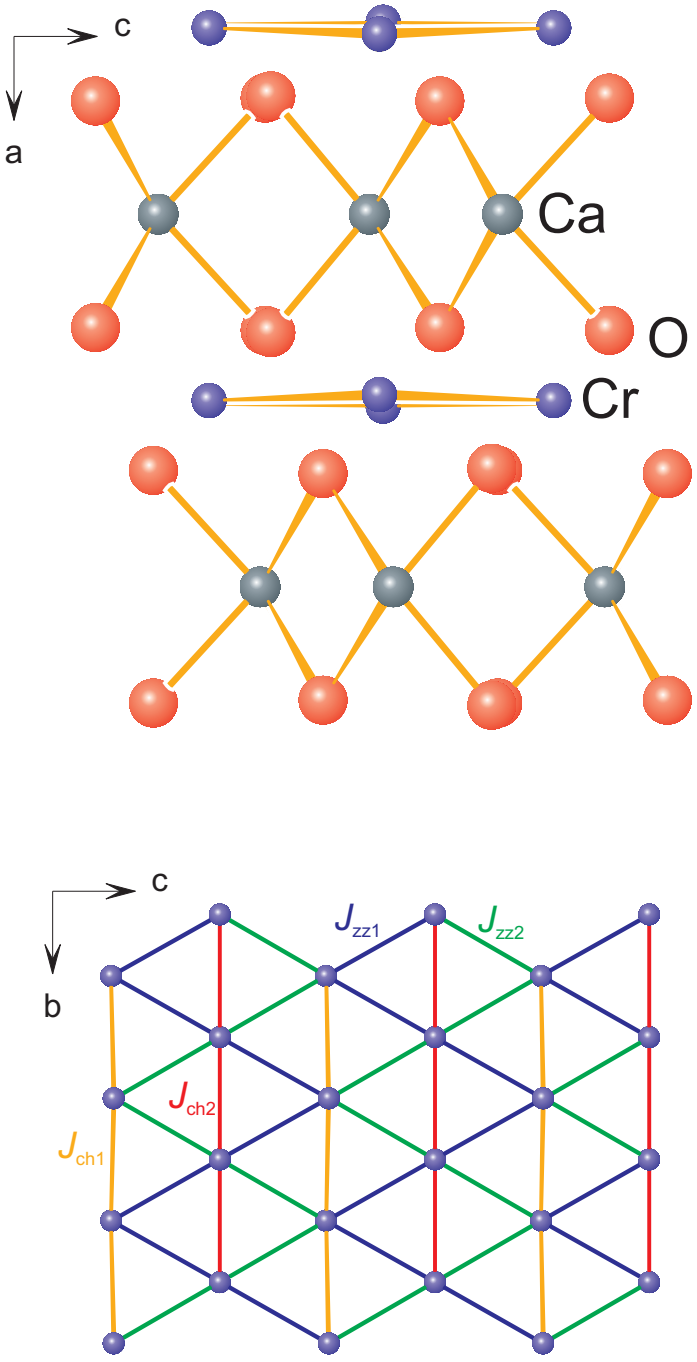

Figure 7.1: Crystal structure of α-$CaCr_2O_4$ within the ab-plane (upper panel) and within the bc-plane (lower panel). The 4 different direct exchange interactions between the Cr ions J_{ch1}, J_{ch2}, J_{zz1}, and J_{zz2} are color coded.

spin structure and an ordering wave vector $\vec{k} = (0, 0.3317, 0)$, i.e., close to the commensurate $\vec{k} = (0, 1/3, 0)$ [91]. This seems to prove the robustness of the 120° phase despite lattice distortions and higher-order interactions. However, INS experiments unveiled the softening of low energy modes with roton-like minima at wavevectors different from $\vec{k} = (0, 1/3, 0)$. This was taken as evidence that α-$CaCr_2O_4$ lies close to a quantum critical point to a new magnetic phase, possibly described by multiple wave vectors $\vec{k}$. These details make α-$CaCr_2O_4$ an ideal candidate to address the issue of deviations from the ideal triangular Heisenberg antiferromagnet on the ground state properties.

In proximity to a phase boundary, enhanced quantum fluctuations and thereby order by disorder can lead to a whole spectrum of effects for frustrated magnets [17]. One possibility for probing magnetic correlations is via electron spin resonance (ESR) measurements, performed at $\nu = 240$ GHz with a sweepable 12 T magnet [86]. In the paramagnetic regime at high temperatures, the Cr^{3+} ions give a sharp, lorentzian-shaped absorption signal. A considerable broadening together with a shift in resonance field is observed upon lowering the temperature due to the onset and further increase in spin-spin correlations, see Fig. 7.2. The signal can be observed below T_N if the external magnetic field H is oriented along the triangular plane, while it wipes out completely in the ordered regime for $H \perp$ to the plane. Further details of the spin dynamics are obtained from the temperature dependence of the line width. Here, two different models can be fitted to the critical broadening of ΔH_{pp} upon lowering the temperature towards T_N. The first fit $\Delta H_{pp} \propto (T - T_N)^{-p}$ (solid lines in Fig. 7.2 a)) yields a critical exponent $p = 0.385(0.483)$ for the out-of-plane (in-plane) direction. These values deviate by a factor of ~ 2 from the typical critical exponent found in triangular $s = 3/2$ 120° antiferromagnets (with $p \approx 0.7 - 0.9$, [92, 93, 94]). Hence, the spin dynamics in α-$CaCr_2O_4$ are different from those in the other systems. The second model is based on spin relaxation via magnetic vortices, which was a reasonable description for the related triangular lattice chromium oxides ACrO$_2$ ($A =$ H, Li, Na, Cu, Ag, Pd) with a 120° ground state [92, 93, 94]. Here, the spin-spin correlation length ξ determines the line broadening via $\Delta H_{pp} \propto \xi(T)^3$, with $\xi(T) = \xi_0 \exp(b/\tau^\nu)$ and $\tau = (T/T_m - 1)$. T_m is the 2D melting transition temperature. A fit of this model to the data (see dashed lines in Fig. 7.2 a)) matches well. However, the fit parameter for the exponent ν has a value of 0.07, which is one order of magnitude below the exponent found in the related chromium oxides ACrO$_2$ (with $\nu \approx 0.36 - 0.47$). Such a small exponent suggests the insignificance of vortices for the line broadening.

7.2 Phonon modes in α-$CaCr_2O_4$

The crystal structure of α-$CaCr_2O_4$ is orthorhombic (space group $Pmmn$) with four formula units per primitive cell [88]. The factor group analysis [27] yields for this crystal symmetry 36 Raman-active phonon modes: $\Gamma_{Raman} = 11 \cdot A_g + 6 \cdot$

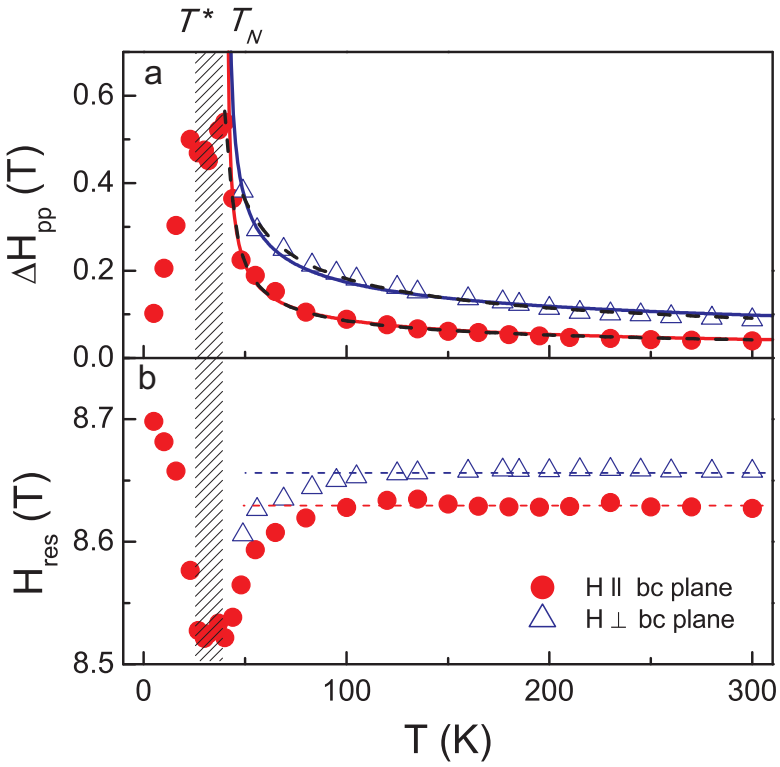

Figure 7.2: Temperature dependence of a) ESR line width and b) ESR resonance field. The full circles (open triangles) denote the in-plane (out-of-plane) field direction. The solid and dashed lines in panel a) are fits to the data. The dashed lines in panel b) mark the regime of constant resonance field. [86].

$B_{1g} + 11 \cdot B_{2g} + 8 \cdot B_{3g}$. The corresponding Raman tensors are given by:

$$\mathrm{A}_g = \begin{pmatrix} a & 0 & 0 \\ 0 & b & 0 \\ 0 & 0 & c \end{pmatrix}, \mathrm{B}_{1g} = \begin{pmatrix} 0 & d & 0 \\ d & 0 & 0 \\ 0 & 0 & 0 \end{pmatrix}, \mathrm{B}_{2g} = \begin{pmatrix} 0 & 0 & e \\ 0 & 0 & 0 \\ e & 0 & 0 \end{pmatrix}, \mathrm{B}_{3g} = \begin{pmatrix} 0 & 0 & 0 \\ 0 & 0 & f \\ 0 & f & 0 \end{pmatrix}.$$

All Raman scattering experiments are performed within the bc plane of the crystal due to the sample's thin, plate-like geometry. Phonon modes of B_{1g} and B_{2g} symmetry can only be observed in scattering experiments within the ab and ac plane, respectively. Therefore, only A_g and B_{3g} symmetry components contribute to our spectra. Single crystals of α-$CaCr_2O_4$ host three crystallographic twins with their unit cells rotated by an angle of $\pm$ 60° around the a axis. Therefore, neither the b nor the c axis is fixed with respect to the laboratory reference of frame and it is not possible to distinguish between A_g and B_{3g} phonon modes. An overview of the phonon spectrum is shown in Fig. 7.3. We can clearly observe 14 out of the expected 19 Raman-active phonon modes, marked by blue arrows. The discrepancy can be due to possible overlapping with phonons of larger intensities as well as a lack of pronounced phonon intensity.

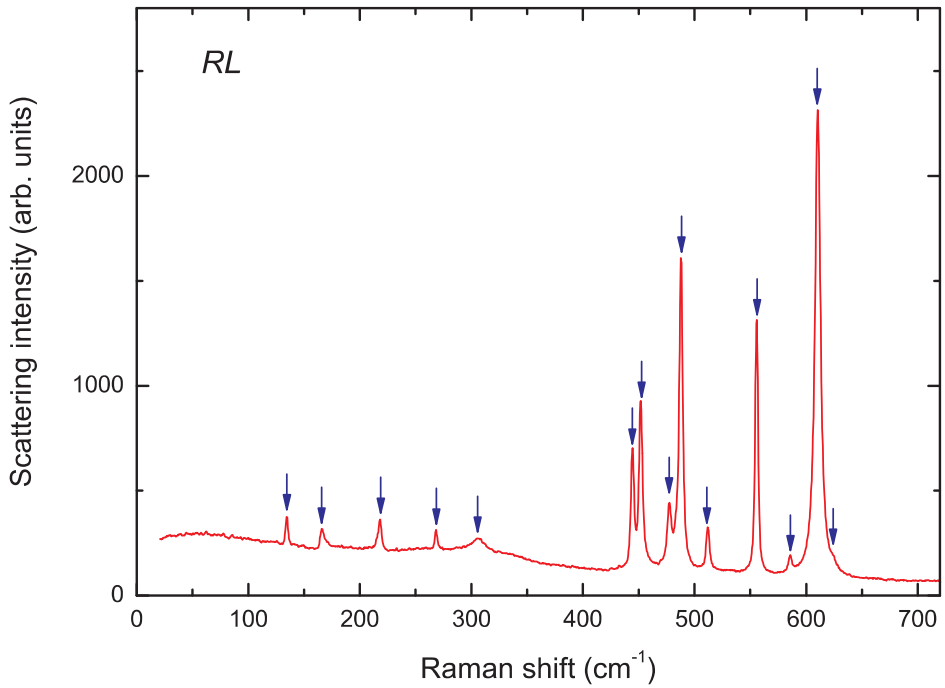

Figure 7.3: Raman spectrum of α-$CaCr_2O_4$ obtained at $T = 10$ K and in RL polarization. The arrows mark the 14 observed phonon modes.

7.3 Magnetic Raman scattering in α-$CaCr_2O_4$

A further understanding of the magnetic correlations in α-$CaCr_2O_4$ can be gained through magnetic Raman spectroscopy, which allows to directly probe the two-magnon spectrum and investigate the effect of magnon-magnon interactions on the spectral weight. In particular, the theoretical study on the dynamics of magnons in noncollinear antiferromagnets [95, 96] suggests a substantial amount of magnon-magnon interactions.

In contrast to square lattice antiferromagnets, the magnetic scattering from frustrated, undistorted triangular lattices should be independent of the in-plane scattering geometry of the incoming and outgoing light [95]. In the case of α-$CaCr_2O_4$, the small distortion might induce a minute anisotropy in the excitation spectra for different scattering geometries. However, the twinning will ultimately lead to an averaging of these anisotropies.

In the upper panel of Fig. 7.4, we show the low energy range (20 – 400 cm^{-1}) of Raman spectra obtained in different polarizations at $T = 10$ K. We observe a rather weakly structured background for the spectra in LL and RR polarization and an appreciable background scattering with a quasi-elastic tail in xx polarization. In RL polarization, an enhanced background is visible. For clarity, base lines are added to each curve. Subtracting all phonon modes from the RL spectrum yields the spectral weight shown in the lower panel of Fig. 7.4. As the back-

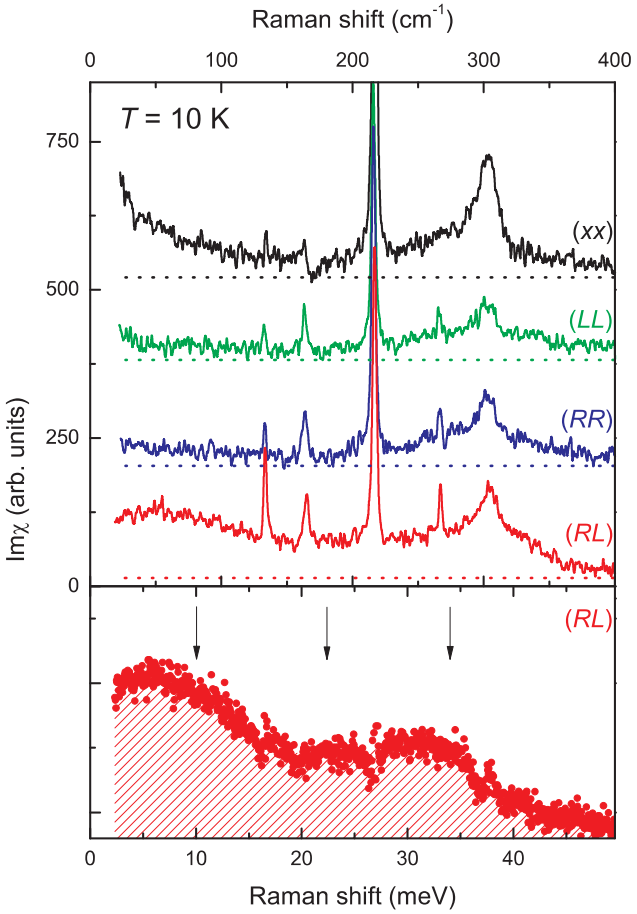

Figure 7.4: Bose corrected Raman spectra of α-$CaCr_2O_4$ obtained for different light polarizations xx, LL, RR, and RL at $T = 10$ K [86]. The spectra are shifted in intensity for clarity. The dashed horizontal lines mark the background for each spectrum. The lower panel displays the spectrum obtained in RL polarization with the phonon lines subtracted. The three black arrows mark twice the roton energy obtained from INS [90].

ground is very broad and mostly pronounced in the RL polarization and shows no dependence on laser wavelength (see Fig. 7.5 a)), we exclude a phonon density of states as a possible origin. Recent INS studies on powder samples revealed magnetic excitations in α-$CaCr_2O_4$ ranging from lowest energies up to around 320 cm^{-1} ($\widehat{=}$40 meV, see Fig. 7.5 b) and [90]). In particular, the shift of the spectral weight toward lower energies observed in Raman spectroscopy is comparable to the monotonic increase of the momentum averaged neutron scattering intensity. Judging from the energy range and spectral form (compare the lower panel of Fig. 7.4 to Fig. 7.5 b)), we ascribe this signal to a two-magnon like scattering.

As mentioned above, the two-magnon scattering of an ideal triangular lattice

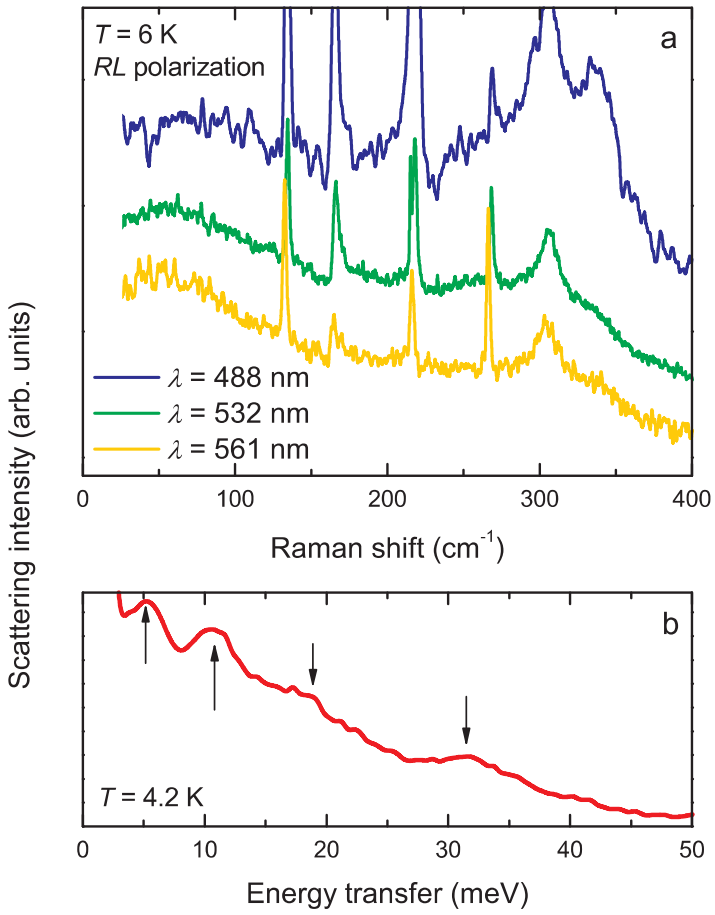

Figure 7.5: a) Magnetic Raman scattering in α-$CaCr_2O_4$ probed with three different laser lines. The spectra are shifted in intensity for clarity. b) van-Hove singularities observed in inelastic neutron scattering experiments [90].

shows no directional dependence, i.e. the magnetic scattering intensity should be the same in xx and yy polarization. This isotropic behaviour can be checked by inspecting the circular polarized spectra: The RR and LL polarizations correspond to $xx-yy-i(xy+yx)$ and $xx-yy+i(xy+yx)$, respectively, with $R = x-iy$ and $L = x+iy$. Therefore, we expect little to no magnetic contribution in both RR and LL polarization. Consistently, the magnetic background is hardly discernible, see upper panel in Fig. 7.4. In contrast, the RL polarization corresponds to $xx+yy+i(xy-yx)$ and thus the magnetic contributions from the xx and yy polarizations (i.e. the A_g and the B_{3g} components) add up. Indeed, we observe a pronounced magnetic continuum in the RL scattering configuration.

For the case of the ideal triangular lattice, the xx and the RL polarization spectra should scale with each other. Overall, both the xx and RL polarization spectra show a similar shift of the spectral weight toward lower energies. How-

ever, the RL polarization spectrum possesses several maxima around 46, 184, and 250 cm^{-1} (see Fig. 7.4) while the xx polarization spectrum shows a strong quasi-elastic like tail for energies below 160 cm^{-1} (20 meV) with a broad maximum around 266 cm^{-1} (33 meV). The latter is explained by the huge spectral weight at $\omega \approx 0$ observed in INS [90]. In addition, the more pronounced structure in the RL spectrum is due to deviations from the ideal triangular lattice and implies a complex exchange topology.

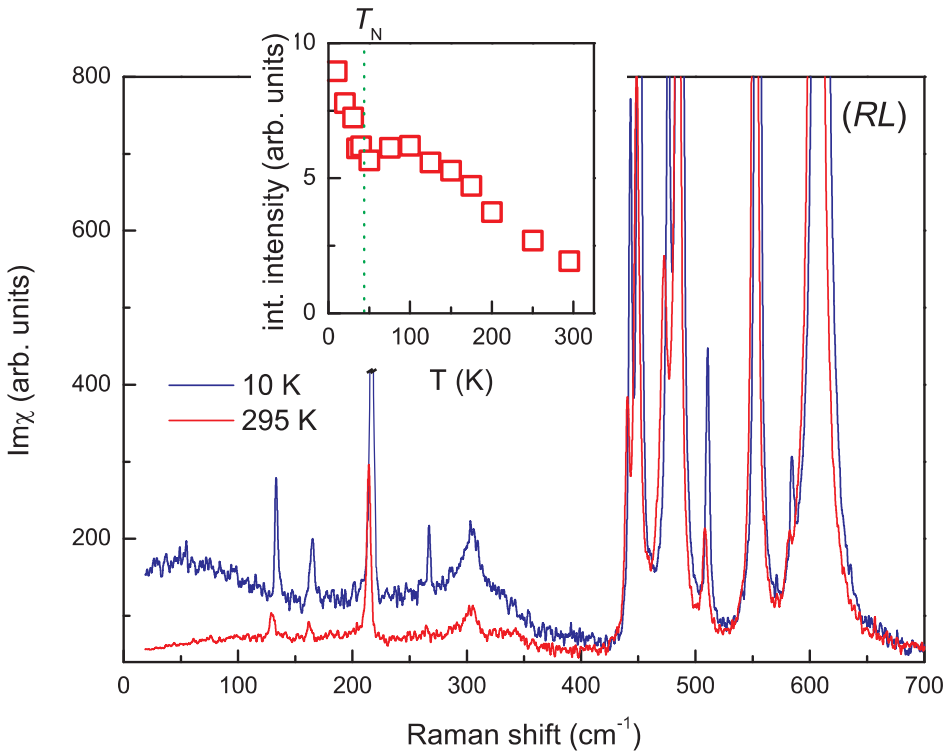

Figure 7.6: Comparison of the Bose corrected spectra obtained in RL polarization at 10 K (blue curve) and 295 K (red curve). The inset shows the integrated intensity of the spectral weight as shown in the lower panel of Fig. 7.4 over temperature [86].

Fig. 7.6 compares two spectra obtained at $T = 10$ K and 295 K in RL polarization. The phonon modes show a moderate hardening together with a gain in intensity upon cooling. Overall, the temperature dependence of the phonon parameters can be explained by lattice anharmonicities. The magnetic continuum, observed strongest in RL symmetry, increases in spectral weight with decreasing temperature. For a square lattice, with increasing temperature through T_N the spectrum dampens and the peak energy renormalizes strongly [97]. However, there is no substantial change in the width and the position of the two-magnon continuum in a wide temperature range for our case. In contrast, only a gradual

suppression of the spectral weight is associated with the characteristic feature of a frustrated system, that is, the persistence of locally correlated magnetic states. The inset in Fig. 7.6 plots the integrated intensity of the magnetic continuum over temperature. Around $T_N = 43$ K, a sudden change in slope occurs, marking the crossover from short range magnetic correlations to long range magnetic order.

The two-magnon scattering mechanism for conventional square lattices is well established. The bare two-magnon density of states has a van-Hove singularity due to a flat magnetic dispersion at the Brillouin zone boundary. Magnon-magnon interactions broaden the singularity and shift the maximum intensity down to $E_{max} = J(2zs - 1)$. Here, J is the magnetic exchange constant, z is the number of magnetic bonds (i.e. nearest neighbors) and s is the spin quantum number. This picture is well confirmed by experimental results (e.g. for $LaSrMnO_4$, see [97]). However, the same argument cannot be applied to frustrated spin systems. Actually, the estimated peak position of $E_{max} = 17J \approx 880$ cm^{-1} with $s = 3/2$ and $z = 6$ is much higher than the high-energy cut-off of the magnetic spectral weight at around 440 cm^{-1}. In comparison, the previously discussed highly frustrated $s = 1/2$ kagome lattice system $ZnCu_3(OH)_6Cl_2$ shows a broad continuum located at about $2\ J$ with no clear cutoff but a moderate suppression at higher energy scales above $6\ J$ [59]. This is also contrasted by the $s = 1/2$ square lattice, which has a dominant spectral weight around $2.7J$.

In a 2D triangular lattice, quantum corrections cause a substantial downscaling of the spectral weight due to the increased level of frustration and strongly modify the shape of the magnon dispersion [95]. For $s = 1/2$, the one-magnon dispersion is characterized by shallow roton-like minima and a flat region extending over a wide range of the Brillouin zone. This leads to two van-Hove singularities in the Raman response. As a result, the bare two-magnon profile has two peaks. This feature will be smeared out due to magnon-magnon scatterings and especially the high energy peak is strongly suppressed due to larger magnon damping. Thus, a broad, rather symmetric Raman continuum appears with the round maximum around twice the roton energy.

For $s = 3/2$, the spectral weight is expected to shift towards the higher energy region. In contrast, the two-magnon continuum of α-$CaCr_2O_4$ gradually increases with decreasing energy. Its intensity is drastically suppressed for frequencies above 440 cm^{-1} ($\approx$ 55 meV) and the weak signal cannot be differentiated from the strong phonon peaks. The same features, in particular, the pronounced spectral weight at low energies, have been observed in the one-magnon spectrum by INS. They were attributed to mode softening due to the instability toward the neighboring new magnetic structure. Additionally, INS experiments show van-Hove singularities around 5, 11, 17, and 33 meV. We mark twice these energies by black arrows on top of the two-magnon continuum (see the lower panel of Fig. 7.4). At the respective energies, we find the substantial spectral weights. The three broad peaks identified in our data are related to low-energy roton-like modes. The minor discrepancies in energy are due to the different scattering matrix element between INS and Raman scattering. The multi-peak feature suggests

that α-$CaCr_2O_4$ is close to a new magnetic (multi-k) phase.

7.4 Conclusion

The $s = 3/2$ compound α-$CaCr_2O_4$ forms 2D layers of slightly distorted, edge-sharing triangles. Despite the exchange geometry with minute anisotropies a seemingly robust 120° ground state is formed as in perfect, undistorted triangular lattices. However, a strongly renormalized and structured two-magnon continuum evidences substantial magnon-magnon interactions and the system's proximity to a different magnetic phase, described by multiple k-vectors.

Chapter 8

Summary

In this thesis magnetic excitation spectra in disordered, short-range-, and long-range ordered phases are investigated as a function of temperature and the degree of spin frustration.

The first discussed compound is the quasi-1D $s = 1/2$ chain system $TiPO_4$. The spin chains start to distort around 111 K and finally dimerize due to a spin-Peierls instability below 74 K. This intermediate temperature regime is dominated by unusually strong lattice fluctuations and the formation of a spin gap. Below 74 K the lattice resumes its static behaviour. Upon crossing from the uniform into the dimerized phase, the character of magnetic excitations changes from fermionic to bosonic. The rich magnetic excitation spectrum allows us to extract a value for the spin gap. In addition, a sharp, high energy mode with a decisive polarization and temperature dependence was identified as a mixed magnetic-electronic excitation.

$Sr_3Cr_2O_8$ realizes a three dimensional network of weakly coupled dimers. A Jahn-Teller distortion drives the system into an orbitally ordered state with a spin gap. Our Raman data uncovers an extended temperature regime of strong orbital fluctuations below the Jahn-Teller transition, as evidenced by strong quasi-elastic scattering. The development of its intensity as function of temperature is directly related to the heat capacity and allows an independent determination of both the structural transition temperature T_S as well as the orbital ordering temperature T^*. From the observation of a soft mode in the orbitally ordered regime, we can estimate the orbital gap $\Delta_{JT} = 450$ K. Finally, 2-magnon as well as more exotic 3-magnon scattering signals at low temperatures yield a spin gap of $\Delta = 40$ K. $Ba_3Cr_2O_8$, on the other hand, which is isostructural to $Sr_3Cr_2O_8$ exhibits no such fluctuations. The energies (intradimer-, interdimer-interaction, characteristic temperatures and critical fields) in this system are scaled down, but show the same hierarchy as $Sr_3Cr_2O_8$. On the other hand, their ratios are slightly different. This leads to a stable ground state without a critical fluctuation regime.

The three highly frustrated quantum spin systems herbertsmithite, vesigniete and volborthite realize 2D kagome lattice structures. The highest degree of frus-

tration is achieved in herbertsmithite, which is not plagued by lattice distortions. In fact, this compound was discussed as a promising candidate to realize a spin liquid ground state. Our temperature dependent Raman study reveals a broad continuum of gapless, fractional spinon excitations at low temperatures, ranging from the lowest energy up to $\sim 5 \cdot J$ with its maximum around $2 \cdot J$. Additionally, we observe magnetic correlations decaying by a power law with temperature. These observations evidence a gapless algebraic spin liquid as herbertsmithite's ground state, despite its sizeable amount of Zn/Cu antisite disorder. The degree of frustration in vesignieite and volborthite is reduced due to a small lattice distortion. Consequently, in vesignieite short range spin-spin correlations are observed at low temperatures which culminate in a bosonic 2-magnon like signal, while volborthite exhibits a lattice distortion at low temperatures, thus partly removing the frustration.

Moving from the kagome (i.e. corner-shared triangular) lattice to the edge-shared triangular lattice has again a huge impact on the magnetic properties of the compound. While originally edge-shared triangular systems were also discussed in the framework of spin liquids, it was found that they order in a 120° ground state. However, the influence of lattice distortions on the ordered state is yet to be resolved. In α-$CaCr_2O_4$, the distorted triangular lattice leads to a complex network of different magnetic exchange paths. Our magnetic Raman scattering study reveals a strongly renormalized and structured two-magnon continuum due to considerable magnon-magnon interactions. This evidences that the lattice distortions push the system to the edge of a new magnetic phase, different from its 120° ground state.

The plethora of observed phenomena in the systems studied in the framework of this thesis highlights the importance of hierarchy of energy scales in correlated electron systems as well as the versatility of inelastic light scattering.

Appendix A

List of investigated samples

- **$TiPO_4$**

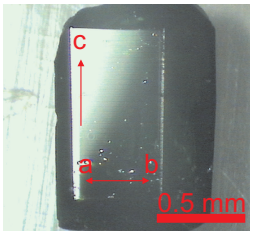

Figure A.1: Photo of the measured sample piece of $TiPO_4$.

The single crystal was grown in the group of Prof. R. Glaum, Institut für anorganische Chemie, University of Bonn, and kindly provided by Dr. R. K. Kremer, Max Planck Institut für Festkörperphysik, Stuttgart.

- **$Sr_3Cr_2O_8$**

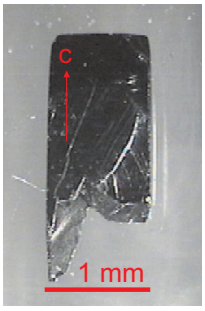

Figure A.2: Photo of the measured sample piece of $Sr_3Cr_2O_8$.

The single crystal was grown by A. T. M. N. Islam in the group of B. Lake, Helmholtz Zentrum Berlin für Materialien und Energie.

- **$Ba_3Cr_2O_8$**

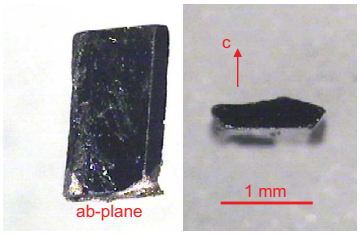

Figure A.3: Photo of the measured sample piece of $Ba_3Cr_2O_8$.

The single crystal was grown by Hiroaki Ueda at the Institute of Solid State Physics, University of Tokyo, Japan.

- **$ZnCu_3(OH)_6Cl_2$**

  - natural grown crystals

Figure A.4: Photo of a mineral (naturally grown) herbertsmithite single crystal [98].

The investigated sample was obtained from a copper mine in Chile and kindly provided by Ph. Mendels, Univ. Paris-Sud.

- synthesized single crystal

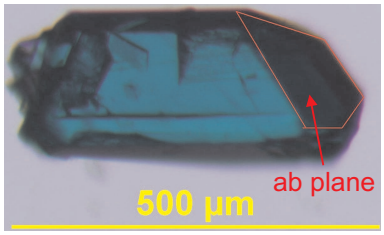

Figure A.5: Photo of the measured synthesized single crystal herbertsmithite. This photo was kindly provided by Tianheng Han, MIT Massachusetts.

The sample was hydrothermally grown by T. Han et al. at the MIT Massachusetts.

- series of powder samples: $ZnCu_3(OD)_6Cl_2$ and $Zn_{1+x}Cu_{4-x}(OH)_6Cl_2$

Both a powder sample of deuterated herbertsmithite (i.e. $ZnCu_3(OD)_6Cl_2$) and a series of zinc paratacamite ($Zn_{1+x}Cu_{4-x}(OH)_6Cl_2$, with $x = 0.5, 0.85, 1.0, 1.1, 1.2, 1.4$) were synthesized by Mark de Vries, Univ. of Edinburgh.

- **Vesignieite and volborthite**

  Powder samples of vesignieite and volborthite were synthesized by Hiroyuki Yoshida at NIMS Tsukuba and Yoshihiko Okamoto and Zenji Hiroi at the ISSP Tokyo, in Japan.

- **$CaCr_2O_4$**

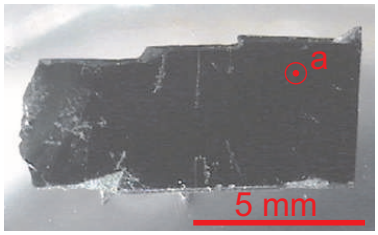

Figure A.6: Photo of the measured sample piece of α-$CaCr_2O_4$.

The single crystal was grown by A. T. M. N. Islam in the group of B. Lake, Helmholtz Zentrum Berlin für Materialien und Energie.

Appendix B

List of publications

- *Anomalous low-temperature behavior of the Co dimers in the oxo-halide* $CoSb_2O_3Br_2$, Z. Hugonin, M. Johnsson, S. Lidin, D. Wulferding, P. Lemmens, R.K. Kremer, Journal of Solid State Chemistry **181** 2776 (2008).
- *Lattice and electronic anomalies of* $CaFe_2As_2$ *studied by Raman spectroscopy*, K.-Y. Choi, D. Wulferding, P. Lemmens, N. Ni, S. L. Bud'Ko, P. C. Canfield, Phys. Rev. B **78** 212502 (2008).
- *Separation of the oxide and halide part in the oxohalide* $Fe_3Te_3O_{10}Cl$ *due to high lewis acidity of the cations*, D. Zhang, M. Johnsson, H. Berger, R. K. Kremer, D. Wulferding, P. Lemmens, Inorganic Chemistry **48** 6599 (2009).
- *Interplay of electronic correlations and lattice instabilities in* $BaVS_3$, Kwang-Yong Choi, Dirk Wulferding, Helmuth Berger, Peter Lemmens, Phys. Rev. B **80** 245108 (2009).
- *Optical phonons, spin correlations, and spin-phonon coupling in the frustrated pyrochlore magnets* $CdCr_2O_4$ *and* $ZnCr_2O_4$, Ch. Kant, J. Deisenhofer, T. Rudolf, F. Mayr, F. Schrettle, A. Loidl, V. Gnezdilov, D. Wulferding, P. Lemmens, V. Tsurkan, Phys. Rev. B **80** 214417 (2009).
- *A molecular magnet confined in the nanocage of a globular protein*, R. K. Mitra, P. K. Verma, D. Wulferding, D. Menzel, T. Mitra, A. M. Todea, P. Lemmens, S. K. Pal, ChemPhysChem **11** 389 (2010).
- *Microwave absorption in the frustrated ferrimagnet* Cu_2OSeO_3, M. I. Kobets, K. G. Dergachev, E. N. Khatsko, A. I. Rykova, P. Lemmens, D. Wulferding, H. Berger, Low Temperature Physics / Fizika Nizkikh Temperatur **36** 176 (2010).
- *Synthesis, crystal structure, and magnetic properties of the copper selenite chloride* $Cu_5(SeO_3)_4Cl_2$, Dong Zhang, Helmuth Berger, Reinhard K. Kremer, Dirk Wulferding, Peter Lemmens, and Mats Johnsson, Inorganic Chemistry **49** 9683 (2010).

- *Interplay of thermal and quantum spin fluctuations in the kagome lattice compound herbertsmithite*, D. Wulferding, P. Lemmens, P. Scheib, J. Röder, Ph. Mendels, S. Chu, T. Han, and Y. S. Lee, Phys. Rev. B **82**, 144412 (2010).

- *Coupled spin-lattice fluctuations in a compound with orbital degrees of freedom: The Cr-based dimer system $Sr_3Cr_2O_8$*, D. Wulferding, P. Lemmens, K.-Y. Choi, V. Gnezdilov, Yu. G. Pashkevich, J. Deisenhofer, D. Quintero-Castro, A. T. M. N. Islam, and B. Lake, Phys. Rev. B **84**, 064419 (2011).

- *Anomalous low-energy phonons in nearly tetragonal $BiFeO_3$ thin films*, K.-Y. Choi, S. H. Do, P. Lemmens, D. Wulferding, C. S. Woo, J. H. Lee, K. Chu, and C.-H. Yang, Phys. Rev. B **84**, 132408 (2011).

- *Extension of the zinc paratacamite phase diagram: Probing the effect of spin vacancies in an $S = 1/2$ kagome antiferromagnet*, M. A. de Vries, D. Wulferding, P. Lemmens, J. S. Lord, A. Harrison, P. Bonville, F. Bert, and P. Mendels, Phys. Rev. B **85**, 014422 (2012).

- *Phononic and magnetic excitations in the quasi-one-dimensional Heisenberg antiferromagnet $KCuF_3$*, V. Gnezdilov, J. Deisenhofer, P. Lemmens, D. Wulferding, O. Afanasiev, P. Ghigna, A. Loidl, and A. Yeremenko, Low Temperature Physics / Fizika Nizkikh Temperatur **38** 5, 538 (2012).

- *The spin dynamics in distorted kagome lattices: a comparative Raman study*, D. Wulferding, P. Lemmens, H. Yoshida, Y. Okamoto, and Z. Hiroi, J. Phys.: Condens. Matter **24**, 185602 (2012).

- *Crossover from coherent to incoherent scattering in spin-orbit dominated Sr_2IrO_4*, Mehmet Fatih Cetin, Peter Lemmens, Vladimir Gnezdilov, Dirk Wulferding, Dirk Menzel, Tomohiro Takayama, Kei Ohashi, and Hidenori Takagi, Phys. Rev. B **85**, 195148 (2012).

- *Tailoring defect structure and optical absorption of porous anodic aluminium oxide membranes*, Hongdan Yan, Peter Lemmens, Dirk Wulferding, Jianmin Shi, Klaus Dieter Becker, Chengtian Lin, Aidin Lak, and Meinhard Schilling, Materials Chemistry and Physics **135**, 206 (2012).

- *Dynamical lattice instability versus spin liquid state in a frustrated spin chain system*, V. Gnezdilov, P. Lemmens, Yu. G. Pashkevich, D. Wulferding, I. V. Morozov, O. S. Volkova, and A. Vasiliev, Phys. Rev. B **85**, 214403 (2012).

- *Low-dimensional magnetism of spin-1/2 chain systems α- and β-$TeVO_4$: a comparative study*, V. Gnezdilov, P. Lemmens, D. Wulferding, Yu. Pashkevich, K. Lamonova, K.-Y. Choi, O. Afanasiev, S. Gnatchenko, and H. Berger, Low Temperature Physics / Fizika Nizkikh Temperatur **38** 7, 715 (2012).

- *New Perspectives for Cuprate Research: $(Ca_xLa_{1-x})(Ba_{1.75-x}La_{0.25+x})Cu_3O_y$ Single Crystals*, Gil Drachuck, Meni Shay, Galina Bazalitsky, Rinat Ofer, Zaher Salman, Alex Amato, Christof Niedermayer, Dirk Wulferding, Peter Lemmens, Amit Keren, J. Supercond. Nov. Magn. **25**, 2331 (2012).

- *Softened magnetic excitations in the $s = 3/2$ distorted triangular antiferromagnet α-$CaCr_2O_4$*, D. Wulferding, K.-Y. Choi, P. Lemmens, A. N. Ponomaryov, J. van Tol, A. T. M. N. Islam, S. Toth, and B. Lake, J. Phys.: Condens. Matter **24**, 435604 (2012).

- *Ultrafast excited state deactivation of doped porous anodic alumina membranes*, Abhinandan Makhal, Soumik Sarkar, Samir Kumar Pal, Hongdan Yan, Dirk Wulferding, Fatih Cetin, and Peter Lemmens, Nanotechnology **23**, 305705 (2012).

- *Evidence for Dimer Crystal Melting in the Frustrated Spin-Ladder System $BiCu_2PO_6$*, K.-Y. Choi, J. W. Hwang, P. Lemmens, D. Wulferding, G. J. Shu, and F. C. Chou, Phys. Rev. Lett. **110**, 117204 (2013).

- *Interplay between lattice and spin states degree of freedom in the FeSe superconductor: Dynamic spin state instabilities*, Vladimir Gnezdilov, Yurii G. Pashkevich, Peter Lemmens, Dirk Wulferding, Tatiana Shevtsova, Alexander Gusev, Dmitry Chareev, and Alexander Vasiliev, Phys. Rev. B **87**, 144508 (2013).

- *Charge gap and charge-phonon coupling in $LuFe_2O_4$*, A. Glamazda, K.-Y. Choi, P. Lemmens, D. Wulferding, S. Park, and S.-W. Cheong, Phys. Rev. B **87**, 144416 (2013).

- *Competing lattice fluctuations and magnetic excitations in CuO*, K.-Y. Choi, W.-J. Lee, A. Glamazda, P. Lemmens, D. Wulferding, Y. Sekio, and T. Kimura, Phys. Rev. B **87**, 184407 (2013).

- *Raman scattering of electronic surface and bulk states in the giant Rashba, polar semiconductor BiTeI*, V. Gnezdilov, D. Wulferding, P. Lemmens, A. Möller, P. Recher, H. Berger, R. Sankar, and F. C. Chou, arXiv:1303.4333v1 (2013).

- *Phonon and orbital anomalies during the dimerization process in $TiPO_4$*, Dirk Wulferding, Peter Lemmens, Kwang-Yong Choi, Yurii G. Pashkevich, Roman Yu. Babkin, Karina V. Lamonova, Angela Möller, Joseph M. Law, Reinhard K. Kremer, and Robert Glaum, arXiv:cond-mat (2013).

Appendix C

Contributions to conferences and workshops

- *Highly Frustrated Magnetism 2008*, TU Braunschweig 2008, Posters "Anomalous electronic properties, scattering rates and the phase diagram of the cobaltates Na_xCoO_2", "Anomalous Excitations in $s = 1/2$ Kagome $ZnCu_3(OH)_6Cl_2$ and $Rb_2Cu_3SnF_{12}$"

- *Topological Order and Quantum Hall Systems*, MPI Dresden 2009, Poster "Instabilities in the frustrated 2-D $J_1 - J_2$ square lattice $(CuCl_{1-x}Br_x)La(Nb_{1-y}Ta_y)_2O_7$"

- *Orbital 2009*, Helmholtz Zentrum Berlin 2009, Poster "Interplay of thermal and quantum fluctuations in the Kagome compound $ZnCu_3(OH)_6Cl_2$"

- *Kagome systems*, Univ. Paris-Sud Orsay 2010, Poster "Excitations on the Kagome lattice: A comparative Raman study"

- *DPG Spring Meeting 2010*, Regensburg 2010, Talk "Interplay of thermal and quantum spin fluctuations on the Kagome lattice"

- *Perspectives in Highly Frustrated Materials*, MPI Dresden 2010, Talk "Thermal and quantum fluctuations in the Kagome lattice"

- *International Conference for Young Scientists*, ILTPE Kharkov 2010, Talk "Thermal and quantum fluctuations in the Kagome lattice"

- *Structure - Properties Relationships in Magnetic Materials*, MPI Stuttgart 2010, Poster "Excitations on the Kagome lattice: A comparative Raman study"

- *NTH Summer School for Students*, Hannover 2010, Lecture "Introduction to Raman scattering in correlated electron systems"

- *PSI Summer School on Condensed Matter Research, Magnetic Materials*, Zuoz 2010, Poster "Excitations on the Kagome lattice: A comparative Raman study"

- *IGSM Summer School 2010*, Warberg 2010, Poster "Excitations on the Kagome lattice: A comparative Raman study"

- *NTH Winter School*, Bad Hofgastein 2011, Talk "Morphology and Functionalization of nanoscale templates"

- *DFG SPP 1458 Project Kick-Off Meeting*, IFW Dresden 2011, Poster "Electronic and structural degrees of freedom in pnictides: A Raman scattering study"

- *DPG Spring Meeting 2011*, Dresden 2011, Poster "Effect of spin state, ordered moment and lattice anharmonicity of phonons in FeTe", Talks "Spinon continuum and the ground state of the quantum kagome system", "Magnetic and phononic excitation spectrum of the spin dimer system $Sr_3Cr_2O_8$"

- *International Conference for Young Scientists*, ILTPE Kharkov 2011, Talk "Strong orbital fluctuations in the quantum spin dimer system $Sr_3Cr_2O_8$"

- *NTH Autumn Workshop*, Hannover 2011, Talk "Excitations in spin liquid states"

- *PSI User Meeting*, PSI Villigen 2012, Talk "Approaching the HTSC problem with μSR and Raman"

- *DPG Spring Meeting 2012*, Berlin 2012, Talks "Tuning the spin dynamics of kagome systems", "Spin and lattice dynamics in the low-dimensional quantum magnet $(NO)Cu(NO_3)_3$"

- *NTH Spring Workshop*, Goslar 2012, Talk "Raman scattering on topological insulators: A comparative study"

- *Itinerant Spin-Orbital Systems: From Magnetic Frustration to Novel Superconductivity*, MPI Dresden 2012, Poster "Crossover from a resonating valence bond state to dynamical lattice instabilities in the confederate flag system $(NO)[Cu(NO_3)_3]$"

- *ICM 2012*, Busan 2012, Poster "Light scattering in spin liquid systems"

- *DPG Spring Meeting 2013*, Regensburg 2013, Talks "Low vs. high energy excitations in the Skyrmion lattice Cu_2OSeO_3", "Is there a magnetic analogon of the isotope effect in HTSC?"

- *Helmholtz Virtual Institute Kick-off Meeting: New states of matter and their excitations*, Berlin 2013, Poster "Light scattering in antiferromagnets with competing interactions – from triangular to kagome lattices"

- *NTH Spring Workshop*, Goslar 2013, Poster "Fluctuation regimes in frustrated correlated electron systems"

- *ZFM Festkörpernachmittag*, Hannover 2013, Talk "Lichtstreuung als Tool zur Charakterisierung von Festkörpern und ihren Energieskalen am Beispiel magnetischer und struktureller Phasenübergänge"

Bibliography

[1] A. Smekal, *Zur Quantentheorie der Dispersion*, Die Naturwissenschaften **11**, 43 (1923).

[2] C. V. Raman, Ind. J. Phys. **2**, 387 (1928).

[3] E. Ya. Sherman, O. V. Misochko, and P. Lemmens, *What can one learn from Raman Spectra of High-Temperature Superconductors?* in "Spectroscopy of High Temperature Superconductors, A Theoretical View", Taylor & Francis Inc, London and New York (2003).

[4] K.-Y. Choi, P. Lemmens, *Scattering: Inelastic Scattering Technique – Raman* in Encyclopedia of Condensed Matter Physics, G. Bassani, G. Liedl, and P. Wyder (eds.), Elsevier, Amsterdam (2005).

[5] P. Lemmens, G. Güntherodt, and C. Gros, Phys. Rep. **375**, 1 (2003).

[6] J. W. Halley, Phys. Rev. Lett. **41**, 1605 (1978).

[7] B. N. Narozhny, Phys. Rev. B **54**, 3311 (1996).

[8] M. J. Buerger, *Crystal-Structure Analysis*, New York: John Wiley, 163 – 171, 226 – 231 (1960).

[9] N. D. Mermin, H. Wagner, Phys. Rev. Lett. **17**, 1133 (1966).

[10] P. W. Anderson, Mater. Res. Bull. **8**(2) (1973).

[11] L. Pauling, *The Nature of the Chemical Bond*, 3^{rd} ed. Cornell Univ. Press, Ithaca, New York (1960).

[12] P. W. Anderson, Science **235**, 1196 (1987).

[13] H. Bethe, Z. Phys. **71**, 205 (1931).

[14] J. des Cloizeaux, J. J. Pearson, Phys. Rev. **128**, 2131 (1962).

[15] L. D. Faddeev, L. A. Takhtajan, Phys. Lett. A **85**, 375 (1981).

[16] A. B. Harris, C. Kallin, and A. J. Berlinsky, Phys. Rev. B **45**, 2899 (1992).

[17] J. Villain, R. Bidaux, J.-P. Carton, and R. Conte, J. Phys. (Paris) **41**, 1263 (1980).

[18] W. Schweika, M. Valldor, and P. Lemmens, Phys. Rev. Lett. **98**, 067201 (2007).

[19] R. R. P. Singh, D. A. Huse, Phys. Rev. B **76**, 180407(R) (2007).

[20] S. Yan, D. A. Huse, S. R. White, Science **332**, 1173 (2011).

[21] Y. Ran, M. Hermele, P. A. Lee, and X.-G. Wen, Phys. Rev. Lett. **98**, 117205 (2007).

[22] W. Rantner and X.-G. Wen, Phys. Rev. Lett. **86**, 3871 (2001).

[23] O. Cépas, C. M. Fong, P. W. Leung, and C. Lhuillier, Phys. Rev. B **78**, 140405(R) (2008).

[24] W. Zheng, J. O. Fjærestad, R. R. P. Singh, R. H. McKenzie, and R. Coldea, Phys. Rev. B **74**, 224420 (2006).

[25] R. L. Doretto, M. Vojta, Phys. Rev. B **85**, 104416 (2012).

[26] D. Wulferding, P. Lemmens, K.-Y. Choi, Yu. G. Pashkevich, R. Yu. Babkin, K. V. Lamonova, A. Möller, J. M. Law, R. K. Kremer, and R. Glaum, arXiv:cond-mat (2013).

[27] Bilbao Crystallographic Server [http://www.cryst.ehu.es].

[28] J. M. Law, *Identification and investigation of new low-dimensional quantum spin systems*, Ph.D. thesis, MPI-FKF Stuttgart, 2011.

[29] J. M. Law, C. Hoch, R. Glaum, I. Heinmaa, R. Stern, J. Kang, C. Lee, M.-H. Whangbo, and R. K. Kremer, Phys. Rev. B **83**, 180414(R) (2011).

[30] J. W. Bray, H. R. Hart, L. V. Interrante, I. S. Jacobs, J. S. Kasper, G. D. Watkins, S. H. Wee, and J. C. Bonner, Phys. Rev. Lett. **35**, 744 (1975).

[31] M. Hase, I. Terasaki, and K. Uchinokura, Phys. Rev. Lett. **70**, 3651 (1993).

[32] R. Rückamp, J. Baier, M. Kriener, M. W. Haverkort, T. Lorenz, G. S. Uhrig, L. Jongen, A. Möller, G. Meyer, and M. Grüninger, Phys. Rev. Lett. **95**, 097203 (2005).

[33] see, e.g., Ch. Kant, J. Deisenhofer, T. Rudolf, F. Mayr, F. Schrettle, A. Loidl, V. Gnezdilov, D. Wulferding, P. Lemmens, and V. Tsurkan, Phys. Rev. B **80**, 214417 (2009).

[34] R. Werner, C. Gros, and M. Braden, Phys. Rev. B **59**, 14356 (1999).

[35] E. J. Baran, F. Muto, N. Kumada, and N. Kinomura, J. Mater. Sci. Lett. **8**, 1305 (1989).

[36] P. Lemmens, K. Y. Choi, G. Caimi, L. Degiorgi, N. N. Kovaleva, A. Seidel, and F. C. Chou, Phys. Rev. B **70**, 134429 (2004).

[37] L. P. Regnault, M. Aïn, B. Hennion, G. Dhalenne, and A. Revcolevschi, Phys. Rev. B **53**, 5579 (1996).

[38] P. Lemmens, K.-Y. Choi, R. Valenti, T. Saha-Dasgupta, E. Abel, Y. S. Lee, and F. C. Chou, New Journal of Physics **7**, 74 (2005).

[39] P. H. M. van Loosdrecht, J. P. Boucher, G. Martinez, G. Dhalenne, and A. Revcolevschi, Phys. Rev. Lett. **76**, 311 (1996).

[40] Yu. G. Pashkevich, unpublished (2012).

[41] D. Wulferding, P. Lemmens, K.-Y. Choi, V. Gnezdilov, Yu. G. Pashkevich, J. Deisenhofer, D. Quintero-Castro, A. T. M. N. Islam, and B. Lake, Phys. Rev. B **84**, 064419 (2011).

[42] L. C. Chapon, S. Stock, P. G. Radaelli, and C. Martin, arXiv:0807.0877v2 (2008).

[43] P. Radaelli, Y. Horibe, M. J. Gutmann, H. Ishibashi, C. H. Chen, R. M. Ibberson, Y. Koyama, Y.-S. Hor, V. Kiryukhin, and S.-W. Cheong, Nature (London) **416**, 155 (2002).

[44] D. L. Quintero-Castro, B. Lake, E. M. Wheeler, A. T. M. N. Islam, T. Guidi, K. C. Rule, Z. Izaola, M. Russina, K. Kiefer, and Y. Skourki, Phys. Rev. B **81**, 014415 (2010).

[45] Zhe Wang, M. Schmidt, A. Günther, S. Schaile, N. Pascher, F. Mayr, Y. Goncharov, D. L. Quintero-Castro, A. T. M. N. Islam, B. Lake, H.-A. Krug von Nidda, A. Loidl, and J. Deisenhofer, Phys. Rev. B **83**, 201102(R) (2011).

[46] A. A. Aczel, Y. Kohama, C. Marcenat, F. Weickert, M. Jaime, O. E. Ayala-Valenzuela, R. D. McDonald, S. D. Selesnic, H. A. Dabkowska, and G. M. Luke, Phys. Rev. Lett. **103**, 207203 (2009).

[47] P. Fazekas, *Lecture Notes on Electron Correlation and Magnetism*, World Scientific Publishing Co. Pte. Ltd. Singapore (1999).

[48] J. A. Sanjurjo, C. Rettori, S. Oseroff, and Z. Fisk, Phys. Rev. B **49**, 4391 (1994).

[49] G. Radtke, A. Saúl, H. A. Dabkowska, G. M. Luke, and G. A. Botton, Phys. Rev. Lett. **105**, 036401 (2010).

[50] see, e.g., J. F. Scott, Rev. Mod. Phys. **46**, 83 (1974).

[51] G. Els, P. H. M. van Loosdrecht, P. Lemmens, H. Vonberg, G. Güntherodt, G. S. Uhrig, O. Fujita, J. Akimitsu, G. Dhalenne, and A. Revcolevschi, Phys. Rev. Lett. **79**, 5138 (1997).

[52] K.-Y. Choi, D. Wulferding, H. Berger, and P. Lemmens, Phys. Rev. B **80**, 245108 (2009).

[53] Y. Tokura and N. Nagaosa, Science **288**, 462 (2000).

[54] S. Miyasaka, J. Fujioka, M. Iwama, Y. Okimoto, and Y. Tokura, Phys. Rev. B **73**, 224436 (2006).

[55] C. Ulrich, A. Gössling, M. Grüninger, M. Guennou, H. Roth, M. Cwik, T. Lorenz, G. Khaliullin, and B. Keimer, Phys. Rev. Lett. **97**, 157401 (2006).

[56] K.-Y. Choi, G. Güntherodt, A. Oosawa, H. Tanaka, and P. Lemmens, Phys. Rev. B **68**, 174412 (2003).

[57] M. Kofu, J.-H. Kim, S. Ji, S.-H. Lee, H. Ueda, Y. Qiu, H.-J. Kang, M. A. Green, and Y. Ueda, Phys. Rev. Lett. **102**, 037206 (2009); M. Kofu, H. Ueda, H. Nojiri, Y. Oshima, T. Zenmoto, K. C. Rule, S. Gerischer, B. Lake, C. D. Batista, Y. Ueda, and S.-H. Lee, Phys. Rev. Lett. **102**, 177204 (2009).

[58] Z. Wang, M. Schmidt, A. Günther, F. Mayr, Y. Wan, S.-H. Lee, H. Ueda, Y. Ueda, A. Loidl, and J. Deisenhofer, Phys. Rev. B **85**, 224304 (2012).

[59] D. Wulferding, P. Lemmens, P. Scheib, J. Röder, P. Mendels, S. Chu, T. Han, and Y. S. Lee, Phys. Rev. B **82**, 144412 (2010).

[60] D. Wulferding, P. Lemmens, H. Yoshida, Y. Okamoto, and Z. Hiroi, J. Phys.: Condens. Matter **24**, 185602 (2012).

[61] T. H. Han, J. S. Helton, S. Chu, A. Prodi, D. K. Singh, C. Mazzoli, P. Müller, D. G. Nocera, and Y. S. Lee, Phys. Rev. B **83**, 100402(R) (2011).

[62] J. S. Helton, K. Matan, M. P. Shores, E. A. Nytko, B. M Bartlett, Y. Yoshida, Y. Takano, A. Suslov, Y. Qiu, J.-H. Chung, D. G. Nocera, and Y. S. Lee, Phys. Rev. Lett. **98**, 107204 (2007).

[63] M. A. de Vries, K. V. Kamenev, W. A. Kockelmann, J. Sanchez-Benitez, and A. Harrison, Phys. Rev. Lett. **100**, 157205 (2008).

[64] P. Mendels, F. Bert, M. A. de Vries, A. Olariu, A. Harrison, F. Duc, J.-C. Trombe, J. S. Lord, A. Amato, and C. Baines, Phys. Rev. Lett. **98**, 077204 (2007).

[65] A. Zorko, S. Nellutla, J. van Tol, L. C. Brunel, F. Bert, F. Duc, J.-C. Trombe, M. A. de Vries, A. Harrison, and P. Mendels, Phys. Rev. Lett. **101**, 026405 (2008).

[66] Ph. Mendels and F. Bert, J. Phys. Soc. Jpn. **79**, 011001 (2010).

[67] M. A. de Vries, D. Wulferding, P. Lemmens, J. S. Lord, A. Harrison, P. Bonville, F. Bert, and P. Mendels, Phys. Rev. B **85**, 014422 (2012).

[68] H. Kuroe, J. Sasaki, T. Sekine, Y. Sasago, M. Hase, N. Koide, K. Uchinokura, H. Kojima, I. Tanaka, and Y. Shibuya, Physica B **219-220**, 104 (1996).

[69] P. Lemmens, M. Grove, M. Fischer, G. Güntherodt, V. N. Kotov, H. Kageyama, K. Onizuka, and Y. Ueda, Phys. Rev. Lett. **85**, 2605 (2000).

[70] M. Hermele, Y. Ran, P. A. Lee, and X.-G. Wen, Phys. Rev. B **77**, 224413 (2008).

[71] W.-H. Ko, Z.-X. Liu, T.-K. Ng, and P. A. Lee, Phys. Rev. B **81**, 024414 (2010).

[72] O. Cépas, J. O. Haerter, and C. Lhuillier, Phys. Rev. B **77**, 172406 (2008).

[73] A. Läuchli and C. Lhuillier, arXiv:0901.1065 (unpublished).

[74] A. Olariu, P. Mendels, F. Bert, F. Duc, J. C. Trombe, M. A. de Vries, and A. Harrison, Phys. Rev. Lett. **100**, 087202 (2008).

[75] M. A. Lafontaine, A. le Bail, and G. Férey, J. Solid State Chem. **85**, 220 (1990).

[76] P. Sindzingre, arXiv:0707.4264v1 (unpublished).

[77] H. Yoshida, Y. Okamoto, T. Tayama, T. Sakakibara, M. Tokunaga, A. Matsuo, Y. Narumi, K. Kindo, M. Yoshida, M. Takigawa, and Z. Hiroi, J. Phys. Soc. Jpn. **78**, 043704 (2009).

[78] G. J. Nilsen, F. C. Coomer, M. A. de Vries, J. R. Stewart, P. P. Deen, A. Harrison, and H. M. Rønnow, Phys. Rev. B **84**, 172401 (2011).

[79] M. Yoshida, M. Takigawa, H. Yoshida, Y. Okamoto, and Z. Hiroi, Phys. Rev. Lett. **103**, 077207 (2009).

[80] R. H. Colman, F. Bert, D. Boldrin, A. D. Hillier, P. Manuel, P. Mendels, and A. S. Wills, Phys. Rev. B **83**, 180416(R) (2011).

[81] Y. Okamoto, H. Yoshida, and Z. Hiroi, J. Phys. Soc. Jpn. **78**, 033701 (2009).

[82] J. A. Quilliam, F. Bert, R. H. Colman, D. Boldrin, A. S. Wills, and P. Mendels, Phys. Rev. B **84**, 180401(R) (2011).

[83] H. Yoshida, J.-I. Yamaura, M. Isobe, Y. Okamoto, G. J. Nilsen, and Z. Hiroi, Nature Communications **3**, 860 (2012).

[84] M. G. Cottam, D. J. Lockwood, "Light Scattering in Magnetic Solids", Wiley, New York (1986).

[85] P. A. Fleury, Phys. Rev. **180**, 591 (1969).

[86] D. Wulferding, K.-Y. Choi, P. Lemmens, A. N. Ponomaryov, J. van Tol, A. T. M. N. Islam, S. Toth, and B. Lake, J. Phys.: Condens. Matter **24**, 435604 (2012).

[87] E. Wheeler, R. Coldea, E. Wawrzyńska, T. Sörgel, M. Jansen, M. M. Koza, J. Taylor, P. Adroguer, and N. Shannon, Phys. Rev. B **79**, 104421 (2009).

[88] H. Pausch, H. Müller-Buschbaum, Z. anorg. allg. Chem. **405**, 113 (1974).

[89] S. Toth, B. Lake, S. A. J. Kimber, O. Pieper, M. Reehuis, A. T. M. N. Islam, O. Zaharko, C. Ritter, A. H. Hill, H. Ryll, K. Kiefer, D. N. Argyriou, and A. J . Williams, Phys. Rev. B **84**, 054452 (2011).

[90] S. Toth, B. Lake, K. Hradil, T. Guidi, K. C. Rule, M. B. Stone, and A. T. M. N. Islam, Phys. Rev. Lett. **109**, 127203 (2012).

[91] L. C. Chapon, P. Manuel, F. Damay, P. Toledano, V. Hardy, and C. Martin, Phys. Rev. B **83**, 024409 (2011).

[92] M. Hemmida, H.-A. Krug von Nidda, N. Büttgen, A. Loidl, L. K. Alexander, R. Nath, A. V. Mahajan, R. F. Berger, R. J. Cava, Y. Singh, and D. C. Johnston, Phys. Rev. B **80**, 054406 (2009).

[93] M. Hemmida, H.-A. Krug von Nidda, and A. Loidl, Journal of Physics: Conference Series **200**, 022016 (2010).

[94] M. Hemmida, H.-A. Krug von Nidda, and A. Loidl, J. Phys. Soc. Jpn. **80**, 053707 (2011).

[95] N. Perkins and W. Brenig, Phys. Rev. B **77**, 174412 (2008).

[96] A. L. Chernyshev, M. E. Zhitomirsky, Phys. Rev. Lett. **97**, 207202 (2006).

[97] K.-Y. Choi, P. Lemmens, D. Heydhausen, G. Güntherodt, C. Baumann, R. Klingeler, P. Reutler, and B. Büchner, Phys. Rev. B **77**, 064415 (2008).

[98] Picture taken from [http://www.mindat.org/photo-80390.html].